# Advances in Measurement and Force Modeling for Improved GNSS-based Precise Orbit Determination of CYGNSS and Sentinel-6 MF

by

**Alex V. Conrad**

B.S., Arizona State University, 2017

M.S., University of Colorado Boulder, 2020

A thesis submitted to the

Faculty of the Graduate School of the

University of Colorado in partial fulfillment

of the requirements for the degree of

Doctor of Philosophy

Department of Aerospace Engineering Sciences

2023

Committee Members:

Penina Axelrad, Chair

Shailen Desai

Bruce Haines

Jade Morton

Steve Nerem

Conrad, Alex V. (Ph.D., Aerospace Engineering Sciences)

Advances in Measurement and Force Modeling for Improved GNSS-based Precise Orbit Determination of CYGNSS and Sentinel-6 MF

Thesis directed by Prof. Penina Axelrad

Precise orbit determination (POD) based on global navigation satellite systems (GNSS) tracking is fundamental to many space-based geodesy missions. The research presented here develops and implements improvements to the models and methods for two missions: CYGNSS, a low-cost constellation of small satellites, and Sentinel-6 Michael Freilich (MF), the current reference global ocean altimeter mission. The orbit solutions are improved though the advancement of the measurement models, dynamic force models, and solution strategies.

CYGNSS is a constellation of eight small satellites designed to use reflected GNSS signals for retrieval of ocean surface winds. The navigation requirements to achieve this primary mission are quite loose, allowing the project to use simple point positioning, with a single-frequency GPS receiver, to support mission orbit needs. Research presented here demonstrates that orbits with 3-D positioning accuracy better than 10 cm can be achieved, with an iterative solution strategy that includes calibration of the antenna, use of combined code and carrier GRAPHIC (GRoup And PHase Ionosphere Correction) observables, and correction of a timing difference between code and carrier measurements. The process is validated using comparable data from the GRACE (Gravity Recovery and Climate Experiment) mission, for which high precision reference orbits are available.

To support stringent POD requirements, Sentinel-6 MF is equipped with multiple tracking instruments: a TriG GPS receiver, a pair of redundant PODRIX GNSS (GPS + Galileo) receivers, a satellite laser retroreflector, and a Doppler Orbitography and Radiopositioning Integrated by Satellite (DORIS) receiver. The first study develops an improved dynamic solar radiation pressure model. Compared to the previously used macromodel, this results in more consistent estimates of drag and solar scale parameters throughout changes in the orientation of the sun relative to the

orbit plane (beta angle). The second study improves the measurement model by extending the new GPS IIIA transmitter antenna calibration out to boresight angles of 14-17 degrees, which are not observed by ground-based receivers, but are quite important for receivers in low Earth orbit. Implementation of this extension produces solutions that incorporate GPS IIIA measurements with statistics consistent with older satellite families. Finally, applying lessons learned from the previous studies, orbit solutions are generated from all available Sentinel-6 MF GNSS tracking data. This multi-receiver/GNSS configuration with two independent receivers and constellations (GPS + Galileo) revealed a range bias effect in the TriG GNSS observations that can be calibrated. Processing the calibrated TriG and PODRIX observations separately results in highly accurate orbit solutions, which are both consistent with one-way satellite laser ranging (SLR) residuals at the level of 6.9 mm rms. When processed together, the TriG plus PODRIX multi-GNSS solutions produced the most accurate orbit solutions with one-way SLR residual rms of 6.8 mm.

## Dedication

To my family and those who have supported me, I could not have done this without you.

## Acknowledgements

I would like to thank Dr. Shailen Desai, Dr. Bruce Haines, and Dr. Cinzia Zuffada for their support, guidance, advice, and training in all the work and analysis described here. I would also like to thank my advisor Dr. Penny Axelrad for her tireless help and support in getting me to this point.

The CYGNSS research presented here was supported by the NASA ROSES PO award NRA NNH16ZDA001N, 2017-2020. Part of the research was carried out at the Jet Propulsion Laboratory, Caltech, under a contract with the National Aeronautics and Space Administration (80NM0018D0004). The Sentinel-6 MF work in this thesis was supported by the Jet Propulsion Laboratory, California Institute of Technology on Subcontract 1659402 to the University of Colorado.

# Contents

**Chapter**

# Tables

**Table**

# Figures

**Figure**

# Chapter 1

# Introduction

## 1.1 Introduction

GNSS-based precise orbit determination (POD) is a critical component for space-based satellite geodesy missions such as those supporting satellite altimetry (Haines et al., 2004; Bertiger et al., 2010a; Montenbruck et al., 2021) and gravity recovery (Kang et al., 2020). Orbit accuracies of 3-5 cm (3-D) (Hackel et al., 2017) can be readily achieved for low Earth orbiting (LEO) satellite missions equipped with dual-frequency GNSS receivers. This level of accuracy is achieved by processing dual-frequency pseudorange and carrier phase observations in combination with a state-of-the-art gravity field (Lemoine et al., 2019), satellite surface macromodel (Marshall and Luthcke, 1994), antenna calibration (Haines et al., 2004), and reduced-dynamic processing (Wu et al., 1991). The implementation of single-receiver integer ambiguity resolution has also been shown to improve orbit estimates (Bertiger et al., 2010b; Montenbruck et al., 2018) with recent results by Mao et al. (2021) demonstrating 1 cm precision for Sentinel-3A/B.

This thesis focuses on several aspects of the POD approach for two very different types of missions: CYGNSS and Sentinel-6 Michael Freilich (MF). CYGNSS is a constellation of eight low-cost, small satellites with a primary mission to measure ocean surface wind speed based on reflected GNSS (Global Navigation Satellite Systems) signals (GNSS-R) (Ruf et al., 2012). There is also interest in using these reflections to observe open water and ice surface heights (Mashburn et al., 2020; Li et al., 2018, 2019), which requires precise orbit knowledge. The goal of improving

and understanding CYGNSS orbit orbit accuracy is achieved by assessing various POD solution strategies given the limitation of the onboard receiver to L1 single-frequency GPS tracking data.

In contrast, Sentinel-6 MF is a multi-national satellite mission that serves as the current reference altimeter mission for global ocean sea-surface height (Donlon et al., 2021b). The accuracy of satellite-based altimetry is highly dependent on orbit knowledge, with radial orbit errors mapping directly into the sea surface height estimates. To support a radial orbit accuracy requirement of $< 1.5$ cm (rms) (Donlon et al., 2021b), Sentinel-6 MF is equipped with four independent tracking systems: a Doppler Orbitography and Radiopositioning Integrated by Satellite (DORIS) receiver (Auriol and Tourain, 2010), a laser retroreflector array for ground-based satellite laser ranging (SLR), a redundant pair of multi-GNSS PODRIX receivers developed by RUAG that is the primary GNSS POD instrument (Montenbruck et al., 2021; Peter et al., 2022), and a TriG receiver from NASA's Jet Propulsion Laboratory (JPL) that supports POD and radio occultation measurements (Tien et al., 2010, 2012). The POD methods presented in the next three chapters exclusively use the GNSS tracking data. The SLR measurements are withheld from the solution and thus form the basis for an independent evaluation of the GNSS-based POD accuracy. DORIS observations are not included as part of these studies.

The research presented in this thesis focuses on improvements to the measurement and force models and their impact on Sentinel-6 POD. It includes improvements in solar radiation pressure modeling and the estimation of an extension to the GPS IIIA antenna calibration which is consistent with the current Block II International GNSS Service (IGS) calibrations. The lessons from these studies are then applied to a combined solution that uses all available GNSS observations from both the TriG and PODRIX. The overall goal is to improve GNSS-based POD performance and thus the quality of GNSS-based science. All POD solutions are estimated within JPL's GipsyX software (Bertiger et al., 2020). GipsyX is currently used for nearly all operational POD and research activities using GNSS tracking data at JPL. It derives its heritage from the legacy GIPSY/Oasis software dating to the 1980s (Wu and Thornton, 1985), and is thus well-established for applications of GNSS for positioning, timing, navigation, and geodetic science.

## 1.2 Research Contributions

### 1.2.1 CYGNSS Single-Frequency Orbit Determination

The primary mission objective for CYGNSS does not require precise orbit solutions. Thus, the only publicly available orbit product has been the navigation solutions computed by the onboard Surrey Satellite Technology Ltd. (SSTL) Space GPS Receiver Remote Sensing Instrument (SGR-ReSI). Given the interest in applications using GNSS-R for altimetry (Carreno-Luengo et al., 2017; Mashburn et al., 2020), this study was conducted with the goal of improving the CYGNSS orbit knowledge and understanding the limiting factors.

The contributions presented here include an analysis and demonstration of single-frequency POD solutions for the CYGNSS spacecraft using two different strategies: a code-only solution and GRAPHIC (GRoup And PHase Ionosphere Correction) solution. As part of this effort, a method is also introduced for correcting an unexpected clock-like signal in the CYGNSS raw carrier measurements that is not present in the pseudorange. Typically, GPS measurements contain a similar clock signal in both the pseudorange and carrier, but we found that this is not the case for CYGNSS. By estimating and removing this clock-like signal from the phase observations we are able to produce single-frequency GRAPHIC orbit solutions. The GRAPHIC observable removes the first order ionosphere delay by taking the average of code and phase measurements. Another important feature for CYGNSS POD is an antenna calibration which captures line-of-sight dependent delays due to both the physical antenna pattern (Aparicio et al., 1996) and spacecraft multipath effects (Young et al., 1985). Antenna calibrations can be applied to any GNSS observable. For CYGNSS, an antenna calibration was separately estimated for both the code-only and GRAPHIC observables. The calibration is estimated within a dynamic POD solution which simultaneously estimates the clock biases, phase biases, and calibrations together. The antenna calibration is then applied to code-only and GRAPHIC single-frequency reduced-dynamic orbit solutions.

These methods were validated by applying them to data from the GRACE (Gravity Recovery and Climate Experiment) mission, where highly accurate dual-frequency solutions are avail-

able. The GRACE results can be extrapolated to assess the likely errors associated with CYGNSS single-frequency GRAPHIC POD where solutions based on the GRAPHIC observable are much more accurate than code-only solutions. The GRAPHIC POD strategy with antenna calibration and clock correction produces CYGNSS orbit solutions with estimated $1\sigma$ accuracy of about 3 cm radial, 3 cm cross-track, and 6 cm in-track. This study is published in the *Journal of the Institute of Navigation* (Conrad et al., 2023b). Thus, this research has demonstrated the ability to provide improved CYGNSS orbit solutions suitable for GNSS-R-based altimetry, where uncertainty in the orbit has been a significant error source (Mashburn et al., 2020; Li et al., 2018, 2019). Additionally, the strategies described are expected to enable a similar level of accuracy for other low-cost science missions using small satellites equipped with single-frequency receivers intended for onboard navigation and timing.

### 1.2.2 Sentinel-6 MF Radiation Pressure Modeling

The next set of contributions are based on an examination of key background models for Sentinel-6 MF POD. The first is an improvement to the modeling of forces due to solar radiation pressure (SRP). SRP forces are typically captured using a model of spacecraft surfaces, commonly called a box-wing model or macromodel (Marshall and Luthcke, 1994; Rodriguez-Solano et al., 2012; Montenbruck et al., 2015b). Such macromodels consist of a simplified set of plates that represent the spacecraft geometry. Surfaces are defined by a normal vector, total surface area, and reflective properties. SRP forces from the macromodel are computed as the sum of the individual effects from each plate.

One limitation of the macromodel is that shadowing is only considered for each plate individually, and does not account for the relative positioning of the plates. Due to the inability to account for overall shadowing, the original Sentinel-6 MF macromodel (ESA, 2023) resulted in several estimated parameters showing strong dependence on sun elevation with respect to orbit plane (beta angle). The most problematic are the estimated antenna offsets. Due to spacecraft multipath (Young et al., 1985) and the antenna gain pattern (Aparicio et al., 1996), mean antenna

offsets exist within the phase variations (PV) in the in-flight environment relative to mechanical spacecraft antenna reference point. The effective mean phase center offset (PCO) due to the PVs can be easily absorbed into the antenna calibration. However, when estimating these offsets, they are expected to be relatively consistent over time. The Sentinel-6 MF estimated antenna y-offsets (roughly aligned with the cross-track direction) showed strong correlation with the beta angle. This behavior is indicative of poor SRP modeling and can degrade the estimated antenna calibration. Thus, this research estimates new solar radiation force models and demonstrates greater consistency across the beta angle cycle for drag and solar scale estimates, antenna offset estimates, measurement residuals, and orbit precision when compared to the original macromodel. POD solutions with the new SRP models also show improvement in the residual rms of one-way independent SLR measurements from 8.6 mm to 8.1 mm when processed with a reduced-dynamic technique (Wu et al., 1991). This research is the topic of Chapter 6 and was published in the Proceedings of ION GNSS+ 2022 (Conrad et al., 2022).

### 1.2.3 Extension of the GPS IIIA IGS Antenna Calibration

Accurate phase modeling is crucial to single receiver phase ambiguity resolution and requires calibrations for both the transmitting and receiving antennas (Schmid et al., 2016). The primary contribution of this study is an estimated extension of the IGS14 GPS IIIA phase variations for boresight angles higher than 14 degrees (the observation limit for ground stations). Thus, the extension improves LEO POD solutions, which can observe transmitter boresight angles up to 17 degrees, without impacting terrestrial GNSS processing. Using the Sentinel-6 MF TriG GNSS observations, the extension is estimated in a manner that is consistent with the IGS14 Block II antenna calibrations. This approach facilitates the continuity of POD solutions based on IGS standards during and after the transition of the GPS constellation from only Block II to also include GPS IIIA transmitters. This research demonstrates that without the IGS14 GPS IIIA extension, the LEO orbit solution performance is degraded which is most apparent in the post-fit residuals rms and the success of ambiguity resolution. When the estimated GPS IIIA extension

is applied, the POD solutions are consistent with orbit solutions computed from only the Block II measurements and calibrations. The estimated GPS IIIA antenna calibration extension research has been published in the *Journal of Geodesy* (Conrad et al., 2023a). This publication provides a reference that users can apply directly for their use-case or to compare against independent extensions. Furthermore, the estimated extension is also applicable to the more recent ISG20 antenna calibrations.

### 1.2.4 Sentinel-6 MF Combined TriG and PODRIX Orbit Solution

The previously described contributions for Sentinel-6 MF SRP modeling improvements and GPS IIIA extension are steps required to facilitate the final contribution in this thesis, which is an analysis of a combined POD solution with tracking data from both the TriG and PODRIX receivers. The PODRIX receiver poses additional challenges and potential benefits for POD as it tracks both GPS and Galileo signals (Montenbruck et al., 2021). Unlike the TriG which uses the legacy C1W/C2W observations, the PODRIX GPS observations are a mix of legacy GPS C1W/C2W signals and modern L2C signals. To properly incorporate these various signals, the pseudorange observations must be corrected for transmitter and receiver based differential code biases.

The availability of both sets of receiver observations revealed an unexpected range bias effect of approximately 405 m in the TriG pseudorange observations that resulted in an in-track bias in the TriG orbits of about 10 mm relative to PODRIX derived orbit solutions. After this bias was correctly calibrated, an evaluation of TriG and PODRIX based solutions was performed. The TriG and PODRIX had similar performance in terms of orbit overlap precision and accuracy. However, the PODRIX Galileo observations showed lower code and phase tracking residual rms values compared to the GPS observations. This is likely due to the superior noise and multipath rejection for wideband tracking on E5 compared to P(Y) cross correlation tracking on the TriG. Processing the calibrated TriG and PODRIX observations separately results in highly accurate orbit solutions with radial orbit accuracies better than 1 cm rms as indicated by one-way SLR residuals.

Orbit solution accuracy is slightly improved by processing both TriG and PODRIX observations together, resulting in one-way SLR residual rms of 6.8 mm.

## 1.3 Overview of Dissertation

The remainder of this dissertation begins with an overview and background of GNSS based precise orbit determination techniques by presenting the equations of motion, measurement models, and the setup of the solution. Additionally, strategies for evaluating the POD solution in terms of precision and accuracy are presented. Next, Chapter 3 discusses the formulation and properties of antenna calibration, which is an important factor in each of the following studies, as it accounts for a significant source of error in the observations. Chapter 4 describes the CYGNSS single-frequency orbit estimation strategy and its validation using the GRACE-B satellite.

The next four chapters cover the Sentinel-6 MF studies, starting in Chapter 5 with a brief overview of the Sentinel-6 MF mission. This chapter also presents the common background models, POD solution strategy, attitude description, and SLR corrections used throughout the following chapters. Chapter 6 describes the methods for improving the solar radiation pressure modeling for Sentinel-6 MF. This is followed by the estimation of an extension to the GPS IIIA IGS14 antenna phase variations for use by LEO satellites in Chapter 7. The development of Chapters 6 and 7 were done together. The estimated macromodel was produced first and applied in the estimation of the GPS IIIA extension. Next, the GPS IIIA extension was included for the SRP table estimation. Chapter 8 presents a combined POD solution using the TriG and PODRIX observations and comparisons between the different POD solutions. Finally, Chapter 9 provides a summary of this thesis and suggestions for future work.

# Chapter 2

# Global Navigation Satellite Systems Based Precise Orbit Determination

## 2.1 Background

The myriad of applications of GNSS have grown far beyond the original GPS requirements and likely anything the original designers could have conceived. The primary GNSS applications of positioning, navigation, and timing (PNT) have been extended beyond the surface of the Earth to include other spacecraft both below and above the constellations. The first publicly reported GPS measurements in LEO were made onboard the Landsat-4 satellite in 1982 using an experimental receiver (Birmingham et al., 1983). Only ten years later, in 1992, the TOPEX/Poseidon sea-surface altimetry mission was launched with stringent POD requirements. TOPEX/Poseidon carried a GPS demonstration receiver, a DORIS receiver, and retroreflector for ground-based satellite laser ranging (Haines et al., 1999). Because radial orbit errors map directly into the altimetry measurements, TOPEX/Poseidon was a driving force for much early GNSS-based POD research. Within a year of its launch, POD with better than 3 cm radial rms orbit accuracy using GPS tracking data alone (Bertiger et al., 1994) was demonstrated using a reduced-dynamic technique (Wu et al., 1991; Yunck et al., 1994, 1990). The follow-on mission, Jason-1, further improved the radial rms accuracy to 1 cm by incorporating improved geopotential models and in-flight calibration of the antenna phase variations (Haines et al., 2004). Sub-centimeter accuracy for Jason-2 was achieved by also fixing phase ambiguities (Bertiger et al., 2010a).

This chapter provides the reader with an overview of the basic components of the GNSS based POD problem. The format here broadly follows the descriptions and notation by Bar-Sever (2021).

It includes a brief description of the dynamical and measurement models, the solution strategies through the use of linearization, and dynamic, kinematic, and reduced-dynamic approaches for orbit determination. Finally, a brief overview of the techniques applied for assessment of the orbit solution is provided.

## 2.2 GNSS Based POD

Missions where accuracy is of the utmost importance, such as Sentinel-6 MF, will use geodetic quality dual-frequency receivers and apply the highest fidelity models possible. Solutions to the orbit determination problem with GNSS measurements covers a large trade space between the desired accuracy and the complexity of the problem. Not all missions will require centimeter level accuracy and as such can simplify the models used in analysis and/or relax the hardware requirements to reduce cost.

GNSS-based LEO POD requires highly accurate knowledge of the GNSS transmitter orbit positions and clock biases. These can be estimated simultaneously with the LEO receiver or using GNSS clock and orbit products which are available from an established organization such as the International GNSS Service (IGS) (Johnston et al., 2017). The motion of the satellite in LEO can be modeled by the evolution of its position and velocity vectors in an inertial reference frame. For an initial position and velocity at time $t_0$

$$\boldsymbol{r}(t_0) = \boldsymbol{r_0} \tag{2.1}$$

$$\dot{\boldsymbol{r}}(t_0) = \boldsymbol{v_0} \tag{2.2}$$

the translational equations of motion are given by

$$\ddot{\boldsymbol{r}} = \boldsymbol{f}(\boldsymbol{r}, \dot{\boldsymbol{r}}, \boldsymbol{p}, t)/m \tag{2.3}$$

where $\boldsymbol{r} = \boldsymbol{r}(t)$ is the spacecraft position as a function of time and $\dot{\boldsymbol{r}}$ and $\ddot{\boldsymbol{r}}$ are the first and second time derivatives of $\boldsymbol{r}$; $\boldsymbol{f}$ represents the forces acting on the spacecraft; $m$ is the spacecraft mass; $\boldsymbol{p}$

contains the force model parameters; and $t$ is the coordinate time. The use of coordinate time is necessary to account for the differences in relativistic effects that occur on orbiting platforms. The force model vector $\boldsymbol{f}$ is the sum of all forces acting on the spacecraft such as the force due to the gravity field, solar radiation pressure, and atmospheric drag. The term $\boldsymbol{p}$ contains parameters of those models such as the drag coefficient and solar radiation pressure coefficient.

The GNSS pseudorange measurement, $X(t)$, is directly related to the difference between the position of the LEO spacecraft at the time of reception $t_r$ and the transmitter position at the time of transmission $t_t$ and is given by

$$X(t) = ||\boldsymbol{r_G}(t_t) - \boldsymbol{r}(t_r)|| + g(\boldsymbol{q}) + w \tag{2.4}$$

where the first term is the Euclidian norm of the difference between the transmitter position $\boldsymbol{r_G}$ and LEO position $\boldsymbol{r}$. The term $g$ contains the signal-in-space effects such as ionospheric delay as well as transmitting and receiver clock errors and antenna phase variations, and $w$ is the measurement noise. The vector $\boldsymbol{q}$ includes the measurement model parameters in $g$ to be estimated. This typically includes the receiver clock and phase measurement biases.

From the initial conditions $\boldsymbol{r_0}$ and $\boldsymbol{v_0}$, the satellite position in time, $\boldsymbol{r}(t)$, can be propagated by integrating Equation 2.3 forward in time. Incorporating Equation 2.3 into Equation 2.4 forms the basis of the orbit determination problem as follows

$$\boldsymbol{X}(t) = \boldsymbol{h}(\boldsymbol{r_0}, \boldsymbol{v_0}, \boldsymbol{p}, \boldsymbol{q}, t) + \boldsymbol{w} \tag{2.5}$$

where $\boldsymbol{X}(t)$ is now a vector of measurements and $\boldsymbol{h}$ contains the first two terms on the right hand side of Equation 2.4 written as function that relates the force and measurement models to the measurements at time $t$. Once the initial conditions $\boldsymbol{r_0}$, $\boldsymbol{v_0}$, and force model parameters $\boldsymbol{p}$ are known, Equation 2.3 can then be integrated forward from $t_0$ to any point in time, $t$, and the solution is produced.

### 2.2.1 POD Solution

Given the highly non-linear dynamics for a LEO spacecraft, the solution to Equation 2.5 cannot be inverted directly to solve for the initial state. Linearization techniques exist, such as batch least squares or Kalman filtering, that can be used with a suitable reference trajectory. This reference trajectory must be close enough to the *true* trajectory so that is stays within the linear regime. The initial reference trajectory can be formulated from a variety of sources. Typically, the initial reference states, $\boldsymbol{r}_{ref0}$, $\boldsymbol{v}_{ref0}$, and $\boldsymbol{p}_{ref}$, are solved for by minimizing the least-squares difference between the crude onboard navigation solution (top box in Figure 2.1) at each epoch $\boldsymbol{r}_{t_i}$ and integrated orbit $\boldsymbol{r}(t_i)$. This step is shown in the second box in Figure 2.1.

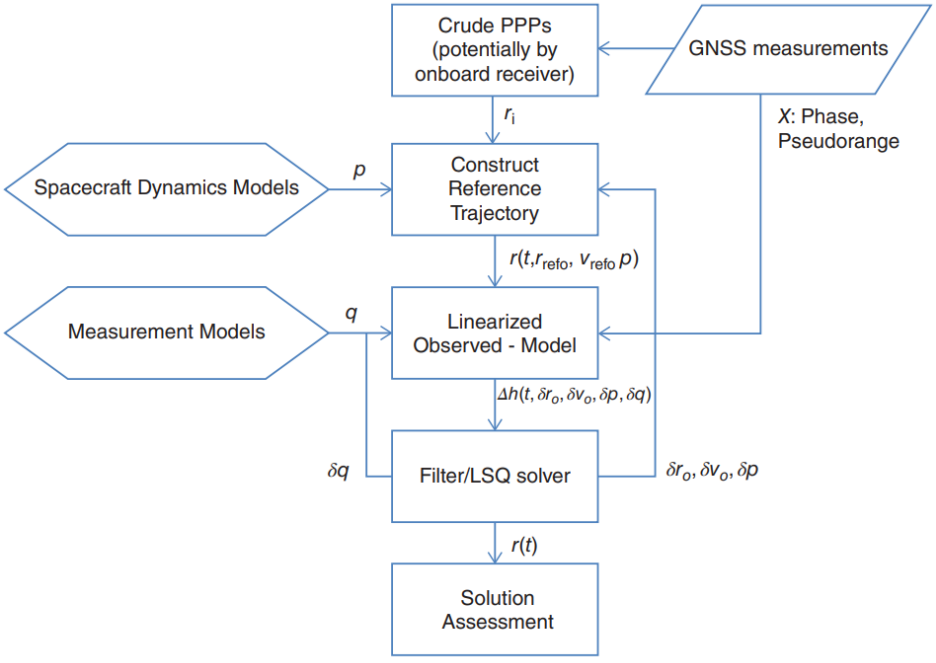


Figure 2.1: Flowchart of the LEO POD process. Image Credit: (Bar-Sever, 2021)

For a reference trajectory, $\boldsymbol{r}_{ref}(t)$, with initial state and associated parameters $\boldsymbol{p}_{ref}$, we form $\delta\boldsymbol{r}(t) = \boldsymbol{r}(t) - \boldsymbol{r}_{ref}(t)$ as the difference between the true trajectory and the reference orbit. In order to effectively determine a solution, this difference must be within the linear regime. In a similar

manner, we can define a correction to the initial states; $\delta \boldsymbol{r_0}$, $\delta \boldsymbol{v_0}$, $\delta \boldsymbol{p}$, and $\delta \boldsymbol{q}$. Thus Equation 2.5 can be linearized as

$$\boldsymbol{X}(t) = \boldsymbol{h}(\boldsymbol{r}_{ref0}, \boldsymbol{v}_{ref0}, \boldsymbol{p}_{ref}, \boldsymbol{q}_{ref}, t) + \nabla \boldsymbol{h}(\boldsymbol{r}_{ref0}, \boldsymbol{v}_{ref0}, \boldsymbol{p}_{ref}, \boldsymbol{q}_{ref}, \delta \boldsymbol{r_0}, \delta \boldsymbol{v_0}, \delta \boldsymbol{p}, \delta \boldsymbol{q}, t) + \boldsymbol{w} \tag{2.6}$$

where $\nabla \boldsymbol{h}$ is the first-order term of a Taylor series expanded about the reference values at each epoch in time $t$. This corresponds to the third box in Figure 2.1. The correction terms, $\delta \boldsymbol{r_0}$, $\delta \boldsymbol{v_0}$, $\delta \boldsymbol{p}$, and $\delta \boldsymbol{q}$, can now be solved for directly, since Equation 2.6 is now invertible. The correction terms are added to the initial conditions of the reference trajectory, and the solution can be considered solved. In many cases, it is useful to iterate upon the reference trajectory. Advanced orbit determination software such as GipsyX (Bertiger et al., 2020) allows the user to implement a number of options during this step. For example, it is possible to specify measurement post-fit residual windows that will exclude outliers from the next iteration on the reference trajectory.

In the solution above, the measurement model vector $\boldsymbol{q}$ contains the receiver clock state. All clocks are stochastic in nature, and the inclusion of additional clock states such as frequency bias and frequency drift can be included but is not necessary for POD. The reason for this is two-fold: the stochastic nature of the clock is difficult to assess, and the abundance of GNSS measurements makes the clock bias highly observable. The second point allows for the clock to be estimated as a stochastic white noise process with a new unconstrained clock state estimate at each epoch or eliminated entirely with double differences. While stochastic clock estimates increases the number of states to be estimated by the number of measurement epochs, with the abundance of GNSS measurements in both ground and LEO scenarios, the impact on the solution is small.

### 2.2.2 Orbit Determination Strategies

When solving the orbit determination problem, there are several strategies available. These can be broken down into three categories: dynamic, kinematic, and reduced-dynamic. In the the dynamic solution strategy, when the force models are well understood, the force model vector $\boldsymbol{p}$ is a

simple set of parameters which along with the initial state, $\boldsymbol{r_0}$, $\boldsymbol{v_0}$, uniquely defines the trajectory. As such, dynamic solutions assume that the force models largely capture the spacecraft motion and only solve for parameters such as the drag coefficient or the solar scale factor which are estimated as constants across the solution arc. As part of the dynamic solution, the phase measurement biases must still be estimated, and LEO clock states can be eliminated with double differences or estimated as stochastic parameters. Often times a simple dynamic approach does not result in sufficient accuracy, but can be improved with the addition of empirical forces. Errors in the force models typically result in state errors with a once-per-orbit frequency (Colombo, 1989). Custom empirical forces can model this effect as

$$\boldsymbol{f}_u = [C_u cos(\theta) + S_u sin(\theta)]\hat{\boldsymbol{u}} \tag{2.7}$$

$$\boldsymbol{f}_v = [C_v cos(\theta) + S_v sin(\theta)]\hat{\boldsymbol{v}} \tag{2.8}$$

$$\boldsymbol{f}_w = [C_w cos(\theta) + S_w sin(\theta)]\hat{\boldsymbol{w}} \tag{2.9}$$

where $C$ and $S$ are the estimated sine and cosine force amplitudes, position in the orbit is the argument of latitude $\theta$, and $\hat{\boldsymbol{u}}$, $\hat{\boldsymbol{v}}$, and $\hat{\boldsymbol{w}}$ are the component directions expressed in a fixed frame. Typically the amplitudes, $C$ and $S$, are estimated as constant across the solution arc in an orbit fixed frame (radial, cross-track, in-track) or a spacecraft body frame (body-x/y/z). This orbit solution is still considered dynamic as the trajectory is uniquely defined by the initial state, $\boldsymbol{r_0}$, $\boldsymbol{v_0}$, and force model parameters $\boldsymbol{p}$.

The kinematic approach extends the white noise modeling beyond just the clock to the position states as well. In this case, the spacecraft dynamic models are completely ignored and the spacecraft position becomes a parameter of the measurement model, and the position at each epoch is determined only by the observations at the corresponding epoch. In this method, the solution is wholly dependent on the observations. This approach is typically not as accurate as other solutions that do incorporate satellite dynamical models. However, because it is primarily dependent on the

observation models, differences between kinematic and dynamic solutions can be used to identify potential modeling errors in in either the measurement model or the dynamic models.

The reduced dynamic technique allows for the compensation of force model errors through the estimation of stochastic force model parameters (Wu et al., 1991) taking an in-between approach between the dynamic and kinematic. The stochastic parameters can be tuned so that the orbit solution is guided by the modeled dynamics while leveraging the accuracy of the numerous GNSS measurements. In the reduced dynamic technique, states or custom forces are formulated in terms of either a random process with exponentially correlated process noise or random walk. Following Bierman (2006), a first-order Gauss-Markov process, $p(t)$, can be described in terms of an exponential autocorrelation

$$R(\Delta t) = E(p(t), p(t + \Delta t)) = \sigma^2 e^{-\Delta t/\tau} \tag{2.10}$$

where $\sigma^2$ is the steady-state uncertainty, $\tau$ is the correlation time, and $\Delta t$ is the update interval. The evolution of $p(t)$ is given by

$$p(t_{i+1}) = mp(t_i) + w \tag{2.11}$$

where

$$m = e^{-(t_{i+1}-t_i)/\tau} \tag{2.12}$$

and the process noise $w$ is zero mean with expected variance given by

$$E(w^2) = \sigma^2(1 - m^2) \tag{2.13}$$

The custom force model parameters such as those in Equations 2.7 - 2.9 can be updated as Gauss-Markov process and implemented as piecewise constant forces over the update interval $\Delta t = t_{i+1} - t_i$. The user chooses four parameters for the stochastic estimation: the *a priori* uncertainty, the process noise uncertainty added at each update, the update interval $\Delta t$, and the

correlation time $\tau$. These are typically derived empirically through trial and error and tuned using large data sets. For a zero correlation time, $\tau = 0$, then $m_i = 0$ and $w_i = \sigma$ which becomes a white-noise process. For the case $\tau = \infty$, then $m_i = 1$ and $w_i = 0$ which becomes dynamic tracking. The reduced dynamic approach, when tuned correctly, often allows for the most accurate orbit solutions to be achieved (Wu et al., 1991; Haines et al., 2004; Montenbruck et al., 2005; Bertiger et al., 2010a) through its ability to capture signals present in the observations but not modeled in the dynamics.

## 2.3 Solution Assessment

One of the challenges of the POD solution process is the validation of the orbit solutions. When available, the most valuable reference for evaluation of GNSS-based POD solutions is independent SLR observations (Pearlman et al., 2019). Despite being only a one dimensional measurement of the two-way range between the satellite and the SLR ground station, the use of SLR measurements allows for bounds on the orbit accuracy to be established by examination of the one-way SLR residual rms.

Without an independent measure of orbit accuracy, such as SLR measurements or sea surface height crossovers, it is difficult to fully evaluate the orbit solutions. However, internal metrics can be used to evaluate the orbit solution precision. The two most common internal metrics are the post-fit residual rms, and the orbit overlap difference rms. White noise post-fit residual rms that match the expected measurement noise indicate a well modelled and tuned filter. If significant structure exists in the post-fit residual rms, it is often an indication of poor modeling of either the dynamics or measurements. For example, a daily fit residual rms that is correlated with the sun elevation with respect to the orbit plane (beta angle) would likely be an indicator of poor solar radiation pressure modeling.

Orbit overlaps provide a way to evaluate the precision or consistency of the POD solutions over time. They are computed from the six hours of overlap that occur for 30-hour daily solution arcs centered at noon GPS time. A single rms value can be computed for each of the component differences during the overlap period as seen in Figure 2.2. To avoid edge effects from the reduced

dynamics, one hour from each of the tails is excluded and only the central four hours are used for the rms computation. Orbit overlaps are assumed to provide a lower bound on the accuracy, but in general are optimistic as they are unable to account for systematic errors in the solution common to the two overlapping solution arcs.

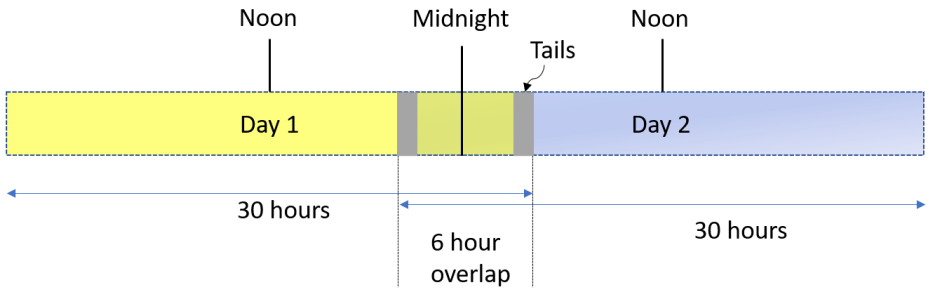


Figure 2.2: Orbit overlaps are constructed by using 30-hour arcs centered at noon. This results in 6 hours of overlap for two 30-hour arcs

## 2.4 Summary

The description above outlined the standard elements of GNSS-based POD. In the following chapters, the techniques described above are applied to the CYGNSS, GRACE, Sentinel-6 MF, and Jason-3 spacecraft. The next chapters detail additional modeling and methods that have been implemented or advanced to improve GNSS-based POD. Specifically, a receiver antenna calibration is discussed in more detail in Chapter 3, which is part of the measurement models discussed above. Chapter 4 examines the reduced-dynamic approach using single-frequency measurements and orbit solution assessment for CYGNSS. Sentinel-6 MF, on the other hand, is primarily focused on the background models. In particular, we discuss an improvement to the dynamical models for solar radiation pressure and an estimation of a GPS IIIA antenna calibration for use in LEO POD. These methods are then applied to an evaluation of POD solutions from the two independent GNSS receivers onboard Sentinel-6 MF and the benefits of a multi-receiver/GNSS POD solution.

# Chapter 3

# Antenna Calibration

## 3.1 Background

The transition from relative to absolute PCO (phase center offset) and PV (phase variaion) modeling for the GNSS satellite transmitter antennas (Schmid et al., 2005, 2007) allowed for more consistent orbit and clock products and paved the way for ambiguity resolution (Bertiger et al., 2010b) through better phase modeling. Signals emitted by a transmitting antenna and then captured by a GNSS receiver experience different effective delays based on the signal line-of-sight direction. These line-of-sight variations are a result of both the physical antenna pattern (Aparicio et al., 1996) and multipath due to the spacecraft structure (Young et al., 1985). Both the pseudorange and carrier phase measurements are affected, but in different ways. By convention, the variations for the phase are often decomposed into a mean PCO and a set of elevation and azimuth dependent PVs (Schmid et al., 2005; Montenbruck et al., 2009; Jäggi et al., 2009). The PCO is effectively the center of a best-fit sphere to the total antenna calibration and represents the mean offset of the wave front from the antenna reference point. The PVs, on the other hand, are azimuth and elevation dependent distortions to the wave front. This same decomposition can be applied to code group delays, and in analogous terms would be described as the mean group delay offset and group delay variations. However, because the formulation is the same (mean offset plus line-of-sight variations), for the remainder of this thesis, the PCO-PV terminology will be used for all calibrations but explicitly referenced to the observation type.

For missions that have strict orbit accuracy requirements, pre-flight antenna phase pat-

terns are often derived from anechoic chamber measurements. For example, as part of a terrestrial frame realization, Haines et al. (2015) used the pre-launch measurements from GRACE and TOPEX/Poseidon choke ring antennas which were measured in isolation. Antenna calibrations measured in this way are often limited in their ability to fully capture spacecraft multipath effects. For this reason, it is beneficial to re-estimate the antenna calibration from in-flight tracking data. Using the pre-flight antenna calibrations provide and important reference for the nominal or *a priori* PCOs. In this thesis, when available, it is used as the *a priori* calibration for the in-flight calibration. Additionally, antenna calibrations derived from anechoic chamber measurements provide a way to constrain the estimated in-flight PCOs when they are not observable.

To achieve the most accurate POD solutions, PCO and PV calibrations are applied to both the transmitting and receiving antennas. The International GNSS Service (IGS) provides a unique PCO product for each GNSS satellite that is linked to the IGS realization of the International Terrestrial Reference Frame (ITRF). The IGS PVs, however, are currently modeled identically for every satellite within a GPS sub-block and only describe variations as a function of boresight angle (Montenbruck et al., 2015a). Because the GNSS transmitters nominally point towards the Earth geocenter and the LEO receiver antenna typically point in the opposite direction, the resulting antenna calibrations are highly correlated in elevation. Because of this, without some judicious constraint such as described by Haines et al. (2015), an estimated LEO antenna calibration will inherently be linked to the applied transmitter PCOs and PVs. As such, potential GNSS PV elevation dependent errors can easily be absorbed during estimation of the receiving antenna calibration. However, as long as the LEO and transmitter calibrations are consistent, it will have little effect on the POD.

## 3.2 Antenna Calibration Description

The antenna calibration function can be formulated in terms of the mean PCO and a set of line-of-sight azimuth and elevation dependent variations. Rothacher et al. (1995) showed that there are inherent degrees of freedom for a PCO vector $\mathbf{r}_0$ and PV function $\phi(az, el)$ such that any

set can be transformed into a new PCO and PV function using the following:

$$\mathbf{r}_0' = \mathbf{r}_0 + \Delta\mathbf{r} \tag{3.1}$$

$$\phi'(az, el) = \phi(az, el) - \Delta\mathbf{r} \cdot \hat{\mathbf{e}} + \Delta\phi \tag{3.2}$$

where $\Delta r$ and $\Delta\phi$ (constant phase offset) can be chosen arbitrarily and $\hat{\mathbf{e}}$ is a unit vector in the line of sight direction from the receiver to the transmitter. From this, it can be seen that the antenna PCO is somewhat arbitrary, and it is possible to induce or remove an offset through the PV function alone. Unless constrained, when estimating the PVs, they will absorb any mean offset relative to the antenna reference point. In general, when the offsets are observable, allowing the PVs to capture these effects is the preferred method since it does not need to factor in the weighting that occurs with different observation densities as a function of azimuth and elevation. When this is not the case, and the *a priori* is trusted, constraints can be applied to preserve the offsets in the *a priori* PV function.

### 3.2.1 Antenna Calibration Estimation

In-flight antenna calibrations can be estimated either by residual stacking or direct estimation within the POD filter. Residual stacking estimates the calibrations by averaging post-fit residuals in discrete azimuth and elevation bins based on the transmitter line-of-sight direction. Haines et al. (2004) showed that the use of in-flight estimated antenna calibrations from residual stacking improved the POD accuracy when applied to Jason-1. However, Jäggi et al. (2009) showed that the direct approach is superior to residual stacking. The preferred method here is the direct approach where the orbit, receiver clock, carrier ambiguities, and PVs are all estimated together.

The receiver antenna calibration is estimated from daily solutions generated from 24-hour dynamic orbit estimates. Outliers must first be removed as they can significantly influence the receiver calibration, especially for bins with low measurement density. This is done using a dynamic solution with *a priori* PVs to simply detect the outliers. With these observations excluded, a new dynamic orbit solution is run that also simultaneously estimates corrections to the *a priori*

Table 3.1: POD estimation strategy for antenna calibrations

| Estimated Parameters | Parameterization | *a priori* $\sigma$ |
|---|---|---|
| **Dynamic Solution (Outlier Detection)** | | |
| Drag Coefficient | Bias per arc | 1000 |
| Once-per-orbit cross-track (cos, sin) | Constant per arc | 1 $mm/s^2$ |
| Once-per-orbit in-track (cos, sin) | Constant per arc | 1 $mm/s^2$ |
| **Dynamic Solution (Calibration Estimation)** | | |
| Drag Coefficient | Bias per arc | 1000 |
| Once-per-orbit cross-track (cos, sin) | Constant per arc | 1 $mm/s^2$ |
| Once-per-orbit in-track (cos, sin) | Constant per arc | 1 $mm/s^2$ |
| Antenna Calibration Vertices | Constant per arc | 10 $m$ |
| **Carrier Phase Bias** | Constant bias per continuous carrier track | 1e6 km |
| **Clock Offset** | White-noise Process | 3e5 km |

two-dimensional receiver antenna calibration. Table 3.1 shows the antenna calibration estimation strategy including daily estimates of drag coefficient and once-per-orbit accelerations in the cross-track and in-track directions.

The antenna calibrations within GipsyX can be estimated for any observable type, such as a single-frequency code or phase, or an ionosphere-free linear combination. This is done by computing a grid of calibration values on azimuth and elevation vertices. Application within the filter then uses a bi-linear interpolation to correct each measurement based on the line-of-sight azimuth and elevation.

The final antenna calibration is estimated by accumulating the daily Square Root Information Filter (SRIF) state outputs into a single estimate. The SRIF accumulation process accounts for both the uncertainties in the daily estimate's vertices as well as the cross-correlation between the vertices to produce a final state estimate for each vertex along with its corresponding uncertainty. After data assimilation, if any constraints are required, they are applied to the final combined output.

### 3.2.2 Constraints

The process of estimating an antenna calibration produces a correction to the *a priori* calibration. We can rewrite Equation 3.2 to be only in terms of the estimated correction, $\Delta\phi'(az, el)$, relative to the *a priori* values. This results in

$$\Delta\phi'(az, el) = \Delta\phi(az, el) - \Delta\mathbf{r} \cdot \hat{\mathbf{e}} + \Delta\phi \tag{3.3}$$

where the final antenna calibration is given by

$$\phi(az, el)_{final} = \phi(az, el)_{apriori} + \Delta\phi'(az, el)_{constrained} \tag{3.4}$$

The constraints are applied only to the observed correction term $\Delta\phi'(az, el)$ in Equation 3.3. The first parameter to be constrained is $\Delta\phi$. This term cannot be separated from the phase biases as it is a constant term that is added to all line-of-sight observations equally (or clock for code calibrations). This can easily be constrained by setting the calibration along the boresight direction to zero. However, due to the low density of observations for LEO spacecraft in the boresight direction, it is more reliable to level the entire antenna calibration correction, $\Delta\phi'(az, el)$, by constraining the average of all bins above 30 degrees elevation to zero. This choice of the 30 degree elevation cut-off is somewhat arbitrary, but is chosen as it covers a large set of well defined vertices. The constraint is formulated as follows

$$\Delta\phi'(az, el)_{constrained\Delta\phi} = \Delta\phi'(az, el) - \sum_{az=0^\circ}^{360^\circ} \sum_{el=30^\circ}^{90^\circ} \Delta\phi'(az, el) \tag{3.5}$$

where $\Delta\phi'(az, el)_{constrained\Delta\phi}$ is the constrained correction to the *a priori* calibration.

For spacecraft with yaw-fixed attitudes, it is difficult to resolve the mean PCO aligned with in the in-track direction. This issue has previously been observed in estimation of the horizontal PCOs for GNSS satellites during periods when the spacecraft attitude aligns one of the body axes with the in-track direction (Schmid et al., 2007; Huang et al., 2022). For cases where there is *a priori* information, constraining the PCO of the antenna axis aligned with the in-track direction to

zero is suggested. For the example where the antenna-x direction is aligned with the orbit in-track direction, this can be done by forcing $\Delta\mathbf{r} = [\Delta x = 0, \Delta y, \Delta z]$. Here the receiver antenna calibration correction, $\Delta\phi'(az, el)$, can absorb offsets in the body-y and z components, but not for the body-x offset.

To formulate the constraint in terms of the antenna calibration correction, we must first derive a method for computing the equivalent antenna-x/y/z PCOs contained in $\Delta\phi'(az, el)$. Each point in the antenna calibration correction can be converted from polar coordinates and projected into the antenna frame x, y, and z components using

$$\Delta x_{az,el} = \Delta\phi'(az, el)cos(az)cos(el) \tag{3.6}$$

$$\Delta y_{az,el} = \Delta\phi'(az, el)sin(az)cos(el) \tag{3.7}$$

$$\Delta z_{az,el} = \Delta\phi'(az, el)sin(el) \tag{3.8}$$

The mean offset contained in the antenna calibration correction, assuming equal weighting of the vertices, can be formulated as follows

$$x_{off} = \sum_{az=0^\circ}^{360^\circ} \sum_{el=0^\circ}^{90^\circ} \Delta\phi'(az, el)cos(az)cos(el)/n \tag{3.9}$$

$$y_{off} = \sum_{az=0^\circ}^{360^\circ} \sum_{el=0^\circ}^{90^\circ} \Delta\phi'(az, el)sin(az)cos(el)/n \tag{3.10}$$

$$z_{off} = \sum_{az=0^\circ}^{360^\circ} \sum_{el=0^\circ}^{90^\circ} \Delta\phi'(az, el)sin(el)/n \tag{3.11}$$

where $n$ is the number of vertices contained in $\Delta\phi'(az, el)$.

The formulation of the constraint requires that the partials be computed relative to the state, which in this case are the antenna calibration vertices of $\Delta\phi'(az, el)$. The constraint for the x-offset then becomes

$$\frac{\partial x_{off}}{\partial \Delta\phi'(az,el)} = cos(0^\circ)[cos(0^\circ) + ... + cos(90^\circ)] + ... + cos(360^\circ)[cos(0^\circ) + ... + cos(90^\circ)] = 0 \quad (3.12)$$

This constraint is applied to the normal equations in the SRIF state output using a user defined $\sigma$. As a note, the division by the number of elements, $n$, can be dropped so long as the constraint value is zero.

## 3.3 Summary

The estimation of a receiver antenna calibration is an important aspect of the POD process. In the following research, for each spacecraft, it the first step taken where a separate antenna calibration for all observation types is estimated. For Sentinel-6 MF, this includes calibrations for each of the ionosphere-free phase and pseudorange combinations. It allows for the removal of systematic line-of-sight variations from the measurements. In the case of CYGNSS, where the GRAPHIC observable is used, this variability is on the order of one meter. For Sentinel-6 MF, it is important for accurate phase modeling in the ambiguity resolution process.

# Chapter 4

# Improved GPS-Based Single-Frequency Orbit Determination for the CYGNSS Spacecraft Using GipsyX

## 4.1 Introduction

Satellite missions requiring high accuracy orbit solutions are typically equipped with scientific-grade dual-frequency GNSS receivers. This allows for precise phased-based measurements and the direct removal of ionospheric effects. Even some small satellites like the 3U CubeSats flown by Spire (Nguyen et al., 2020) have this capability, which is used to produce a variety of science data products. However, there are also LEO missions where precise orbit solutions are not a priority. These satellites are often equipped with only single-frequency GNSS capability to support basic navigation and timing functions derived primarily on pseudorange observations rather than the phase. Space-capable single-frequency receivers with positioning accuracies of 10 m are readily available (Montenbruck et al., 2012) and function well, meeting the lower cost, weight, power, and telemetry constraints for small spacecraft.

CYGNSS is a constellation of eight small satellites, each equipped with a GNSS Reflectometry (GNSS-R) instrument consisting of a SGR-ReSI receiver, a zenith antenna for conventional direct signal tracking and formation of navigation solutions, and two downward-looking antennas capable of measuring GPS reflections from the surface of the Earth (Ruf et al., 2012). While CYGNSS was designed to use GNSS-R to measure ocean surface wind speed, it also provides an opportunity to study the feasibility of using GNSS-R for ocean altimetry to measure patterns of ocean circulation and sea level change. For the ocean altimetry application, the delay of the reflected GPS signal

must be precisely and accurately measured. Previous work (Mashburn et al., 2020; Li et al., 2018, 2019) identified uncertainty in the knowledge of CYGNSS satellite orbit solutions as a significant source of error for GNSS-R altimetry. Consequently, a focused effort to analyze and improve the CYGNSS orbit estimates was undertaken.

Most of the POD processes and techniques described in Chapters 2 and 3 are applicable to POD with single-frequency observations; however, without dual-frequency observations, it requires an alternative approach for mitigation of ionospheric effects and cannot easily take advantage of single receiver carrier phase integer ambiguity resolution. The latter limitation reduces the effectiveness of purely kinematic solutions. To address the ionospheric effects, three basic approaches have been well-established: modeling based on ionospheric density databases, estimation based on the divergence in code and carrier observations, and direct removal of the ionospheric effects by combining code and carrier observations into the GRAPHIC observable.

Model-based methods approximate ionospheric effects using measurement based Global Ionosphere Maps (GIM) (Hernández-Pajares et al., 2009) or empirical models such as the International Reference Ionosphere (IRI) (Bilitza et al., 2017; Bock et al., 2009; Montenbruck and Gill, 2002). The GRAPHIC method (Yunck, 1993; Montenbruck, 2003) eliminates first order ionospheric effects directly by adding code-based pseudorange and carrier-based measurements together. This produces an ionosphere-free observable with a fixed ambiguity per pass and error dominated by half the noise in the pseudorange measurement. This approach is effective and widely used.

Early single-frequency POD of the TOPEX/POSEIDON spacecraft achieved radial accuracies of 4 to 5 cm (Muellerschoen et al., 1994) with GRAPHIC. Subsequent studies (Montenbruck et al., 2005; Bock et al., 2009) achieved full 3-D accuracies below 10 cm. Because GRAPHIC incorporates code-base pseudorange as part of the primary observable, the noise and group delay in the code have a greater effect on the solution than is seen in dual-frequency ambiguity-resolved POD solutions. Shao et al. (2019) demonstrated further improvements by reducing systemic errors with an antenna calibration for the GRAPHIC observable, generated with a residual stacking approach. They achieved 3-D accuracies better than 5 cm for the GRACE-B satellite.

The goal of our work was to improve the CYGNSS orbit solutions and quantify the precision and accuracy of the results in support of GNSS-R altimetry research. As part of this effort, we introduce a method for correcting a clock-like signal in the CYGNSS raw carrier measurements that is not present in the pseudorange. This correction allows for implementation of the GRAPHIC orbit solutions. We estimate code-only and GRAPHIC observable antenna calibrations directly within a dynamic POD filter and demonstrate performance of single-frequency model-corrected code-only and GRAPHIC orbit solutions in the GipsyX software environment.

While GipsyX is primarily used with dual-frequency GNSS measurements, we show that it can also be configured to produce accurate single-frequency POD. To demonstrate the methods for CYGNSS, we have selected GRACE-B as the primary reference satellite. The GRACE mission, at a similar altitude to CYGNSS, provides extensive sets of high-quality dual-frequency observations that are readily available, as well as previously established high precision orbit solutions. The GRACE-B satellite orbit and GPS measurements are used to directly evaluate errors associated with L1 single-frequency POD strategies that we apply to CYGNSS. In addition to GRACE-B, we also consider the higher altitude Sentinel-6 Michael Freilich (MF) spacecraft to provide an additional dual-frequency reference. Like GRACE, the Sentinel-6 MF altimetry mission is highly dependent on accurate orbit solutions and provides a reference for the L1 single-frequency POD errors. While our results for this mission are less extensive, they provide a useful reference point because Sentinel-6 MF flies at a 66 degree inclination, more similar to CYGNSS than the GRACE polar orbit.

The remainder of this chapter is organized into three main sections. Section 4.2 describes the background models and methods for LEO POD within GipsyX, including the specifics of the GRACE and CYGNSS missions, estimation strategies, antenna calibration, and issues encountered with the CYGNSS phase measurements. Section 4.3 presents the results, including estimated antenna calibrations, followed by an orbit precision and accuracy assessment using internal metrics of residual post-fit rms and orbit overlaps for GRACE and CYGNSS, and external metrics for GRACE by comparing to the dual-frequency solutions. We also use a small set of Sentinel-6 MF

orbit solutions to support the assessment of CYGNSS GRAPHIC solutions. Finally, the conclusions in section 4.4 summarize the findings of this work.

## 4.2 Methods

### 4.2.1 CYGNSS, GRACE, and Sentinel-6 MF comparison

Table 4.1 shows a comparison of the key features of the GRACE-B, CYGNSS FM05, and Sentinel-6 MF satellites, orbits, and onboard GPS receivers. Both the 8-satellite CYGNSS constellation and GRACE A and B pair of satellites operate in the LEO regime in near circular orbits, with CYGNSS being about 50 km higher in altitude. They have similar attitude profiles with a nominal yaw-fixed orientation relative to the flight direction. The biggest difference between GRACE and CYGNSS orbits is that GRACE is in a polar orbit, while CYGNSS is in a low inclination orbit (35 degree) driven by its mission to observe ocean surface winds linked to cyclones. Sentinel-6 MF is much higher than both GRACE and CYGNSS, but like CYGNSS is not in a polar orbit (inclination of 66 degrees).

Table 4.1: Comparison of GRACE-B, CYGNSS FM05, and Sentinel-6 MF

| | **GRACE-B** | **CYGNSS FM05** | **Sentinel-6 MF** |
|---|---|---|---|
| Altitude | 455 - 478 km | 514 - 528 km | 1336 km |
| Inclination | 89 degrees | 34.8 degrees | 66 degrees |
| Eccentricity | $< 0.005$ | $< 0.003$ | $< 0.001$ |
| Mass | 487.2 kg | 28.9 kg | 1191 kg |
| Receiver | Blackjack GPS Receiver | SSTL SGR-ReSI Receiver | TriG GNSS Receiver |
| GPS Signals | L1W, L2W | L1C | L1W, L2W |
| Tracked | C1C, C1W, C2W | C1C | C1C, C1W, C2W |
| Year | 2009 | 2019 | 2021 |

Each CYGNSS satellite is equipped with a Surrey Satellite Technology Ltd. (SSTL) Space GPS Receiver Remote Sensing Instrument (SGR-ReSI) receiver that determines the satellite position in real time using civil single-frequency GPS (L1 C/A) signals (Unwin et al., 2013)). Since the primary mission is not reliant on precise knowledge of the CYGNSS orbit, only the onboard GPS

instantaneous navigation (Nav) solution was originally downlinked. The Nav solution is noisy with $1\sigma$ 3-D position errors of approximately 3 m. To enable an evaluation of altimetry applications, the satellite flight software was updated (July 2019) to also downlink the individual GPS satellite pseudorange and carrier phase measurements at 15 second intervals. At the time of writing, these lower-level GPS data are only available in the CYGNSS Level-0 data product, accessed by special request for this investigation. The availability of these raw tracking measurements provides the opportunity to estimate the CYGNSS orbit solution on the ground using advanced post-processing techniques in GipsyX or other POD software.

The Blackjack GPS Receiver flown on GRACE is designed specifically for geodetic-quality POD. It uses advanced codeless techniques to track L1 C/A and P(Y) pseudorange and carrier as well as L2 P(Y) pseudorange and carrier (Montenbruck and Kroes, 2003; Dunn et al., 2002). The receiver is coupled with a flush-mounted choke-ring antenna to reduce multipath reflections. The overall measurement approach promotes more precise measurements than typical receiver implementations geared to support real-time onboard navigation and timing. The Sentinel-6 MF spacecraft is equipped with a TriG receiver also capable of tracking L1 C/A, P(Y), and L2 P(Y) measurements (Donlon et al., 2021a). With CYGNSS, GRACE, and Sentinel-6 MF tracking the L1 C/A code and carrier, we can apply the same data processing and orbit estimation methods to the three missions. The observed C/A code noise without post-processed carrier smoothing for both GRACE and Sentinel-6 MF is below 30 cm based on post-fit residual rms. For CYGNSS it is significantly larger with a value around 1 m. Finally, to ensure comparable ionospheric effects for both GRACE and CYGNSS, we selected data sets for each mission near solar minimum, using data from early 2009 for GRACE and the last half of 2019 for CYGNSS.

### 4.2.2 GRAPHIC Observable

The GRAPHIC method is well established as an effective approach for creating an ionosphere-free observable from single-frequency GNSS measurements (Bock et al., 2009). The GRAPHIC observable is formed from the pseudorange, $\rho$, and carrier phase, $\phi$ by computing the mean of the

two measurements as follows

$$\rho = r + b + I + \varepsilon_\rho \tag{4.1}$$

$$\phi = r + b - I + N + \varepsilon_\phi \tag{4.2}$$

$$GRAPHIC = \frac{\rho + \phi}{2} = r + b + \frac{N}{2} + \frac{\varepsilon_\rho}{2} + \frac{\varepsilon_\phi}{2} \tag{4.3}$$

where $r$ is the geometric range, $b$ is the combined receiver and transmitter clock effects, $I$ is the ionosphere delay, and $\varepsilon$ is the measurement noise. This results in an ionosphere-free phase-like observable that contains half the code noise, half the phase noise, and half-integer ambiguities from the carrier measurements. While the GRAPHIC observable only contains half the code noise, this is substantially larger than what would be observed for typical carrier measurements. Bock et al. (2009) showed that a higher data sampling rate can mitigate the effect of the noise. Because GRAPHIC clock and carrier phase ambiguities cannot be separated, the raw (undifferenced) pseudorange is included to anchor the clock solution; but it is de-weighted by roughly five orders of magnitude relative to the GRAPHIC observable such that it does not significantly impact the final orbit solution. The half integer ambiguity that remains in the GRAPHIC observable can be estimated as a constant bias over the duration of the satellite transmitter pass.

### 4.2.3 GipsyX Orbit Modeling

Our single-frequency POD employs a high-fidelity gravity model, solid Earth tide, pole tide, ocean tides, and third-body effects as listed in Table 4.2. Non-gravitational effects are computed based on a custom macromodel constructed for each spacecraft, comprised of individual plates defined by their body frame normal vectors, areas and reflection properties (specularity and diffusivity). This model, along with knowledge of satellite attitude, provides input for computation of drag and radiation pressure forces on the spacecraft. Drag force is computed based on the DTM-2000 model, driven by the F10.7 cm solar flux and Kp geomagnetic indices to compute the atmospheric density (Bruinsma et al., 2003). Radiation pressure force is modeled for both solar (Milani et al., 1987) and Earth albedo (Knocke et al., 1988) radiation sources. GPS satellite ephemerides, clock

Table 4.2: Applied models for single-frequency POD

| **Model/Parameter** | **Selection** |
|---|---|
| GNSS observations | Undifferenced GPS L1 phase and C/A pseudorange<br>30-hour daily arcs<br>CYGNSS: 15-sec data rate<br>GRACE: 30-sec data rate |
| Surface forces | CYGNSS: Macromodel (Table 4.4 and Figure 4.1)<br>GRACE: Macromodel (Table 4.3) |
| Attitude | Measurement quaternions |
| Atmospheric density | DTM-2000 (Bruinsma et al., 2003) |
| GPS satellite antenna calibrations | IGS14 Values (Rebischung and Schmid, 2016) |
| Earth orientation/rotation | JPL IGS Analysis Center IGS14 Final Solutions |
| GPS spacecraft ephemerides | JPL IGS Analysis Center IGS14 Final Solutions |
| GPS spacecraft clocks | JPL IGS Analysis Center IGS14 Final Solutions<br>(Dietrich et al., 2018) |
| Planetary and lunar ephemerides | JPL DE421 ephemerides (Folkner et al., 2009) |
| Earth gravity field | EIGEN-GRGS.RL03-v2.MEAN-FIELD<br>(Rudenko et al., 2015) |
| Ocean tides | FES2004 tide model (Lyard et al., 2006) |
| Reference frame | IGS14 |

solutions, including Earth orientation parameters come from the JPL IGS Analysis Center Final products (Dietrich et al., 2018).

The GRACE macromodel has already been well-established in the GipsyX environment (Bertiger et al., 2020) and is shown in Table 4.3. For CYGNSS, we created a new macromodel

Table 4.3: GRACE Macromodel with body axis normal vector, area, specularity, and diffusivity

| Surface | Surface Normal [x,y,z] | Area ($m^2$) | Specularity | Diffusivity |
|---|---|---|---|---|
| Aft | [-1.000, 0.000, 0.000] | 0.9551 | 0.40 | 0.26 |
| Front | [1.000, 0.000, 0.000] | 0.9551 | 0.40 | 0.26 |
| Nadir | [0.000, 0.000, 1.000] | 6.0711 | 0.68 | 0.20 |
| Port-out | [0.000, -0.766, -0.643] | 3.1555 | 0.05 | 0.30 |
| Port-in | [0.000, 0.766, 0.643] | 0.2283 | 0.40 | 0.26 |
| Starboard-out | [0.000, 0.766, -0.643] | 3.1555 | 0.05 | 0.30 |
| Starboard-in | [0.000, -0.766, 0.643] | 0.2282 | 0.40 | 0.26 |
| Zenith | [0.000, 0.000, -1.000] | 2.1674 | 0.05 | 0.30 |

Table 4.4: CYGNSS Macromodel with body axis normal vector, area, specularity, and diffusivity

| Surface | Surface Normal [x,y,z] | Area ($m^2$) | Specularity | Diffusivity |
|---|---|---|---|---|
| 1 | [1.000, 0.000, 0.000] | 0.1132 | 0.470 | 0.380 |
| 2 | [-1.000, 0.000, 0.000] | 0.1132 | 0.296 | 0.264 |
| 3 | [0.000, 1.000, 0.000] | 0.0489 | 0.401 | 0.260 |
| 4 | [0.000, -1.000, 0.000] | 0.0489 | 0.408 | 0.260 |
| 5 | [0.000, 0.000, 1.000] | 0.5711 | 0.414 | 0.256 |
| 6 | [0.000, 0.000, -1.000] | 0.8155 | 0.371 | 0.255 |
| 7 | [0.000, 0.469, 0.883] | 0.1384 | 0.401 | 0.260 |
| 8 | [0.000, -0.469, 0.883] | 0.1384 | 0.407 | 0.260 |

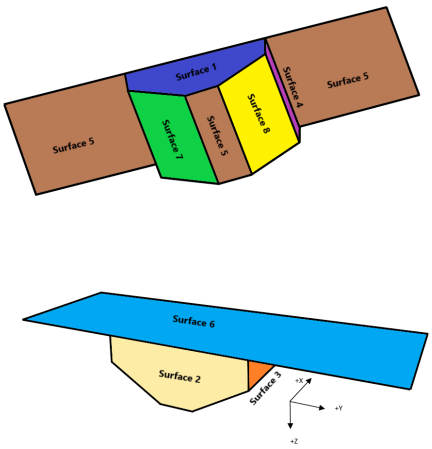


Figure 4.1: CYGNSS macromodel surfaces with each surface label corresponding to the values given in Table 4.4

with eight surface areas based on engineering drawings. Coefficients for their specular and diffuse reflectivity were estimated in GipsyX using dynamic orbit solutions over approximately 170 days. We then computed a weighted mean of the daily results, using the inverse of the filter formal errors, to arrive at the fixed values for CYGNSS specularity and diffusivity. The surface properties are listed in Table 4.4 and illustrated in Figure 4.1.

### 4.2.4 POD Processing Strategy

GipsyX offers a variety of options for orbit determination such as the use of empirical acceleration estimation, configurable reduced-dynamic models, and antenna calibrations (Bertiger et al., 2020). The implementation of empirical accelerations and reduced dynamics within the filter is described in more detail in Chapter 2.

We apply the same GipsyX POD strategy to both the code-only and GRAPHIC methods. Daily POD solutions are generated using 30-hour data sets centered at noon GPS time. A 30-hour measurement set allows for orbit evaluation using orbit overlaps as well as avoiding edge effects in the central 24 hours of the solution (Haines et al., 2004; Bertiger et al., 2010a) (see Figure 2.2).

Table 4.5: Precise Orbit Determination Strategy for GRACE and CYGNSS

| Estimated Parameters | Parameterization | *a priori* $\sigma$ |
|---|---|---|
| **Epoch State** | | |
| 3-D epoch position (X,Y,Z) | Bias per epoch | 10 $km$ |
| 3-D epoch velocity (X,Y,Z) | | 1 $km/s$ |
| **Empirical Acceleration (3 dynamic passes)** | | |
| Drag Coefficient | | 100 |
| Once-per-orbit cross-track (cos, sin) | Constant per 30-hr arc | 1 $mm/s^2$ |
| Once-per-orbit in-track (cos, sin) | | 1 $mm/s^2$ |
| **Empirical Acceleration (reduced-dynamic)** | | |
| Cross-track | Stochastic with $\tau$ = 6 hrs $\Delta$t = 30 min* | 1 $nm/s^2$ |
| Radial | Stochastic with $\tau$ = 6 hrs $\Delta$t = 30 min | 1 $nm/s^2$ |
| In-track | Stochastic with $\tau$ = 6 hrs $\Delta$t = 30 min | 1 $nm/s^2$ |
| Once-per-orbit cross-track (cos, sin) | Stochastic with $\tau$ = 6 hrs $\Delta$t = orbital period | 1 $nm/s^2$ |
| Once-per-orbit in-track (cos, sin) | Stochastic with $\tau$ = 6 hrs $\Delta$t = orbital period | 1 $nm/s^2$ |
| **Carrier Bias (GRAPHIC only)** | Constant bias per continuous carrier track | 1e6 km |
| **Clock Bias** | White-noise Process | 3e5 km |

*$\Delta$t is the update interval and $\tau$ is the correlation time.

GipsyX is initialized by first estimating a dynamic orbit fit to the navigation solution. This is followed up with a two-step iteration process using the pseudorange and phase measurements. The first iteration comprises three dynamic passes where the initial state and dynamic properties are updated after each iteration. This is followed by a final reduced-dynamic pass. The parameters for each estimation strategy are shown in Table 4.5. The a priori $\sigma$ sets the initial uncertainty of the filter. The predominant orbit errors, including those due to mismodeled dynamical effects such as drag and solar radiation pressure, manifest at a once-per-orbit frequency (Colombo, 1989). To account for these effects, once-per-orbit empirical accelerations in the cross-track and in-track directions are estimated. These parameters along with the drag coefficient are estimated as constant biases for each 30-hour data set in the dynamic passes. This is followed by a reduced-dynamic pass where stochastic radial, cross-track, and in-track accelerations are estimated with a correlation time of 6 hours and held constant across the update interval of 30 minutes. The constant amplitude once-per-orbit cross-track and in-track estimates from the dynamic pass are augmented by stochastic states with correlation times of 6 hours and update intervals of once-per-orbit. The reduced-dynamic pass enables the final orbit solution to follow the measurements more closely by allowing the stochastic estimates to slowly change during the 30-hour data set.

### 4.2.5 Antenna Calibration

Antenna calibrations as described in Chapter 3 are used to compensate for line-of-sight measurement biases (e.g., multipath) caused by the receiver antenna and its electromagnetic interaction with the spacecraft (Haines et al., 2004). We separately estimate code-only and GRAPHIC antenna calibrations for CYGNSS and GRACE within dynamic orbit solutions without constant, body-fixed empirical accelerations as these could induce undesirable offsets in the antenna calibration. For example, Jäggi et al. (2009) noted that a radial shift can occur due to a constant radial empirical acceleration which can be absorbed by the estimated PVs.

For this analysis, it is assumed that there is no *a priori* information regarding either the PCOs or the PVs. This is potentially problematic for yaw-fixed spacecraft, such as GRACE and

CYGNSS, where the in-track direction of the antenna calibration experiences reduced observability. Initial evaluation of the GRACE orbits showed a smaller than 2 cm in-track bias for the GRAPHIC orbits. However, the code-only antenna calibration produced a consistent in-track bias larger than 6 cm. A similar bias was observed between the CYGNSS code-only and GRAPHIC orbits. Given these results, we chose to constrain the spacecraft flight direction PCOs of the code-only antenna calibration for both GRACE and CYGNSS to zero.

The PCO-PV model described in Chapter 3 can be applied to both the phase and code data types with the code being highly susceptible to multipath errors resulting in much larger PVs (Haines et al., 2004). The estimation strategy for CYGNSS differs slightly from the description in Section 3.2.1. Instead, on the final pass, only the satellite orbit, clock, and calibration values are estimated, holding the previous dynamical estimates as fixed parameters. To account for the reduced measurement density in the zenith direction, the estimated antenna calibration vertices use a fixed spacing of 2 degrees for elevation and a variable azimuth spacing as shown in Table 4.6. This results in a total of 4242 vertices that are estimated from each 24-hour solution. The output of each daily solution is saved, and then accumulated into a final solution over the desired time span. It is during accumulation that constraints are applied to the PVs. Here we constrain the sum of $\phi(az, el)$ above 30 degrees elevation to be zero.

Table 4.6: Antenna calibration azimuth spacing as a function of elevation

| Elevation Range | 0° - 52° | 54° - 64° | 66° - 70° | 72° - 74° | 76° - 80° | 82° | 84° - 86° | 88° | 90° |
|---|---|---|---|---|---|---|---|---|---|
| Azimuth Spacing | 3° | 4° | 6° | 8° | 10° | 12° | 20° | 24° | 120° |

### 4.2.6 CYGNSS Clock Inconsistency

The first attempts at processing the CYGNSS measurements revealed an unexpected inconsistency between the pseudorange and carrier phase measurements. Typically, GPS pseudorange and carrier phase measurements made on the same receiver channel have the same clock offset,

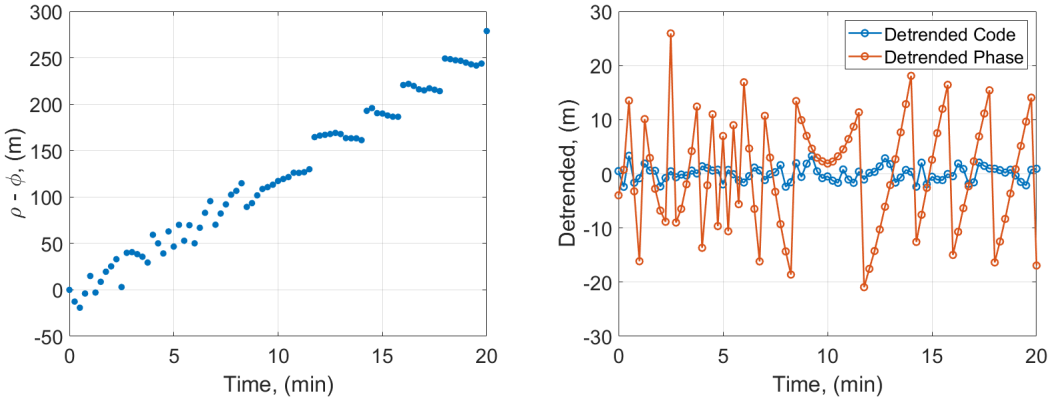


Figure 4.2: CYGNSS code/carrier divergence (left) and detrended code/carrier (right)

and diverge from each other systematically only due to the difference in the sign of the ionospheric effect as follows:

$$\rho - \phi = 2I - N + \varepsilon_\rho - \varepsilon_\phi \tag{4.4}$$

With CYGNSS however, we observed different apparent clock offsets in the pseudorange and carrier measurements, that were common across all simultaneously tracked GPS satellites. An example of the resulting pseudorange/carrier divergence is shown in Figure 4.2 (left) for a single satellite pass. This rate of divergence is much larger than would be expected due to ionosphere or noise alone, and it contains significant ramp/jump structure. When the code and phase are separately detrended, as shown in Figure 4.2 (right), the ramp/jump behavior is seen to be present in the phase measurements and not the code. To further isolate the effect, it is possible to process the pseudorange and carrier separately in GipsyX, solving for independent clock solutions, as shown in Figure 4.3. The left panel shows solutions for receiver clock offset over a full day using only the pseudorange (blue) and only the phase (red). The clock solution behavior revealed by the pseudorange data shows a relatively constant offset across the entire solution. This is quite typical for a GPS receiver and suggests that the receiver's internal oscillator is being steered to GPS time using the onboard navigation solution or that the measurements are compensated onboard for the estimated offset of the oscillator. In contrast, the clock behavior revealed by the phase data features a large linear drift of tens of km per day with jumps of tens of meters about the linear trend. A

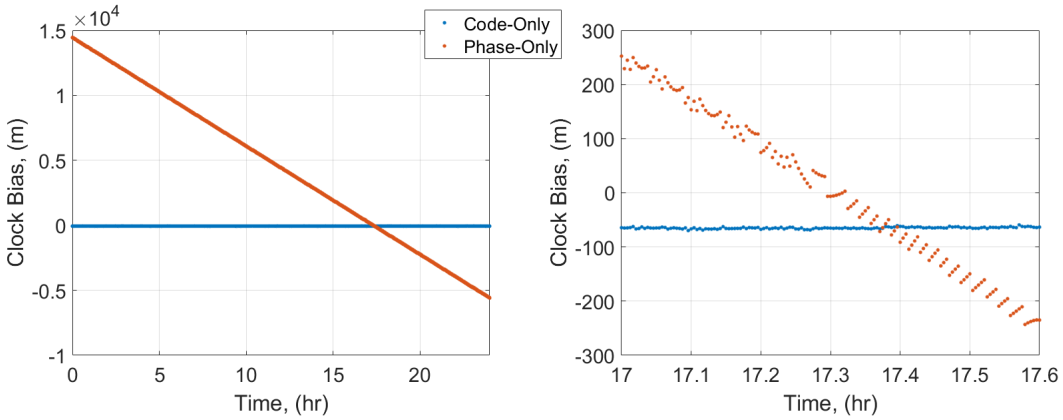


Figure 4.3: CYGNSS code-only (blue) and phase-only (red) clock solution comparison for a full day (left) and zoomed in for comparison (right), day of year (DOY) 191, 2019

zoomed in view, Figure 4.3 (right) shows similar observed behaviors as those in the detrended phase seen earlier in Figure 4.2.

These features in the phase-only clock solution suggest that the phase measurements are either uncorrected for the clock or corrupted in a clock-like way (or both)[1] . This precludes the use of conventional pseudorange/carrier divergence methods to estimate and remove the ionospheric effect and limits our analysis to just two approaches for compensating ionospheric effects in POD: either single-frequency code-only observation processing with ionospheric model corrections, or the GRAPHIC method. The GRAPHIC data combination will result in an apparent clock offset that is the average of the pseudorange and phase. With the SGR-ReSI phase vs pseudorange discrepancy, the issue that arises is that the phase measurements appear inconsistent with the time tags. Timing errors are correlated with in-track orbit errors, and in-track differences greater than 1 m were initially observed in GRAPHIC overlaps of the 30-hour POD solution arcs. Because of this, an effort was undertaken to correct the most significant portion of the clock inconsistency in the phase. Starting with Equation 4.4, the difference, $d$, is now modified to include the non-common

[1] We note that the phase data from the SGR-ReSI receiver are not needed to satisfy any of the mission requirements for the primary CYGNSS mission. The onboard GPS navigation solutions underpinning the primary science mission are conventional and use only the pseudorange measurements. That the phase measurements can be recorded and downlinked, however, is a useful feature for POD studies focused on value-added science (e.g., ocean altimetry).

clock-like phase error, $b_\phi$,

$$d = \rho - \phi = 2I - N + \varepsilon + b_\phi \tag{4.5}$$

To remove the integer ambiguity, we take the time difference for all tracked satellites, $k$, at time $t_i$ and $t_{i+1}$ as follows,

$$\Delta d^k(t_{i+1}) = d^k(t_{i+1}) - d^k(t_i) = 2\Delta I^k + \Delta\varepsilon^k + \Delta b_\phi \tag{4.6}$$

Because the $\Delta b_\phi$ term is common to all satellites, we can use the assumption that the median values at each measurement interval of $\Delta I$ and $\Delta\varepsilon$ are much smaller than $\Delta b_\phi$ and are near zero. We use the median because it is less susceptible to large outliers which can occur for low elevation satellites that experience significant changes in ionosphere over short periods of time. The phase clock term at any given time can then be constructed recursively using the median $\Delta\bar{d}(t_i)$ from $t_0$ to the desired time $t_i$, by initialized $b_\phi(t_0)$ with 0 and using

$$b_\phi(t_{i+1}) = \Delta\bar{d}(t_{i+1}) + b_\phi(t_i) \tag{4.7}$$

The left plot in Figure 4.4 shows a 10-minute span with the computed $\Delta d^k$ (orange) and the median values $\Delta\bar{d}$ (blue), along with the reconstructed phase clock term (right). The reconstructed clock term is then removed from the phase measurements. This creates a clock bias time history for the phase measurements that is much more consistent with the pseudorange measurements and,

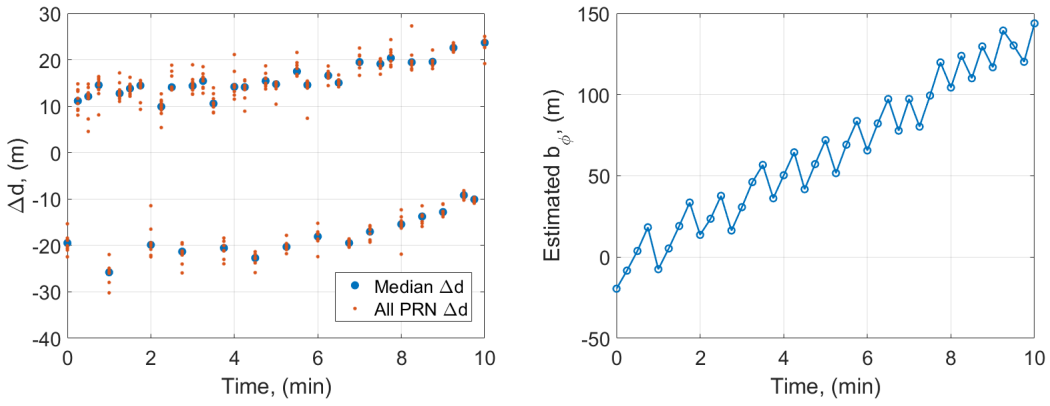


Figure 4.4: First difference of code minus phase (left) with all PRNs (red) and median (blue), and estimated phase clock error (right)

more importantly, consistent with the measurement time tags. The assumption of $\Delta I$ and $\Delta\varepsilon$ being near zero does not need to hold true in the short term, rather the sum only needs to stay near zero in the long term. It will still contain some residual ionosphere signal and measurement noise at each epoch, so this clock effect prevents us from determining the ionospheric effect based on code/carrier divergence. Fortunately, with this adjustment to the clock bias, we can now reliably employ the GRAPHIC approach to remove the ionospheric effects.

### 4.2.7 Code-Only Corrections

The processing of the code-only measurements requires additional corrections for the Timing Group Delay (TGD) bias and C1C-C1W differential code biases (DCB). These corrections are necessary to make the pseudorange measurements consistent with the standard clock products used in GipsyX which are referenced to P(Y) dual-frequency ionosphere-free measurements. An ionospheric correction is made using the IGS GIM to model the vertical total electron content (vTEC) (Hernández-Pajares et al., 2009), mapped to total TEC following the method described by Montenbruck and Gill (2002) with a few modifications. Where Montenbruck and Gill integrated a Chapman profile fit to the IRI model, we instead numerically integrate a single representative IRI2016 (Bilitza et al., 2017) distribution directly, with the purpose of estimating the fraction of the total ionosphere above the satellite. From this, the portion of the vTEC based on the GIM

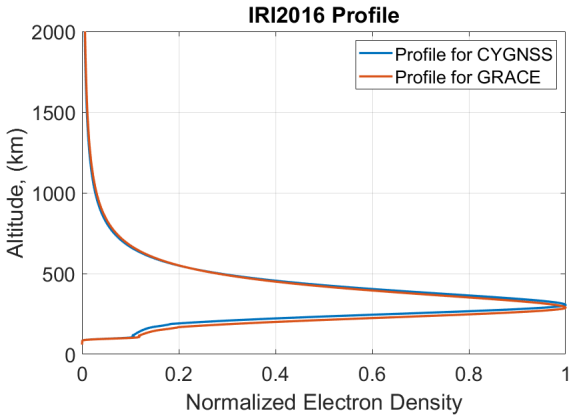


Figure 4.5: CYGNSS and GRACE IRI2016 normalized election density profile

is then mapped to correct the ionospheric delay in the LEO pseudorange. For both GRACE and CYGNSS we select a representative profile near the daily global TEC maximum. For GRACE, the reference IRI2016 profile is from April 9, 2009, at 12:00 UTC located at N 0 deg, E 20 deg, and for CYGNSS, October 2, 2019, at 12:00 UTC located at S 5 deg, E 25 deg. These two profiles are shown in Figure 4.5. One limitation of the IRI2016 model is that it does not converge to zero at the upper altitude limit of the model (2000 km). The remaining portion above 2000 km is small however, and we approximate it as zero above this altitude.

For a given LEO satellite with a height, $h_s$, the ionospheric pierce point, $h_{IP}$, is defined as the altitude where 50% of the total ionosphere above the satellite is located. This can be computed using the condition,

$$\sum_{i=h_s}^{h_{IP}} vTEC_i = \frac{1}{2} \sum_{i=h_s}^{2000km} vTEC_i \tag{4.8}$$

where $vTEC_i$ is the normalized electron density at altitude $i$ from the IRI2016 profile in Figure 4.5. This relationship along with the satellite altitude allows for the computation of the height of the ionospheric pierce point, $h_{IP}$. The remaining fraction, $\alpha$, of the $vTEC$ from the IGS GIM above the satellite can then be computed using,

$$\alpha = \frac{\sum_{i=h_s}^{2000km} vTEC_i}{vTEC_{total}} \tag{4.9}$$

Finally, the L1 C/A delay can be modeled using the mapping function as follows,

$$\Delta\rho_{L1} = \frac{\alpha}{sin(E_{IP})} \frac{40.3 m^2 s^{-2}}{c f_{L1}^2} vTEC_{GIM} \tag{4.10}$$

where $E_{IP}$ is the calculated elevation of the signal ray path at the intersection of the ionospheric pierce point. This produces an estimate of the ionosphere delay that can be removed from each measurement in a pure single-frequency code solution.

## 4.3 Results and Analysis

To demonstrate the single-frequency orbit solution methods proposed for CYGNSS, we processed 200 days of data for GRACE-B and 175 days of data for one of the eight CYGNSS satellites,

FM05, using the same models and solution strategies listed in Tables 4.2 and 4.5 for each. We limit the analysis here to a single satellite from the CYGNSS constellation to demonstrate the POD evaluation, but with the understanding that it can readily be applied to the rest of the CYGNSS constellation. For GRACE, 30-second C/A L1 measurements from DOY 1 – 200, 2009, were processed using the code-only and GRAPHIC methods. For CYGNSS FM05, 15-second C/A L1 measurements from DOY 190 – 365, 2019, were used. The CYGNSS data sets have several large gaps of approximately a day in length on DOY 212, 252 and 353. Large data gaps such as these, prevent the formation of 30-hour arcs of continuous data on either side of the missing data, resulting in 3 missing days for each gap. Additionally, we used a single day of Sentinel-6 MF data to investigate a cross-track anomaly observed in CYGNSS but not in GRACE.

The following subsections present the estimated code-only and GRAPHIC antenna calibrations for both GRACE and CYGNSS. Next, we examine the internal metrics consisting of daily post-fit measurement residual rms values along with the orbit overlap statistics. The GRACE code-only and GRAPHIC orbit solutions are compared to the dual-frequency orbits to evaluate the associated errors. Finally, we use the GRACE and Sentinel-6 MF errors to understand the potential errors associated with the CYGNSS POD.

### 4.3.1 Antenna Calibration

Figures 4.6 and 4.7 show the antenna calibrations estimated in GipsyX using the code-only and GRAPHIC methods for GRACE-B and CYGNSS FM05, respectively. Both sets of antenna calibrations exhibit significant systematic measurement biases. For GRACE, the code multipath effects can cause errors on the order of 30 to 40 cm and for CYGNSS, the variability is as high as several meters. Given that the GRAPHIC observable contains half of the code multipath errors, it is not surprising to see that the GRAPHIC antenna calibration is dominated by the code multipath for both GRACE and CYGNSS, but with half the magnitude (notice antenna calibration scale). For GRACE, this deviates to some degree at the lower elevations, where it is likely that deficiencies in the code-only ionosphere correction result in mean ionospheric errors being absorbed into the

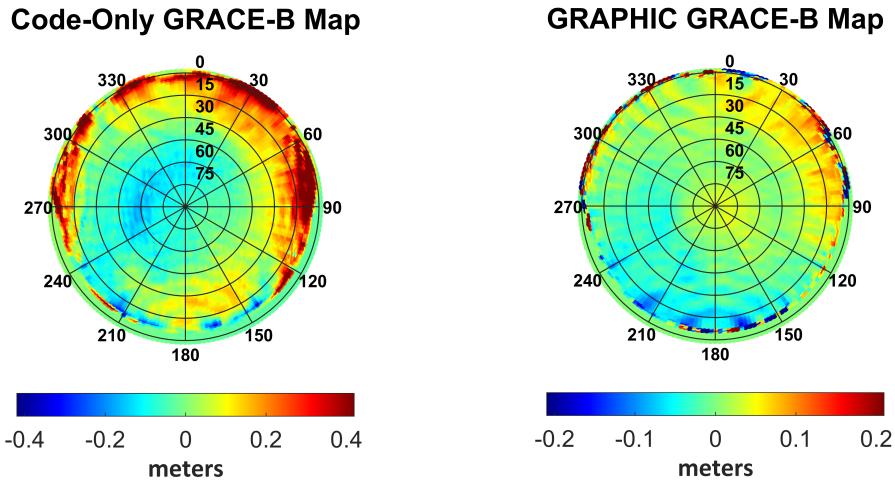


Figure 4.6: GRACE code-only (left) and GRAPHIC (right, half scale) antenna calibration

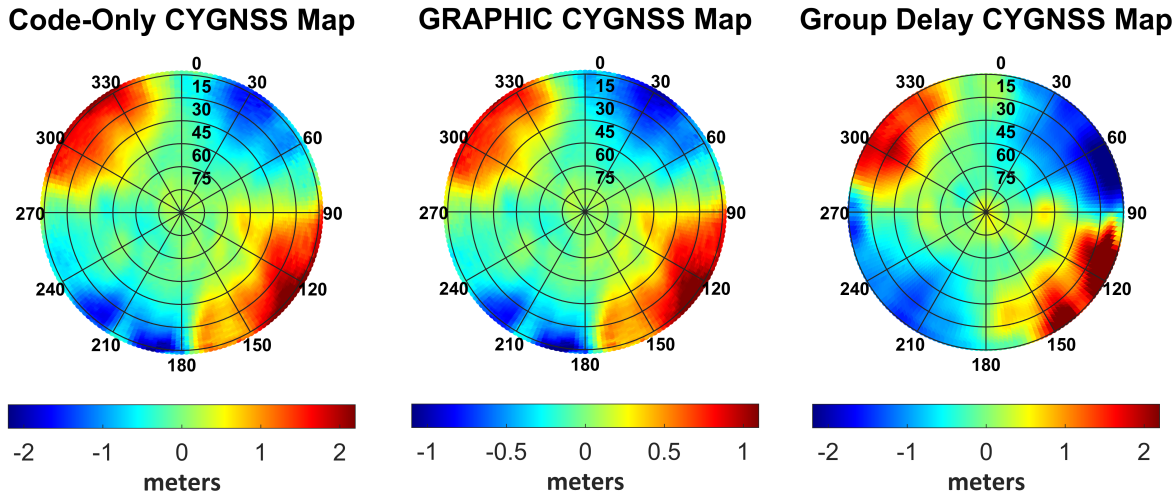


Figure 4.7: CYGNSS code-only (left) and GRAPHIC (middle, half scale) antenna calibration and anechoic chamber derived (right) group delay

antenna calibration. The effect is more pronounced for GRACE due to its lower orbit altitude (more ionosphere) and smaller multipath effects.

In Figure 4.7, for comparison, we also provide a group delay produced from anechoic chamber measurements using a CYGNSS zenith antenna mounted on an approximate CYGNSS satellite mockup (O'Brien, 2019; Wang et al., 2021). For this, the group delay is computed directly as the derivative of the measured right hand circular polarized (RHCP) phase with respect to frequency

at the L1 center frequency. We observe that the CYGNSS on-orbit and anechoic chamber antenna calibration are qualitatively very similar, which gives us confidence in the results produced by GipsyX. Since both the specific antenna and satellite differ from the CYGNSS FM05 on-orbit case, we should expect some differences in the two antenna calibrations. For POD, we will utilize the GipsyX antenna calibrations based on actual on-orbit data since these should be more accurate due to expected differences of in-flight hardware and configuration compared to the anechoic chamber mockup.

### 4.3.2 Orbit Quality Assessment

The internal metrics presented here provide a means to evaluate the overall consistency of the daily POD solutions. Two different metrics are shown here: the daily residual rms and the orbit overlap differences. The daily residual rms is a measure of the quality of fit of the daily reduced-dynamic POD strategy. Figure 4.8 shows the statistical distribution of the daily GRACE residual rms values for the time frame from January 2009 – July 2009. The daily GRAPHIC rms values are very consistent with a mean and standard deviation of 3.5 ± 0.04 cm. This would appear to be consistent with code noise of about 7 cm. However, the code-only residual rms values are significantly larger at 27.6 ± 3.2 cm. This discrepancy is likely due primarily to errors in the

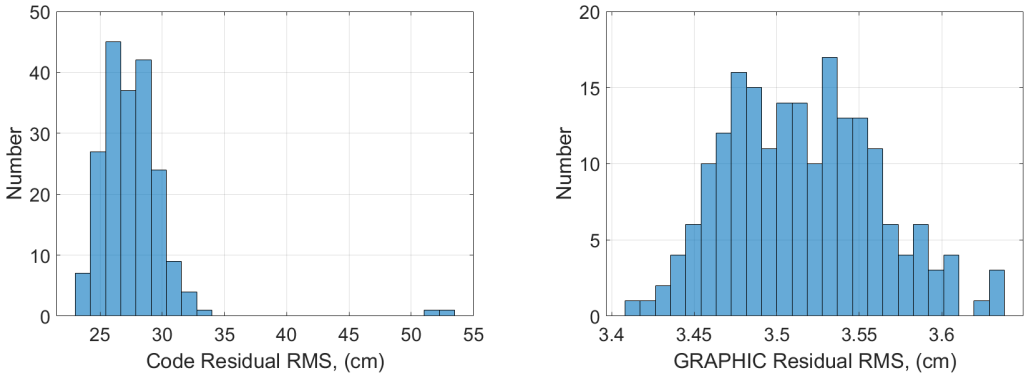


Figure 4.8: GRACE data fit residual rms statistics for code-only (left) and GRAPHIC (right) solutions (note scale)

ionosphere correction and residual DCBs. Here we see that GRAPHIC has a distinct advantage. It is both ionosphere-free and able to absorb the code DCBs in the carrier bias estimate.

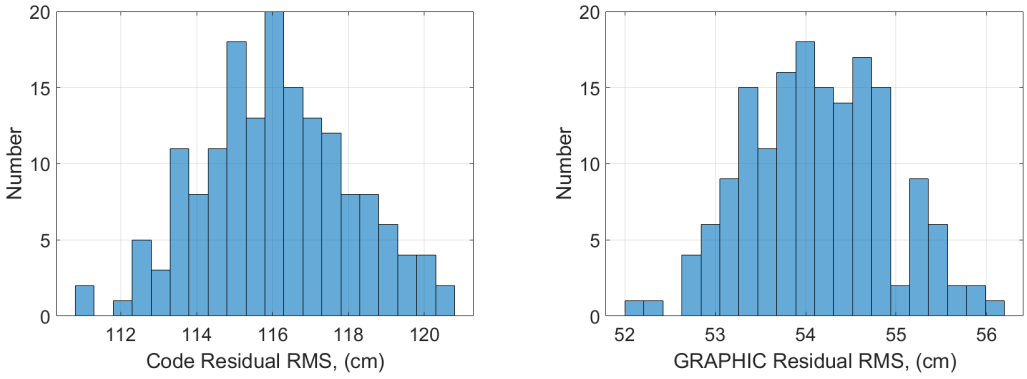


Figure 4.9: CYGNSS data fit residual rms statistics for code-only (left) and GRAPHIC (right) solutions (note scale)

Turning now to CYGNSS, Figure 4.9 shows the statistical distribution of the daily residual rms from July 2019 - December 2019. For CYGNSS, the daily GRAPHIC residual rms values are much larger than for GRACE but still consistent with a mean and standard deviation of 54 $\pm$ 0.8 cm. This would correspond to an expected code noise for CYGNSS of 108 cm which is close to the code-only mean and standard deviation of 116 $\pm$ 2.0 cm. When compared to GRACE, the CYGNSS GRAPHIC residuals are more than an order of magnitude larger representing a substantial increase in measurement noise. This is understood to be a combination of the quality of the receiver measurements and remaining multipath not adequately captured in the antenna calibration.

Orbit overlaps are a way to evaluate the precision or consistency of the POD solutions over time and are computed from the six hours of overlap that occur for 30-hour solution arcs centered at noon GPS time. Daily rms statistics are computed from the component differences of the central four hours of the six hours of overlap to avoid edge effects from the reduced dynamics. Figure 4.10 shows the distribution of the GRACE code-only and GRAPHIC statistics. Here we can see that the GRAPHIC POD solutions are much more consistent than the code-only method for all components. Table 4.7 shows the average and standard deviation of all the component statistics.

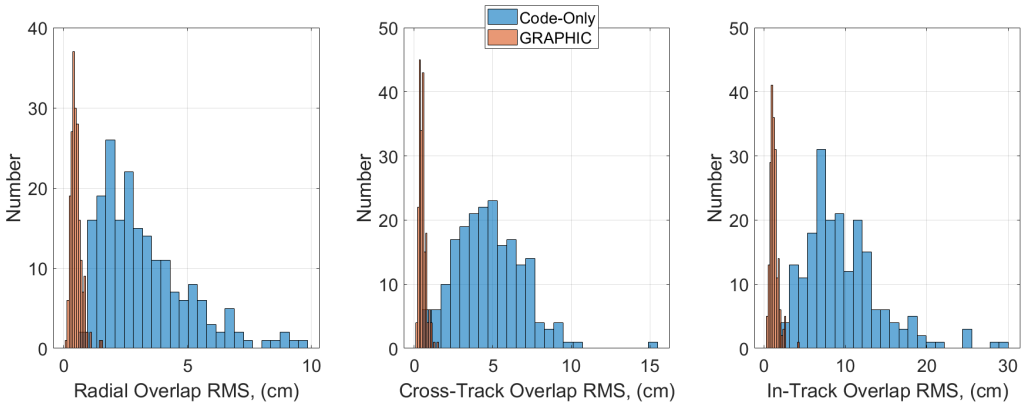


Figure 4.10: GRACE overlap rms statistics for radial (left), cross-track (middle), and in-track (right)

The mean and standard deviation of the GRAPHIC overlap rms statistics show very consistent results of 0.5 ± 0.2 cm for radial and cross-track and 1.2 ± 0.5 cm for the in-track. This is a significant improvement over the code-only method with a more than six-fold improvement in all three components.

We compute the same orbit overlap rms statistics for CYGNSS, shown in Figure 4.11 and Table 4.7. Like GRACE, the CYGNSS GRAPHIC POD solutions are more consistent than the code-only method for all components, but in this case show reductions by a factor of 1.5 for radial,

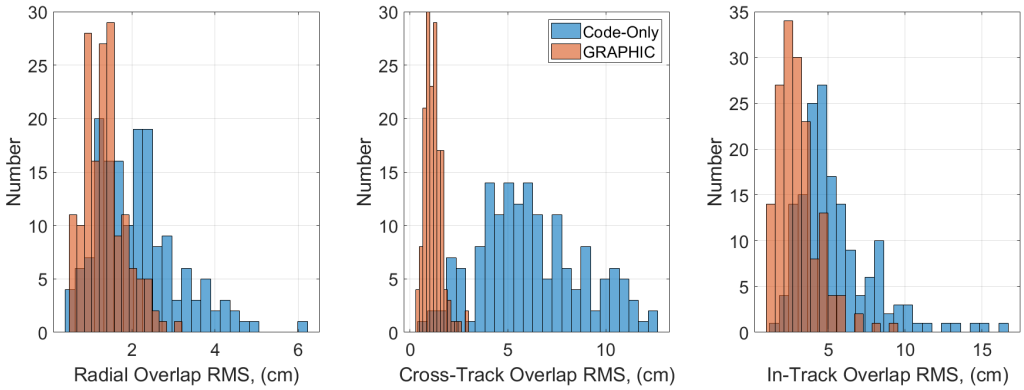


Figure 4.11: CYGNSS overlap rms statistics for radial (left), cross-track (middle), and in-track (right)

Table 4.7: GRACE and CYGNSS code-only and GRAPHIC mean ± standard deviation of the daily overlap rms statistics

| | **GRACE** | | **CYGNSS** | |
|---|---|---|---|---|
| | **Code-only** | **GRAPHIC** | **Code-only** | **GRAPHIC** |
| Component | mean rms ($cm$) | mean rms ($cm$) | mean rms ($cm$) | mean rms ($cm$) |
| Radial | 3.3 ± 1.8 | 0.5 ± 0.2 | 2.1 ± 1.0 | 1.4 ± 0.5 |
| Cross-Track | 4.8 ± 2.1 | 0.5 ± 0.2 | 6.2 ± 2.6 | 1.2 ± 0.4 |
| In-Track | 9.7 ± 4.8 | 1.2 ± 0.5 | 5.5 ± 2.5 | 3.0 ± 1.3 |

5 for cross-track, and 1.8 for in-track. The improvement is not as substantial for the CYGNSS GRAPHIC results as for GRACE, because of the higher noise level of the code measurements which do remain, reduced by a factor of 2, in the GRAPHIC observable. These results show a substantial improvement in orbit consistency with GRAPHIC but cannot confirm the improvement in accuracy. For that we turn to an external reference comparison using both GRACE and Sentinel-6 MF missions.

It is interesting to note that the CYGNSS code-only orbit overlaps are more precise than GRACE for the radial and in-track components. It seems possible that this result is related to the much larger than expected GRACE code-only residual rms when compared to the GRAPHIC residual rms. The remaining signals, DCBs and ionosphere, appear to be much larger than the noise. Because of the low noise of the GRACE pseudorange, it may be that these unmodeled signals have a much larger impact on the final orbit solution, degrading the code-only overlap precision.

### 4.3.3 GRACE Single-Frequency Errors

Because the orbit knowledge of the GRACE satellites is critical to its primary mission of mapping the gravity field, reduced-dynamic dual-frequency orbit solutions have been described by Bertiger et al. (2010b). These orbits have overlap precision of 1.4 mm radial, 2.2 mm cross-track, and 2.3 mm in-track as well as an accuracy of 2 mm for the distance between the satellites, as confirmed by comparison with independent K-band inter-satellite range measurements. These

validated orbits can be treated as "truth" orbits when compared to the single-frequency solutions. Here we first examine the biases associated with code-only and GRAPHIC POD solutions relative to the dual-frequency solution by computing component differences of the central 24 hours of the 30-hour arcs. The bias value is useful for evaluating the antenna calibration where it is possible to both introduce a bias or correct for one if it is known. The daily bias statistics for the radial, cross-track, and in-track components are shown in Figure 4.12. Both the code-only and GRAPHIC solutions show sub-cm bias statistics for the radial and cross-track components indicating very good performance here. The in-track bias is the largest for both the code-only and GRAPHIC solutions.

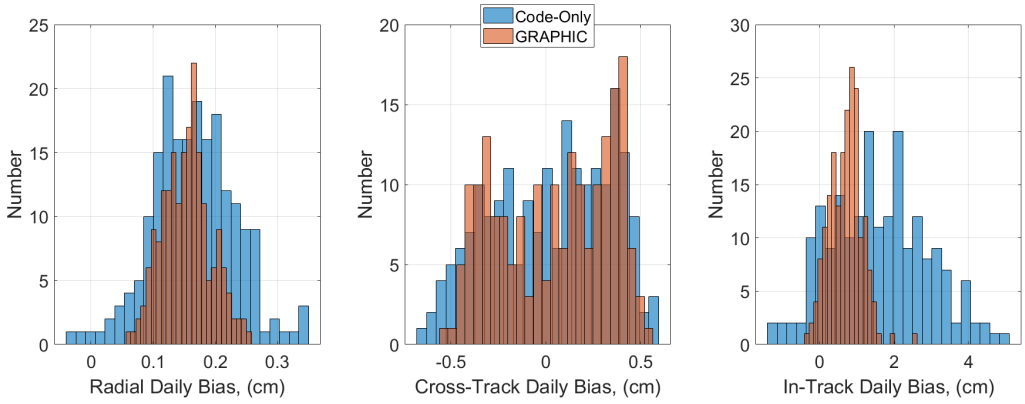


Figure 4.12: GRACE daily error bias statistics for radial, (left), cross-track (middle), and in-track (left)

The solution rms errors are computed from the same component differences. Figure 4.13 shows the daily rms statistics for the radial (left), cross-track (middle), and in-track (right). The GRAPHIC solution error rms is markedly smaller than the code-only solution by more than a factor of two for all components. Table 4.8 contains the overall mean and standard deviation of the daily statistics of the code-only and GRAPHIC errors. The GRAPHIC method performs significantly better than the code-only method with an average 3-D rms error of 3.1 $\pm$ 0.4 cm with an overall improvement by a factor of three when compared to the code-only solution errors at 9.3 $\pm$ 3.0 cm. Relating these errors back to the overlap statistics for each method, we can see that the average code-only overlap rms values are consistent with the overall error rms, but that for GRAPHIC, the

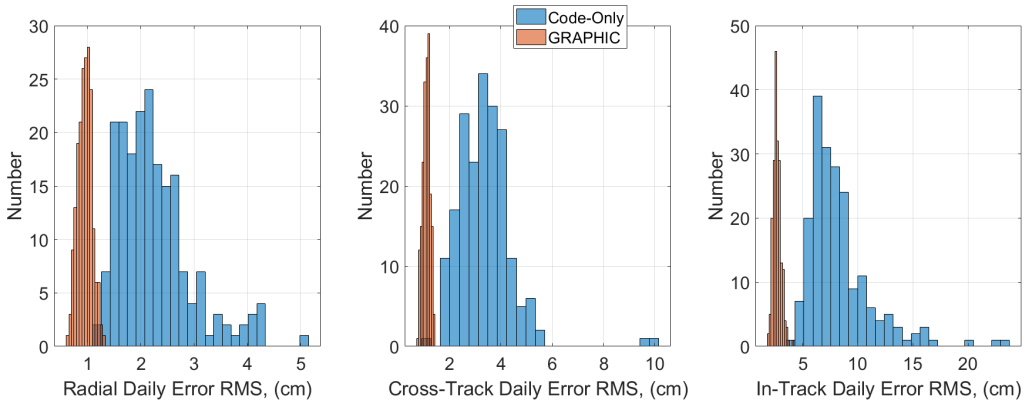


Figure 4.13: GRACE daily error rms statistics for radial, (left), cross-track (middle), and in-track (left)

overlap rms statistics are optimistic by about a factor of 2. Overall, the GRAPHIC method shows much better performance than the code-only method with a smaller in-track bias and reduced errors in all three components.

Table 4.8: GRACE code-only and GRAPHIC mean ± standard deviation of the daily bias error and rms error statistics

| | **Code-only** | | **GRAPHIC** | |
|---|---|---|---|---|
| Component | mean bias error ($cm$) | mean rms error ($cm$) | mean bias error ($cm$) | mean rms Error ($cm$) |
| Radial | 0.17 ± 0.07 | 2.1 ± 0.6 | 0.15 ± 0.04 | 0.9 ± 0.13 |
| Cross-Track | 0.03 ± 0.31 | 3.3 ± 1.0 | 0.04 ± 0.30 | 1.1 ± 0.14 |
| In-Track | 1.6 ± 1.3 | 8.0 ± 3.1 | 0.71 ± 0.43 | 2.5 ± 0.35 |

### 4.3.4 Code-Only and GRAPHIC Comparison

In the absence of dual-frequency measurements or other independent metrics to evaluate the CYGNSS single-frequency orbit accuracy, we leverage the GRACE results to understand the errors in the CYGNSS POD. We can conclude from the internal metrics that the GRAPHIC solution is more precise, and from the GRACE external orbit comparison that errors are smaller in all three components when compared to the code-only solution. While these conclusions are useful, they do

not provide a way to directly quantify the size of the CYGNSS GRAPHIC orbit errors except to say that the GRAPHIC overlap metrics are optimistic and place a lower bound on the errors.

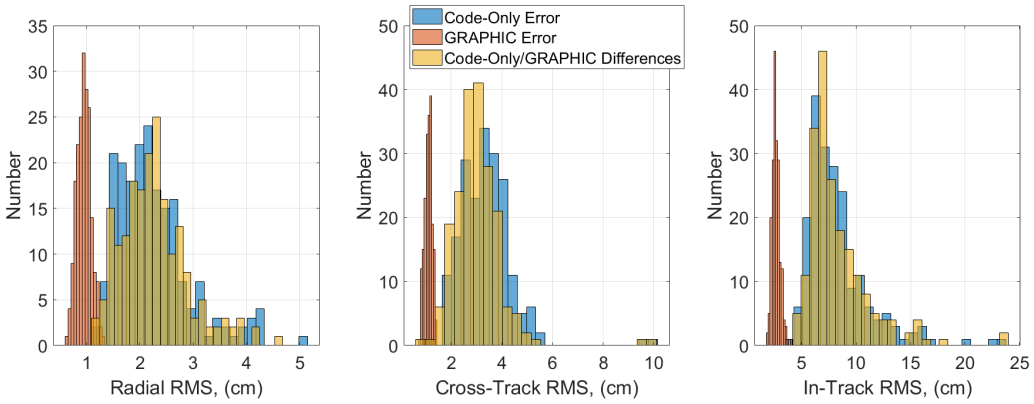


Figure 4.14: GRACE code-only and GRAPHIC errors compared to code-only/GRAPHIC radial (left), cross-track (middle), and in-track (right) component differences

An additional way to quantify the uncertainty in the GRAPHIC solution is to compare it directly to the code-only solution. Figure 4.14 shows a comparison of the statistics for the component differences in the GRACE code-only and GRAPHIC solutions along with the associated errors as inferred from comparison to the validated (dual-frequency) solutions. The solution differences are dominated by the code-only errors and can be used to place an upper bound on the GRAPHIC errors. For GRACE, the optimistic lower bound derived from GRAPHIC overlaps, combined with the pessimistic upper bound from the orbit solution differences between code-only and GRAPHIC solutions, produces a range of possible GRAPHIC orbit errors between 0.5 – 2.3 cm for radial, 0.5 – 3.0 cm for cross-track, and 1.2 – 8.4 cm for in-track. This is in good agreement with the actual GRACE GRAPHIC errors listed in Table 4.8.

The same comparison between the code-only and GRAPHIC solutions, but for CYGNSS, is shown in Figure 4.15. Here the component differences for CYGNSS are much larger than those seen for GRACE. It is also notable that the component with the largest mean rms is the cross-track resulting in a more than 30 cm difference. A summary of the mean and standard deviation of the daily bias and rms statistics is shown in Table 4.9. Once again, we can use the GRAPHIC overlap

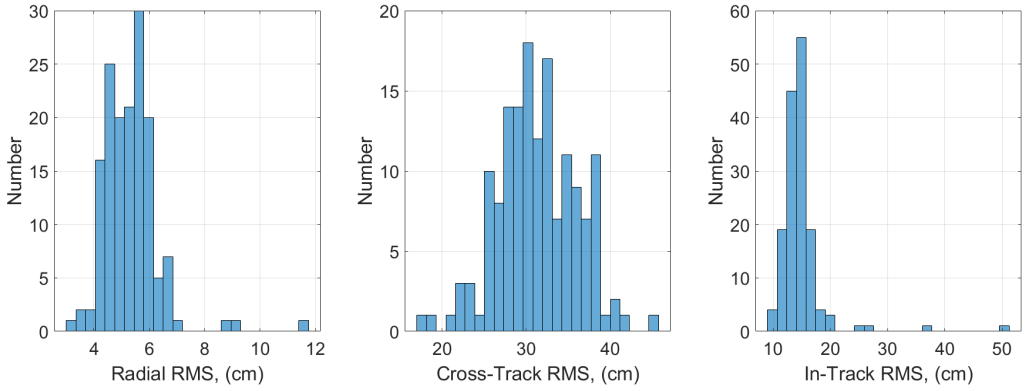


Figure 4.15: CYGNSS code-only/GRAPHIC difference rms statistics for radial (left), cross-track, (middle), and in-track (right)

statistics from Table 4.7 to approximate the CYGNSS GRAPHIC solution lower error bound and the code-only and GRAPHIC solution differences from Table 4.9 for the upper error bound. This produces a potential error range for the CYGNSS GRAPHIC orbits of 1.4 – 5.3 cm for radial, 1.2 – 31 cm for cross-track, and 3.0 – 15 cm for in-track.

Table 4.9: Code-only and GRAPHIC comparison for GRACE and CYGNSS in terms of the mean ± standard deviation of the daily solution differences

| | **GRACE Code-only/GRAPHIC** | | **CYGNSS Code-only/GRAPHIC** | |
|---|---|---|---|---|
| Component | mean bias ($cm$) | mean rms ($cm$) | mean bias ($cm$) | mean rms ($cm$) |
| Radial | 0.01 ± 0.06 | 2.3 ± 0.6 | 0.00 ± 0.62 | 5.3 ± 1.0 |
| Cross-Track | 0.02 ± 0.07 | 3.0 ± 1.0 | 0.06 ± 0.88 | 31 ± 4.7 |
| In-Track | 0.89 ± 1.4 | 8.4 ± 2.9 | 1.8 ± 2.7 | 15 ± 4.1 |

It is interesting to observe that the cross-track differences between the CYGNSS GRAPHIC and code-only solutions are consistent with a very small inclination change. The cross-track difference has a frequency of once-per-orbit with a relatively constant amplitude, and the largest difference occurs at the highest/lowest latitude of the CYGNSS orbit. These differences persist in dynamic only orbit solutions with and without any cross-track empirical accelerations. This implies a persistent signal difference between the pseudorange and GRAPHIC observable which would indicate either an ionosphere related signal, or some behavior related to the GPS transmitter DCBs,

transmitter antenna calibrations, or clock solutions. To test the hypothesis that the code-only solution is the one that contains the error, a single day of Sentinel-6 MF is examined. It is in a roughly circular orbit at an altitude of 1336 kilometers with an inclination of 66 degrees. Figure 4.16 shows a time history comparison of the CYGNSS cross-track GRAPHIC and code-only differences (left) and Sentinel-6 MF cross-track differences for a GRAPHIC and code-only solution relative to the dual-frequency solution. Here we see a similar pattern in the Sentinel-6 MF code-only cross-track differences with a once-per-orbit variability indicating that large differences observed for CYGNSS are a result of errors in the code-only solutions.

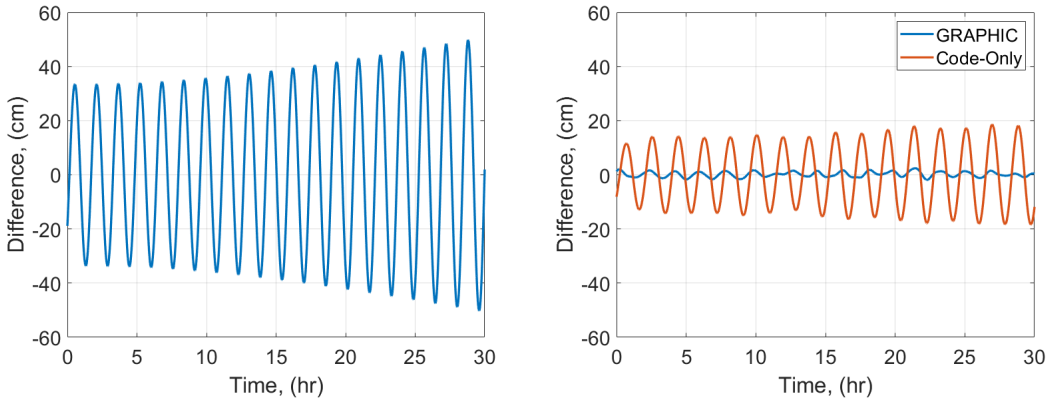


Figure 4.16: Cross-track difference time history for CYGNSS GRAPHIC/code-only, DOY 191, 2019 (left), and Sentinel-6 MF GRAPHIC and code-only comparison to dual-frequency solution (right), DOY 100, 2021

The results in Figure 4.16 are consistent with the conclusion that the code-only solution cross-track errors are much larger than the GRAPHIC cross-track errors. Here the CYGNSS GRAPHIC/code-only difference has an rms of 28 cm compared to the Sentinel-6 MF code-only error rms of 11 cm. This is in contrast to the Sentinel-6 MF GRAPHIC error rms which is an order of magnitude smaller at 1 cm. This observation shows that the cross-track signal in the code-only solution is not present in the GRAPHIC solution. If it were, we would expect to see a cross-track error in the GRAPHIC solution with half the amplitude, but this is not the case. From this, we conclude that the CYGNSS GRAPHIC/code-only differences, like GRACE, are dominated by the code-only errors. Further investigation of the fundamental causes for this behavior would

need to be done to fully explain the observed cross-track differences of the code-only solutions. Such an investigation is beyond the scope of this thesis, but this suggests potentially large errors (>25 cm ) in a code-only solution can exist that would be hidden when assessing the orbits through overlaps alone. Without any method of independent evaluation of the CYGNSS GRAPHIC orbits, we rely on the lessons learned from GRACE and Sentinel-6 MF. Applying the fact that the GRACE GRAPHIC overlaps were optimistic by a factor of two places the CYGNSS orbit errors at 2.8 cm radial, 2.4 cm cross-track, and 6 cm in-track. Overall, the GRAPHIC method is far more precise and accurate than the code-only solution and is the preferred single-frequency method for producing orbit solutions. This is due in part to the lower noise in the GRAPHIC observable and removal of the ionospheric signal.

## 4.4 Summary

Effective strategies for POD with single-frequency CYGNSS data in GipsyX have been introduced and demonstrated on more than 5 months of data from CYGNSS FM05 satellite in the context of assessing its applicability for altimetry. Parallel analysis of data from the GRACE mission provides a basis for quantifying the accuracy of the CYGNSS solutions. With GRACE, the GRAPHIC method, when compared to the code-only method, is shown to be both more accurate and precise. A bound on the $1\sigma$ CYGNSS GRAPHIC orbit errors can be determined from the GRAPHIC overlap statistics and the differences between the two solutions. This approach places a potential $1\sigma$ range of 1.4 – 5.3 cm for radial, 1.2 – 31 cm for cross-track, and 3.0 – 15 cm for in-track with a 3-D position error of 3.5 – 40 cm. Because the solution differences are dominated by the code-only errors as shown in the Sentinel-6 MF example, GRAPHIC solutions will be closer to the lower bound, particularly for the cross-track component. Based on analysis of GRACE POD solutions using the same methodology, and in particular the GRAPHIC overlap statistics, we estimate that the $1\sigma$ CYGNSS GRAPHIC orbit accuracy is 2.8 cm radial, 2.4 cm cross-track, and 6 cm in-track placing the 3-D accuracy less than 10 cm. With this method and the assessment

of the improved orbit accuracy in place, researchers will be able to better determine the potential utility of the CYGNSS constellation for GNSS-R based altimetry.

# Chapter 5

# Sentinel-6 MF Background and Precise Orbit Determination Models

## 5.1 Sentinel-6 MF Background

Satellite altimetry plays a critical role in both climate science and oceanography (Le Traon et al., 2019). The Sentinel-6 Michael Freilich (MF) spacecraft, launched in November 2020, is the latest in a 30-year series of space-based reference ocean altimeters. Primarily designed to measure global ocean sea surface height and provide continuity of service, it builds on the success of previous ocean-monitoring missions beginning with TOPEX/Poseidon in 1992 and followed by the Jason-1/2/3 series of spacecraft. Together, these missions provided valuable insights into ocean currents, sea level rise, and other oceanographic phenomena (Donlon et al., 2021a). Each of these satellites has occupied approximately the same reference orbit with an inclination of 66.04 deg, an altitude of 1339-1356 km, and an orbital period of 112 minutes, resulting in a repeat ground track of 9.9 days. The reference orbit was designed to avoid aliasing of the dominant tidal frequencies into the altimetry data (Parke et al., 1987).

Like its predecessors, Sentinel-6 MF underwent a calibration phase where it flew in tandem with the previous mission, Jason-3. This provides a continuous altimetry record beginning with TOPEX in 1992 to the present day with Sentinel-6 MF, against which other altimetry missions such as CryoSat-2 (Wingham et al., 2006) and Sentinel-3 (Donlon et al., 2012) are calibrated. The Sentinel-6 MF payload includes the Poseidon-4 Ku/C-band synthetic aperture radar altimeter that provides highly accurate and precise altimetry measurements and a multi-frequency Advanced

Microwave Radiometer for Climate (AMR-C) to correct for delay caused by atmospheric water vapor (Donlon et al., 2021a).

Unlike the previous TOPEX/Jason series of spacecraft, which are box shaped with extended solar panels that rotate to maintain sun pointing, Sentinel-6 MF is roughly house-shaped with fixed solar panels, mounted roof-like, that extend beyond the spacecraft body. The spacecraft layout and primary instrumentation locations are shown in Figures 5.1 and 5.2. This configuration eliminates the need for yaw-steering to keep the solar panels pointed towards the sun as was done with the Jason series of spacecraft. However, it does present additional challenges in the solar radiation pressure modeling as it creates significant shadowing effects. Addressing this challenge is the topic of Chapter 6.

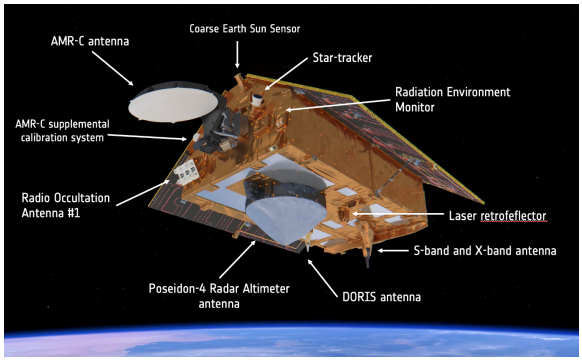


Figure 5.1: Sentinel-6 MF instruments including laser retroreflector location. Image credit from (Copernicus.eu, 2023a)

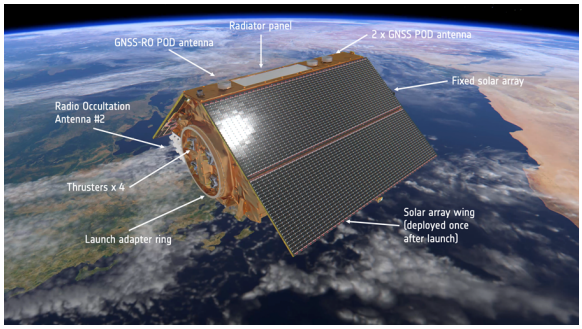


Figure 5.2: Sentinel-6 MF instruments including GNSS antenna locations. Image credit from (Copernicus.eu, 2023b)

The following two sections, 5.2 and 5.3, describe the applied background models and provide an overview of the POD estimation strategies for Sentinel-6 MF and Jason-3. The background models are identical for all orbit solutions unless otherwise specified. All reduced-dynamic ambiguity-resolved orbit solutions, which are evaluated using SLR residual analysis, apply the orbit solution strategy described here. Next, section 5.4 gives an overview of the Sentinel-6 nominal attitude and is followed by Section 5.5 which describes the *a priori* antenna calibrations and applied constraints. Finally, section 5.6 lists the corrections that have been applied to the SLR observations for independent evaluation of the orbit solutions.

## 5.2 Orbit Background Models

We use JPL's GipsyX/RTGx software (Bertiger et al., 2020) for all precise orbit determination solutions with the models listed in Table 5.1. We use either a 12-panel macromodel or SRP table (Conrad et al., 2022) along with measured spacecraft attitude to compute the drag and solar radiation forces. A new approach to modeling of the SRP forces is described in more detail in Chapter 6 and the macromodel surface properties are listed in Table 6.3. The drag model incorporates the DTM-2000 empirical thermosphere model (Bruinsma et al., 2003) to estimate the atmospheric density from the F10.7 cm solar flux and Kp geomagnetic indices. Radiation pressure forces for both Earth albedo (Knocke et al., 1988) and visible solar (Milani et al., 1987) are applied. The geopotential is computed using the GRACE time-variable CNES/GRGS RL04 Earth gravity models up to degree and order 200 (Lemoine et al., 2019). Additional gravitational effects such as solid Earth tides and pole tides conform to the version 1.3.0 IERS conventions (Petit and Luzum, 2010). Ocean tides use a GOT4.8a model (Ray, 2013) which is modified to account for geocenter motion (Desai and Ray, 2014) and implemented using the convolution formalism of Desai and Yuan (2006). Third-body gravitational effects are included using the JPL DE421 planetary and lunar ephemeris (Folkner et al., 2009).

GPS satellite ephemerides, clock solutions, wide-lane phase bias information, and Earth orientation parameters all come from the JPL IGS Analysis Center Final products (Dietrich et al.,

Table 5.1: Measurement and POD models applied in GipsyX/RTGx

| **Model/Parameter** | **Sentinel-6 MF Selection** |
|---|---|
| GNSS observations | Undifferenced GPS L1/L2 phase and pseudorange, 5-min observations, 30-hour daily arcs* |
| Surface forces | Estimated Macromodel (Table 6.3) |
| Sentinel-6 mass | 1180.633 kg (Jan 1, 2021) |
| Sentinel-6 Attitude | Measurement quaternions |
| Sentinel-6 TriG Antenna Reference Point | [-0.933048, 0.006592, -1.13205] m, (Jan 1, 2021) |
| Sentinel-6 PODRIX Antenna Reference Point | [0.930109, -0.00196, -1.097241] m, (Jan 1, 2021) |
| Sentinel-6 LRA Reference Point | [0.091813, -0.393605, 0.604395] m, (Jan 1, 2021) |
| Atmospheric density | DTM-2000 (Bruinsma et al., 2003) |
| GPS satellite antenna calibrations | IGS14 Values (igs14_2194.atx) (Rebischung and Schmid, 2016) |
| Earth orientation/rotation | JPL IGS Analysis Center IGS14 Final Solutions |
| GPS spacecraft ephemerides | JPL IGS Analysis Center IGS14 Final Solutions |
| GPS spacecraft clocks and wide-lane phase bias information | JPL IGS Analysis Center IGS14 Final Solutions (Dietrich et al., 2018) |
| Planetary and lunar ephemerides | JPL DE421 ephemerides (Folkner et al., 2009) |
| Earth gravity field | EIGEN-GRGS.RL04.MEAN-FIELD (Lemoine et al., 2019) |
| Ocean tides | GOT4.8 tide model (Ray, 2013) |
| Reference frame | IGS14 |

*Antenna calibration estimation uses 24-hour arcs

2018). Based on the IGS standards (Johnston et al., 2017), the GPS clock solutions are referenced to the L1/L2 P(Y)-code dual-frequency ionosphere-free combination. Orbit solutions and background models are applied in the IGS14 reference frame which is the IGS realization of the ITRF14 (Altamimi et al., 2016).

## 5.3 Orbit Solution Strategy

For the following chapters, our most rigorous solutions adopt a reduced-dynamic POD approach with single receiver ambiguity resolution (Bertiger et al., 2010b). The POD solution is an iterative process. Following the process described in Section 2.2.1, a reference trajectory is first constructed from a dynamic fit to the on-board navigation solution. Next, three dynamic passes

are processed estimating a drag coefficient and constant amplitude once-per-orbit empirical accelerations in the cross-track and in-track directions. Each subsequent pass adopts the previously estimated dynamic parameters as the *a priori* values. A reduced-dynamic pass follows the dynamic passes, with constant empirical accelerations estimated stochastically in the radial and in-track directions, as well as stochastic once-per-orbit accelerations in the cross-track and in-track directions. The once-per-orbit accelerations apply nominal values as estimated in final dynamic pass. The parameterizations are summarized in Table 5.2 including the stochastic update intervals and correlation times. These reduced-dynamic and ambiguity-resolved solutions are the basis for the final accuracy assessment using independent SLR observations. Implementations of the empiri-

Table 5.2: POD estimation strategy within GipsyX/RTGx

| Estimated Parameters | Parameterization | *a priori* $\sigma$ |
|---|---|---|
| **Epoch State** | | |
| 3-D epoch position (X,Y,Z) | Bias per arc | 10 $km$ |
| 3-D epoch velocity (X,Y,Z) | Bias per arc | 1 $km/s$ |
| **Empirical Acceleration (3 dynamic passes)** | | |
| Drag Coefficient | Bias per arc | 1000 |
| Once-per-orbit cross-track (cos, sin) | Bias per arc | 1 $mm/s^2$ |
| Once-per-orbit in-track (cos, sin) | Bias per arc | 1 $mm/s^2$ |
| **Empirical Acceleration (reduced-dynamic)** | | |
| Radial | Stochastic with $\tau$ = 6 hrs $\Delta$t = 30 min | 1 $nm/s^2$ |
| In-track | Stochastic with $\tau$ = 6 hrs $\Delta$t = 30 min | 1 $nm/s^2$ |
| Once-per-orbit cross-track (cos, sin) | Stochastic with $\tau$ = 6 hrs $\Delta$t = orbit period | 2 $nm/s^2$ |
| Once-per-orbit in-track (cos, sin) | Stochastic with $\tau$ = 6 hrs $\Delta$t = orbit period | 2 $nm/s^2$ |
| **Carrier Phase Bias** | Constant bias per continuous carrier track | 1e6 $km$ |
| **Clock Offset** | White-noise Process | 3e5 $km$ |

$\Delta$t is the update interval and $\tau$ is the correlation time

cal accelerations and stochastic reduced-dynamics within the filter are described in more detail in Section 2.2.2.

## 5.4 Sentinel-6 MF Attitude

Knowledge of the spacecraft attitude is important for several aspects of the POD process. The attitude plus macromodel allows for accurate modeling of both the solar radiation pressure forces and the drag forces. Also, because the POD process estimates the location of the spacecraft center of mass, the attitude is required to correctly model the offset of the receiving antenna relative from this reference point.

The Sentinel-6 MF attitude is constructed from quaternions measured on-board the spacecraft. The nominal attitude profile is close to yaw-fixed. For Sentinel-6 MF, this results in the spacecraft body-x axis being closely aligned with the in-track direction, body-y axis in the cross-track direction (orbit normal), and body-z axis aligned with the radial direction. Over the course of an orbit, the measured yaw about the spacecraft z-axis varies only ± 4 degrees while the pitch and roll stay near zero relative to the orbit frame. During several periods of low beta angle, Sentinel-6

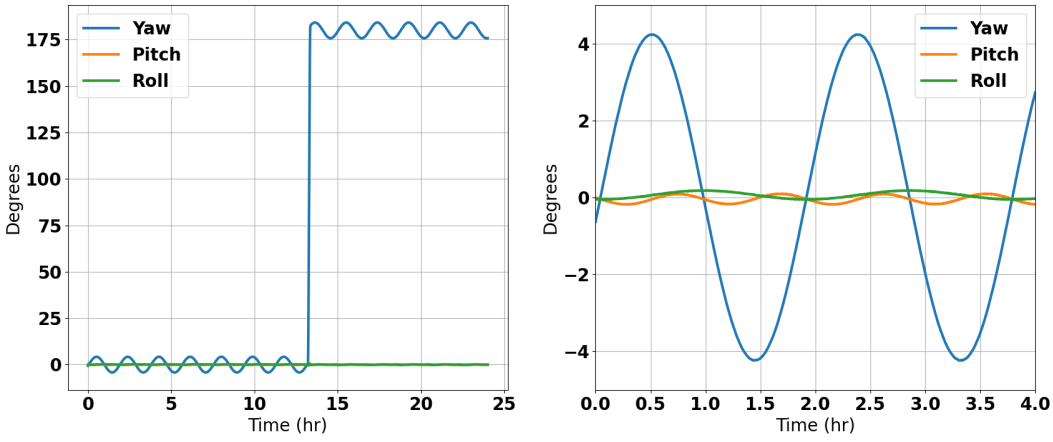


Figure 5.3: Attitude profile change during a yaw-flip (left) on 2021-07-01 and close up view of the yaw, pitch, and roll (right) during nominal attitude flight

MF was commanded to perform a yaw-flip maneuver (180-deg yaw bias for $\sim$ 4 days) to support POD activities related to resolving the estimated antenna calibration y-offsets (ESA, 2023). Figure 5.3 shows the transition from fly-forward to fly-backward on 2021-07-01 in terms the Euler yaw, pitch, and roll angles of the body-frame with respect to the orbit frame. For each yaw-flip, this attitude is maintained for approximately four days before resuming the nominal fly-forward attitude.

## 5.5 Sentinel-6 MF *a priori* Calibrations and Constraints

To initialize the in-flight antenna calibration procedures described in Chapter 3, we begin with the pre-launch antenna calibrations for each Sentinel-6 MF antenna as shown in Figure 5.4. While there are only two physical antennas (not counting the redundant PODRIX antenna), three separate pre-launch calibrations were performed: TriG-GPS, PODRIX-GPS, and PODRIX-Galileo. The antennas for both receivers are nearly identical and so the pre-launch calibrations are very similar. Each contains a large z-offset, so for comparative purposes, Figure 5.5 shows the same pre-launch antenna calibrations but with the z-offset removed. The PODRIX-Galileo pre-launch calibration, which uses the same antenna as the PODRIX-GPS, shows slightly smaller PVs than both GPS calibrations likely due to the use of the E5 signal.

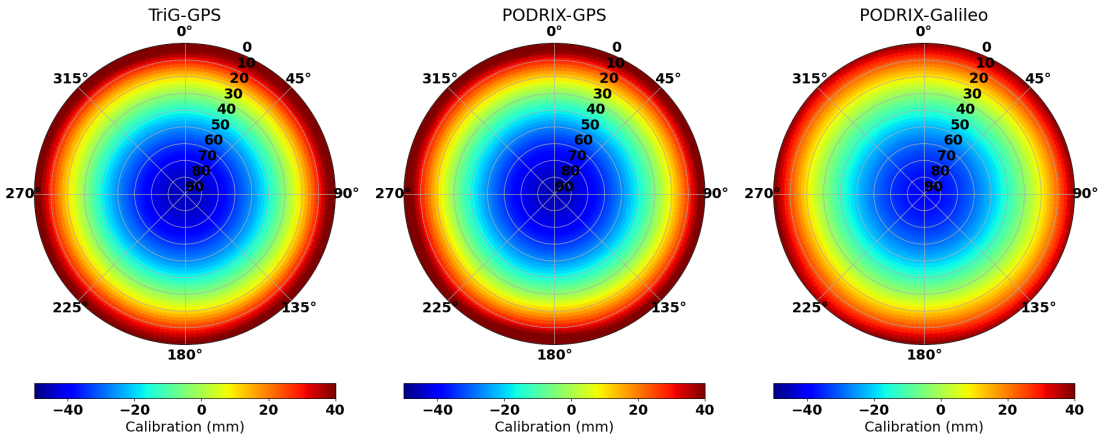


Figure 5.4: Pre-launch antenna calibrations used for *a priori* calibration

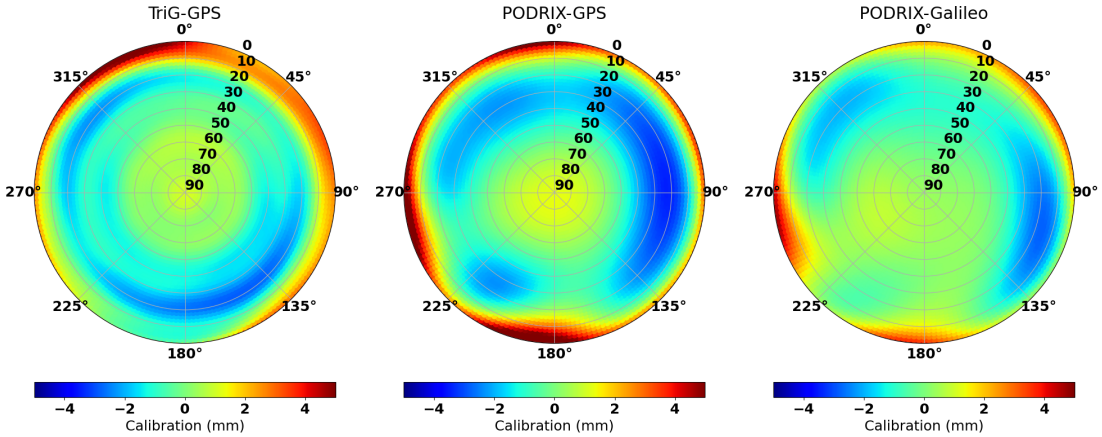


Figure 5.5: Pre-launch antenna calibrations with z-offset removed

The antenna calibration values are described using azimuth measured clockwise from 0 to 360 degrees and elevation from 0 to 90 degrees in the antenna frame which is closely aligned with the spacecraft body-x/y/z frame. The 0 degree azimuth direction corresponds to the positive antenna-x direction (body +x), 90 degrees azimuth to the negative antenna-y direction (body +y), and 90 degrees elevation to the positive antenna-z direction (body -z).

For each of the following studies, the Sentinel-6 MF in-flight antenna calibration is estimated as part of the dynamic orbit solutions with the filter state augmented by the antenna calibration vertices. As described in Chapter 3, the antenna calibration is formulated in terms of the mean PCO (body-x/y/x offsets with respect to the mechanical antenna reference point) and a set of line-of-sight azimuth and elevation dependent phase variations. As presented previously in Equations 3.1 and 3.2, there are inherent degrees of freedom for the PCO offset vector $\mathbf{r}_0$ and the PV function $\phi(az, el)$ which allows for the transformation into a new set of PCOs and PVs through a PCO shift, $\Delta\mathbf{r}$, and constant phase bias offset $\Delta\phi$ (or clock offset for code). Because of this, we first choose to constrain $\Delta\phi$ in Equation 3.2 by leveling the entire antenna calibration correction of all bins above 30 degrees elevation to zero.

Given the attitude of Sentinel-6 MF described in the previous section, it is difficult to resolve a mean PCO from the phase variations relative to the antenna reference point for the in-track (aligned

with body-x direction) direction. This same issue has previously been observed in estimation of the horizontal PCOs for GNSS satellites during periods when the spacecraft attitude aligns the body x- or y-axis with the in-track direction (Schmid et al., 2007; Huang et al., 2022). When estimating antenna offsets, this essentially decouples the antenna location from the center of mass under the constraint that the offset is fixed across the entire solution arc. It is possible for the center of mass to be offset in the in-track direction without creating any inconsistency with the observations or dynamical models. Because the Sentinel-6 MF antenna offset in the body-x direction is aligned with the in-track direction, it is similarly difficult to observe. For this reason, we also choose to constrain the PCO of the antenna calibration correction in the body-x direction to zero by applying the constraint given in Equation 3.12. This is equivalent to setting $\Delta\mathbf{r} = [\Delta x = 0, \Delta y, \Delta z]$. Here we allow the receiver antenna calibration to absorb offsets in the body-y and z components relative to the *a priori* values, but not for the body-x offset.

## 5.6 Laser Retroreflector Array

Satellite laser ranging is an optical technique that measures the round-trip time of flight of a laser pulse from a ground station to a target satellite. As given by Pearlman et al. (2019), the measured round-trip time of flight is given by

$$\begin{aligned}\Delta\tau_R^S = \frac{1}{c}\{|\vec{r}(t+\Delta t_1) - \vec{R}(t)| + |\vec{R}(t+\Delta t_1+\Delta t_2) - \vec{r}(t+\Delta t_1)|\} \\ +\delta_{Trop} + \delta_{Rel} + \frac{1}{c}\delta_{Sys} + \varepsilon_\tau + \frac{1}{c}\eta_R\end{aligned} \tag{5.1}$$

where $t$ is the time of the emission of the pulse from the SLR station, $c$ is the speed of light in a vacuum, $\Delta t_1$ is the flight time from the station to the satellite, $\Delta t_2$ is the time of flight from the satellite back to the station, $\vec{r}(t)$ is the position of the satellite, $\vec{R}(t)$ is the station position, $\delta_{Trop}$ is the delay due to troposphere refraction, $\delta_{Rel}$ is the delay due to relativistic effect, $\delta_{Sys}$ is the delay associated with the ground station, $\varepsilon_\tau$ is the error in the time-tag, and $\eta_R$ includes residual range errors in the system. The time-of-flight for each path, $\Delta t_1$ and $\Delta t_2$, is estimated using an

iterative approach after applying each of the corrections and accounting for the offset of the laser retroreflector array (LRA) from the spacecraft center of mass.

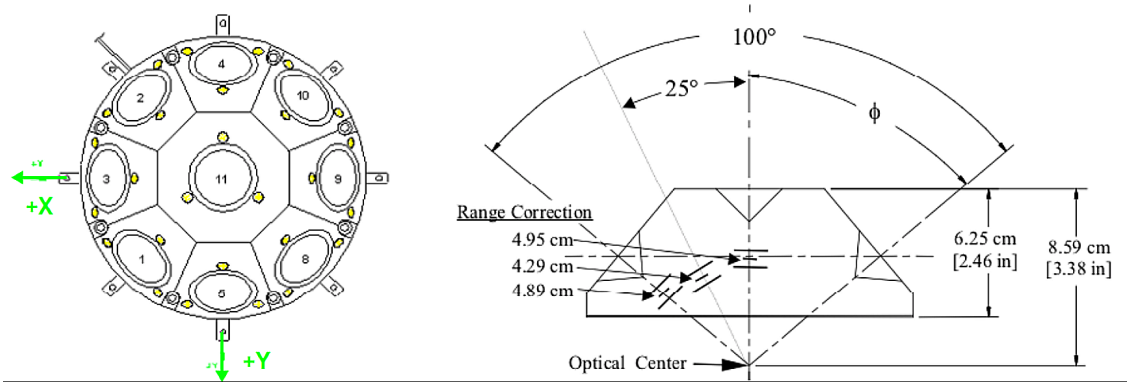


Figure 5.6: Sentinel-6 MF Laser retroreflector array diagram. Image credit: (Couderc, 2015)

The LRA on Sentinel-6 MF is constructed with nine corner cubes, as seen in the left panel of Figure 5.6, where the +z axis points in the spacecraft nadir direction. A center cube is oriented in the nadir direction, surrounded by eight equally spaced corner cubes, each tilted 50 degrees away from the LRA +z direction. Several corrections must be applied to accurately model the timing and reflection of the SLR pulses. First, a correction to the optical center of -23.375 mm (ESA, 2023)

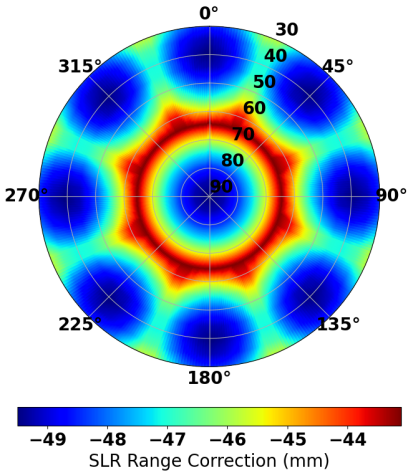


Figure 5.7: Sentinel-6 MF range corrections based on line-of-sight azimuth and elevation in the LRA frame (Mercier and Couhert, 2016)

is applied to the LRA mounting location given in Table 5.1. Additional range corrections based on the line-of-sight azimuth and elevation in the LRA frame are applied (Mercier and Couhert, 2016). Figure 5.7 shows the range corrections applied to the SLR observations as a function of azimuth and elevation. While the SLR measurements can be used directly in orbit estimation or withheld for orbit validation, the studies presented in this thesis exclusively use the SLR observations and corresponding residuals for orbit validation.

## 5.7 Summary

The previous sections provide a description of the background models, reduced-dynamic solution strategies, nominal attitude, and pre-launch antenna calibrations and applied constraints for Sentinel-6 MF. The background models are consistent for each the following studies unless otherwise stated (e.g. applied SRP model). The attitude profile is discussed here as it impacts various aspects of the Sentinel-6 MF studies. In particular, the yaw-fixed attitude factors into the applied antenna calibration constraints for each solution.

# Chapter 6

# Improved Modeling of the Solar Radiation Pressure for the Sentinel-6 MF Spacecraft

## 6.1 Introduction

As discussed previously in Chapter 2, GNSS-derived POD accuracy has increased due to improved state of the art gravity models, satellite surface macromodels, antenna calibrations, reduced dynamic processing (Wu et al., 1991), improved accuracy in the orbit position and clock bias estimates of the GNSS satellites, and phase ambiguity resolution (Bertiger et al., 2010b). Of these, the antenna calibration and the macromodel are specific to the satellite platform. The antenna calibration corrects for line-of-sight variations due to both antenna phase patterns and multipath, and the macromodel provides surface properties used in modeling spacecraft solar radiation pressure (SRP) and drag forces.

During our initial POD processing for Sentinel-6 MF, we observed large shifts in the drag coefficient immediately after 180 degree yaw-flip maneuvers described in section 5.4. Additionally, attempts to estimate the antenna y-offsets relative to the nominal antenna reference point resulted in a much larger than expected variation of roughly 3 cm, that was highly correlated with the sun beta angle (sun elevation relative to the orbit plane). Given that Sentinel-6 MF orbits at an altitude over 1300 km, where drag force is very small, both of these observations are indicators of potential errors in the macromodel or the manner in which it is implemented. Thus, this study was undertaken in an effort to improve the Sentinel-6 MF SRP modeling and subsequent POD.

At the Sentinel-6 MF orbit altitude, SRP forces are the dominant perturbation after higher

order gravity effects. Colombo (1989) found that the dominant SRP perturbations on the GPS satellite orbits are a constant and once-per-orbit acceleration. Because many errors occur at these frequencies, POD solutions for LEO satellites often employ reduced-dynamic solutions that estimate constant and once-per-orbit empirical accelerations (Haines et al., 2004; Bertiger et al., 2010a). However, estimation of constant empirical accelerations simultaneously with the antenna calibration can cause a shift in the apparent PCO (Jäggi et al., 2009), so antenna calibrations are best constructed using highly constrained dynamic orbit estimates without constant empirical acceleration terms. Likewise, SRP modeling errors in the constant terms can also induce an offset in the estimated antenna PCOs. For this reason, accurate SRP modeling is an important factor for in-flight estimation of antenna calibrations.

SRP forces are modeled either analytically or empirically (Duan and Hugentobler, 2021). A cannonball is the simplest analytical SRP model that treats the satellite as sphere with constant cross-sectional area impacted by solar radiation. For POD it is more common to use a "box-wing" model which was first shown by Marshall and Luthcke (1994) to be necessary to meet the orbit error budget for TOPEX/Poseidon. The box-wing and other macromodels (Rodriguez-Solano et al., 2012; Montenbruck et al., 2015b) describe a spacecraft using a simplified set of plates with surfaces defined using a normal vector, surface area, and reflective properties. SRP forces from the macromodel are computed as a summation of the individual effects from each plate as given by Milani et al. (1987).

Empirical SRP force models are derived from estimated orbit accelerations. These models, such as JPL's GPS solar radiation pressure model (GSPM) (Bar-Sever and Kuang, 2003), define forces based on the sun position in a body-fixed frame. For the GSPM specific to each block of GPS satellites, the SRP forces are expressed in terms of a truncated Fourier expansion in the GPS satellite body-fixed frame. Another empirical method is a composite table, where the body-x/y/z SRP force acting on the spacecraft is determined as a function of the sun's azimuth and elevation in the spacecraft body frame (Bertiger et al., 2020). The disadvantage of an SRP table is that

it cannot easily account for changes in the spacecraft geometry such as the relative position of movable solar panels.

The Jason series of spacecraft, which preceded Sentinel-6 MF, have a rectangular body with two solar panel wings. The macromodels work well for this type of spacecraft design because the solar panels are never in shadow and they dominate the overall SRP forces. The solar panels are kept pointed towards the sun through a yaw-steering algorithm (Kobel et al., 2021) which has the added benefit of breaking up the correlation with antenna PCO estimates from the orbit in-track and cross-track directions. For Sentinel-6 MF, both the spacecraft attitude profile and shape are significantly different from the Jason series. It is a house shaped spacecraft with fixed solar panels that cause significant shadowing on the sides and underside of the spacecraft. Flying with a roughly yaw-fixed profile causes SRP modeling errors to strongly correlate with the antenna PCO estimates and is most troublesome in the cross-track direction at high beta angles.

The goal of this study is to improve the the existing SRP force models for the Sentinel-6 MF spacecraft. Two different approaches are examined, an adjustment to the manufacturer provided macromodel (referred to as original macromodel for the remainder of this analysis), and the estimation of a composite SRP table. The macromodel surface properties are estimated using dynamic orbit solutions from which daily solutions are combined to form a final solution. The *a priori* SRP table is generated from the estimated macromodel and then adjusted using dynamic orbits by estimating separate stochastic solar scale parameters in the body-x/y/z directions. Antenna calibrations are separately estimated for each SRP model so that each POD solution includes a consistent SRP model and antenna calibration.

The performance of the estimated macromodel and SRP table are compared to the original macromodel using four POD solutions, consisting of three dynamic solutions and one reduced dynamic solution. The first 30-hour dynamic solution estimates drag and solar scale only. The second 30-hour dynamic solution estimates drag and once-per-orbit accelerations (cross-track/in-track) and is the basis for internal metrics analysis. The third 24-hour dynamic solution estimates the antenna offsets relative to the pre-launch antenna calibration along with drag and once-per-

orbit accelerations (cross-track/in-track). Finally, an external assessment of the orbit accuracy is performed using the SLR residuals measured against 30-hour reduced-dynamic orbits with applied ambiguity resolution. Using the estimated macromodel and SRP table we show improvements in all measures of POD performance. This includes drag and solar scale estimates, the antenna PCOs when estimated against the pre-launch antenna calibration, residual rms, orbit overlaps, and accuracy of reduced-dynamic ambiguity-resolved POD solution.

The remainder of this chapter is organized as follows: section 6.2 describes the study methods including background models, macromodel estimation, SRP table estimation, and POD solution strategies. Section 6.3 provides an analysis of the three SRP force models (the original macromodel; our estimated macromodel; and the SRP table) comparing drag and solar scale estimates, dynamic solution internal metrics, antenna offset estimates, and SLR residuals from reduced dynamic ambiguity-resolved orbits. Finally, section 6.4 discusses the findings and conclusions of this study.

## 6.2 Methods

Orbit solutions are generated from the TriG receiver GPS L1/L2 5-minute decimated phase and pseudorange measurements. We separately estimate an adjusted macromodel and SRP table using parameters estimated within dynamic orbit solutions. The estimated macromodel begins with the original macromodel as the *a priori*, and the SRP table subsequently takes the estimated macromodel as its *a priori*. All solutions employ single receiver ambiguity resolution (Bertiger et al., 2010b). Before estimation of the macromodel and SRP table the antenna offsets relative to the pre-launch antenna calibration are derived from solutions with beta angles near zero where it is expected that the cross-track solar radiation perturbation will be at a minimum. This combined with the maximum eclipse duration allows for a better estimate of the offsets. Because of the uncertainty in the body-y antenna offset, both the estimated macromodel and the SRP table are constrained to be symmetrical about the body-x/z plane.

### 6.2.1 Orbit Background Models

The orbit background models were implemented as described in Section 5.2. We applied the IGS14 GPS antenna calibrations, including both PCOs and PVs, except for the GPS IIIA transmitters, where a custom extension to the PVs has been computed for boresight angles larger than 14 degrees (Conrad et al., 2023a). The estimation of this extension is the topic for Chapter 7. It should be noted that the estimation of the GPS IIIA extension was done after the estimation of the macromodel but before the estimation of the SRP table, but all final solutions presented here apply the GPS IIIA PV extension.

### 6.2.2 Solution Strategies

The following subsections describe the general POD strategies applied to estimate the macromodel and SRP table. Table 6.1 shows the parameterizations of the initial state, carrier biases, and clock solutions that are consistent with the solution strategies for each method.

Table 6.1: General POD estimation strategy for all solutions

| Estimated Parameters | Parameterization | *a priori* $\sigma$ |
|---|---|---|
| **Epoch State** | | |
| 3-D epoch position (X,Y,Z) | Bias per solution | 10 $km$ |
| 3-D epoch velocity (X,Y,Z) | Bias per solution | 1 $km/s$ |
| **Carrier Phase Bias** | Constant bias per continuous carrier track | 1e6 $km$ |
| **TriG Clock Offset** | White-noise Process | 3e5 $km$ |

#### 6.2.2.1 Macromodel Estimation

The macromodel provides the predicted SRP acceleration through a collection of flat plates, each with a surface area, normal body-fixed vector, and reflection properties. The computation of SRP forces within GipsyX from the macromodel only takes into account these characteristics and

does not consider shadowing effects due to the relative positioning of the plates. The acceleration due to solar radiation pressure for a flat plate as derived by Milani et al. (1987) is given by

$$\ddot{\mathbf{a}} = -fA\cos(\theta)[2(\delta/3 + \rho\cos(\theta))\hat{\mathbf{n}} + (1-\rho)\hat{\mathbf{s}}] \tag{6.1}$$

where $A$ is the plate surface area, $\hat{\mathbf{n}}$ is the normal vector, $\hat{\mathbf{s}}$ is a unit vector that points from the plate to the radiation source, $\theta$ is the angle between $\hat{\mathbf{n}}$ and $\hat{\mathbf{s}}$, $\delta$ is diffusivity, $\rho$ is specularity, and $f$ is a scale factor. While not used explicitly here, the absorptivity, $\alpha$, is constrained such that $\delta + \rho + \alpha = 1$. The scale factor $f$ encompasses all constant parameters which scale the total acceleration such as the mass, radiation flux, as well as any accompanying solar scale factor.

When using a macromodel in GipsyX, the square root information filter can be configured for direct estimation of a global solar scale, surface area, specularity, or diffusivity. Care must be taken when estimating these values as the filter can produce unrealistic results such as negative surface areas when observability is low or highly correlated with another estimated property. Also, because individual plate properties are always highly correlated, estimation of multiple surface properties together is only done with small *a priori* uncertainties with 0.1 $m^2$ or below for areas and 0.02 or below for specularity and diffusivity.

Table 6.2: Original 12-surface macromodel as provided by the manufacturer (ESA, 2023)

| Surface | Surface Normal [x,y,z] | Area ($m^2$) | Diffusivity | Specularity |
|---|---|---|---|---|
| Body +x | [1.000, 0.000, 0.000] | 2.99 | 0.04 | 0.50 |
| Body -x | [-1.000, 0.000, 0.000] | 3.35 | 0.04 | 0.50 |
| Body +y | [0.000, 1.000, 0.000] | 2.87 | 0.04 | 0.50 |
| Body -y | [0.000, -1.000, 0.000] | 2.87 | 0.04 | 0.50 |
| Body +z | [0.000, 0.000, 1.000] | 9.03 | 0.02 | 0.60 |
| Body -z | [0.000, 0.000, -1.000] | 1.80 | 0.03 | 0.65 |
| Left SP (top) | [0.000, -0.616, -0.788] | 8.65 | 0.14 | 0.00 |
| Right SP (top) | [0.000, 0.616, -0.788] | 8.65 | 0.14 | 0.00 |
| AMR-C (top) | [0.469, 0.000, -0.883] | 0.92 | 0.08 | 0.00 |
| AMR-C (bottom) | [-0.469, 0.000, 0.883] | 0.92 | 0.56 | 0.19 |
| Left SP (bottom) | [0.000, -0.616, 0.788] | 4.09 | 0.16 | 0.00 |
| Right SP (bottom) | [0.000, 0.616, 0.788] | 4.09 | 0.16 | 0.00 |

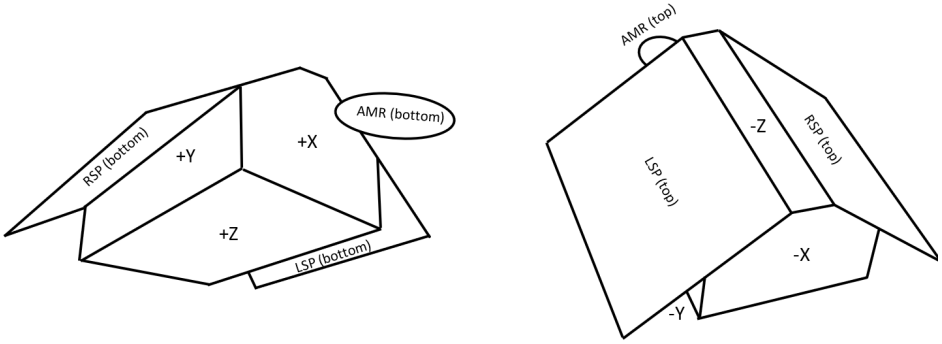


Figure 6.1: Relative position of the surfaces listed in Table 6.2 in the 12-sided macromodel

To estimate the specific macromodel surface properties, the original macromodel is set as the *a priori* for which the 12-sided model values are shown in Table 6.2 and Figure 6.1. The drag coefficient and solar scale are not estimated, but rather are fixed to 5.0 and 1.0, respectively. Fixing the drag coefficient to 5.0 for the is a somewhat arbitrary decision and the higher value is intended to prevent the drag estimate from becoming negative which was an issue for the macromodel. As mentioned before, the macromodel was estimated before the GPS IIIA extension, and so only the Block II observations are applied during this process.

Macromodel estimation is computed by first estimating only the body ±x surface areas and specularity during the first two yaw-flip maneuvers. During yaw-flip maneuvers, the Sentinel-6 MF attitude transitions from flying forward (yaw ∼0-deg) to flying backward (yaw ∼180-deg). After roughly 4-5 days this process is reversed. These yaw-flips occur when the beta angle is near zero degrees and correspond to the body-x surfaces being the most observable and provides a way to separate the drag force from the SRP forces. Next, with the ±x surfaces fixed, the y/z surface areas, specularity, and diffusivity are estimated together, again using small *a priori* $\sigma$'s (0.1 $m^2$ for area, 0.02 for specularity and diffusivity). A few well-defined surface parameters are not estimated, specifically the solar panel areas and the AMR-C properties, as the focus is primarily on adjustment of shadowed surfaces. The AMR-C bottom surface area and body vector are altered to only contribute in the +z direction. Symmetric surfaces about the body-x/z plane are constrained to have equal values (e.g. Solar Panel specularity and diffusivity). Estimates from 24-hour daily

solutions are weighted by the formal error and averaged across approximately 300 days to produce the final macromodel estimate.

#### 6.2.2.2 Solar Radiation Pressure Table

The SRP table computes the total composite surface force acting on the spacecraft based on the azimuth and elevation of the sun vector with respect to the body frame. The elevation is the angle between the sun vector and the body-x/z plane, defined positive in the direction of the +y axis. The azimuth is the angle between the projection of the sun vector in the body-fixed x/z plane and the +x axis, increasing counter-clockwise about the +y axis. Because Sentinel-6 MF is roughly yaw-fixed, this results in an elevation angle that is correlated with the beta angle. Unlike the macromodel where only a single solar scale for the entire spacecraft body can be estimated, the SRP table allows estimation of a separate solar scale for each body-fixed axis. The solution strategy adopted here for the SRP table is to estimate a solar scale for the body-x/y/z directions from more than 50 independent 10-day orbit solutions. Solutions with orbit maneuvers are excluded from the final solution. The drag coefficient is fixed to 3.0 with drag forces being computed from the estimated macromodel surface areas. The solar scale values are then estimated in a stochastic manner, and updated at each measurement epoch (300-sec) using a 30-second correlation time with an *a priori* uncertainty of 0.1. Solar scale values are binned based on the sun line-of-sight azimuth and elevation and the median values are then used to scale the *a priori* values of the SRP table.

The resulting SRP table has improved drag and solar scale estimates, but does not fully remove the beta angle dependence of the antenna y-offset estimates. A final elevation-only correction to the body-y forces is applied to improve the consistency of these estimates. This correction is achieved by fitting a 6th order polynomial curve to the y-offsets as a function of the sun elevation in the body-frame. This curve is then scaled using an empirically derived 1 $nm/s^2$ per 1 $mm$ of predicted offset from the fit. After conversion of the elevation dependent acceleration to force, this is then added to the SRP table. This correction is relatively small, changing only the total

acceleration in the body-y direction by about 1 - 6 $nm/s^2$ or in terms of force roughly 1 - 7 $\mu N$. Once again, symmetry is enforced about the body-x/z plane.

### 6.2.3 Antenna Calibration

As described in Chapter 3, the antenna calibration corrects for delays based on the signal line-of-sight direction. Given the three different SRP models: original macromodel, estimated macromodel, and SRP table; a separate antenna calibration is estimated for each applied SRP model. This produces a antenna calibration that is consistent with the SRP model when processed in reduced-dynamic solutions. The overall estimation strategy for each follows the description in Section 3.2.1. Additional constraints are applied to the estimated PVs as described in more detail in Section 5.5.

### 6.2.4 Reduced-Dynamic Orbit Solutions

Reduced-dynamic orbit solutions are produced following the strategy described in Section 5.2 and summarized in Table 5.2. To achieve the most accurate POD solution, we estimate reduced-dynamic solutions and apply ambiguity resolution for each SRP model. These solutions have identical processing strategies while changing only the SRP model and associated antenna calibration to form the basis for external assessment using SLR measurements.

## 6.3 Results

To develop and compare the proposed methods, we process a total of 578 days of TriG receiver GPS L1/L2 5-minute decimated phase and pseudorange measurements across the time span of 2021-01-01 to 2022-08-01. We first compare the resulting estimated drag and solar scale from 24-hour dynamic orbits with the original macromodel, estimated macromodel, and SRP table. Next, orbit quality is evaluated for 30-hour dynamic orbits (estimating drag and once-per-orbit empirical accelerations in the in-track and cross-track components) by comparisons of the standard internal metrics; post-fit residual rms, overlap statistics, and ambiguity resolution fixing statistics. This

is followed by estimation of daily antenna offsets relative to the pre-launch antenna calibration for each model within 24-hour dynamic orbit solutions. The statistics for all daily solutions are reported in terms of the mean value ± the standard deviation of the full set of daily solutions after $5\sigma$ outlier removal. Finally, independent SLR measurement residuals are assessed to evaluate the accuracy of 30-hour reduced-dynamic orbit solutions with applied ambiguity resolution for all three SRP models.

### 6.3.1 Estimated Macromodel and SRP Table

Table 6.3 lists the estimated macromodel plates and surface properties. When compared to the *a priori* model in Table 6.2, surfaces that experience a significant amount of shadowing show significant changes to the plate properties. This is most notable for the underside of the solar panels and body ±y surfaces. In effect, the estimated parameters likely account for the lack of a shadowing model, rather than errors in the actual physical properties. We see that at high beta angles, the solar panels will shadow the ±y surfaces, but the macromodel will still compute a contribution from them resulting in an SRP force that is too large. The body ±x surface also show significant

Table 6.3: Estimated 12-surface macromodel and change (Δ) relative to Table 6.2

| Surface | Surface Normal [x,y,z] | Area ($m^2$) | Diffusivity | Specularity |
|---|---|---|---|---|
| Body +x | [1.000, 0.000, 0.000]* | 4.149 (+1.159) | 0.041 (+0.001) | 0.349 (-0.151) |
| Body -x | [-1.000, 0.000, 0.000]* | 3.941 (+0.591) | 0.042 (+0.002) | 0.546 (+0.046) |
| Body +y | [0.000, 1.000, 0.000]* | 1.329 (-1.541) | 0.040 (+0.000) | 0.506 (+0.006) |
| Body -y | [0.000, -1.000, 0.000]* | 1.329 (-1.541) | 0.040 (+0.000) | 0.506 (+0.006) |
| Body +z | [0.000, 0.000, 1.000]* | 11.830 (+2.800) | 0.016 (-0.004) | 0.571 (-0.029) |
| Body -z | [0.000, 0.000, -1.000]* | 2.072 (+0.272) | 0.030 (+0.000) | 0.660 (+0.010) |
| Left SP (top) | [0.000, -0.616, -0.788]* | 8.65* | 0.316 (+0.176) | 0.139 (+0.139) |
| Right SP (top) | [0.000, 0.616, -0.788]* | 8.65* | 0.316 (+0.176) | 0.139 (+0.139) |
| AMR-C (top) | [0.469, 0.000, -0.883]* | 0.92* | 0.080* | 0.000* |
| AMR-C (bottom) | [0.000 ,0.000, 1.000]* | 0.8123* | 0.56* | 0.19* |
| Left SP (bottom) | [0.000, -0.616, 0.788]* | 3.760 (-0.330) | 0.164 (+0.004) | 0.013 (+0.013) |
| Right SP (bottom) | [0.000, 0.616, 0.788]* | 3.760 (-0.330) | 0.164 (+0.004) | 0.013 (+0.013) |

*parameters not estimated

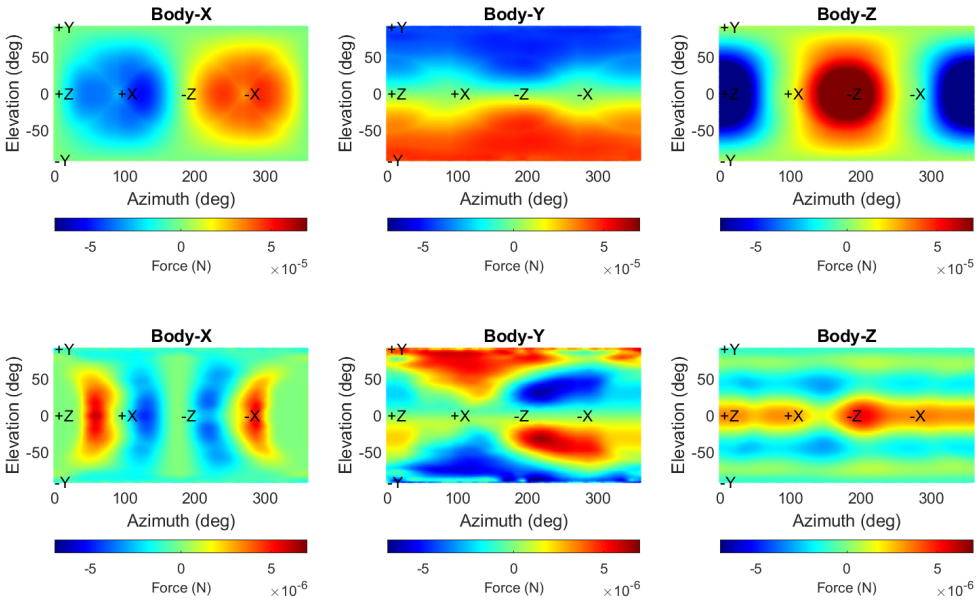


Figure 6.2: Estimated solar radiation table force values as a function of sun position. Top panels show the total body-x (left), body-y (middle), and body-z (right) force. Lower panels show the difference in the force produced between the newly estimated macromodel and SRP table. Note the scale is smaller by a factor of 10

changes relative to the original macromodel. Here the fairly large change in the surface areas is likely a result of finding a fit to the SRP forces and do not represent a real effect.

Figure 6.2 shows the total force produced by the SRP table (top panels) after scaling the *a priori* SRP table (derived from estimated macromodel) with the binned estimated solar scale factors. The bottom panels show how it differs from the *a priori* SRP table. The scale on the upper panels is a factor of 10 larger than the lower values. It should be noted that the nadir pointed face of Sentinel-6 MF never receives direct sunlight due to eclipsing and so the portions of the SRP table near the +z direction cannot be estimated accurately. This is evident in the bottom panels of Figure 6.2 for the body-x/y forces. Also, sun positions with an elevation near ±90 degrees occur during the maximum beta angle, for which the available data are very limited. This lack of observations explains the noisy features seen in the body-y component of the SRP table at high sun elevations.

### 6.3.2 Drag and Solar Scale

Figures 6.3 and 6.4 show the time history of the drag and solar scale estimates from 30-hour dynamic orbit solutions for the original macromodel (green), estimated macromodel (blue), and SRP table (red). Given the high altitude of Sentinel-6 MF, the drag force is expected to be smaller than the SRP forces by approximately two orders of magnitude. In this estimation strategy, it appears that the drag coefficient is absorbing in-track solar radiation pressure modeling errors. This is evident for the original macromodel where there is a large sign change after Sentinel-6 MF performs a yaw-flip. The elimination of this anomaly in the drag coefficient is the most significant

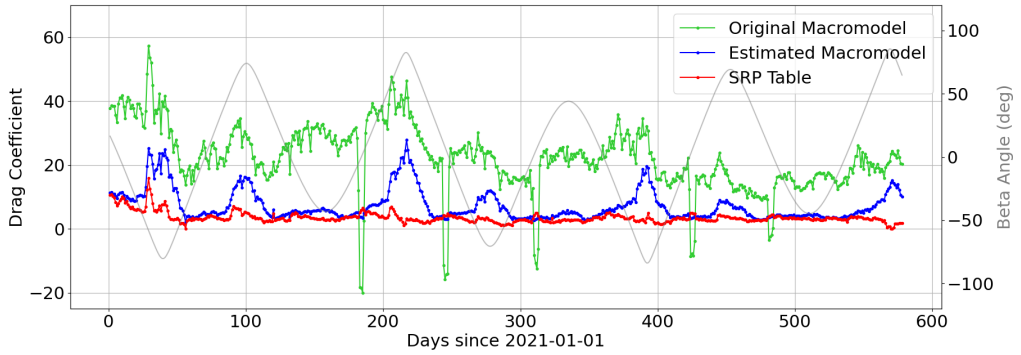


Figure 6.3: Daily drag coefficient estimate for original macromodel (green), estimated macromodel (blue), and SRP table (red). The beta angle is plotted in grey against the right axis

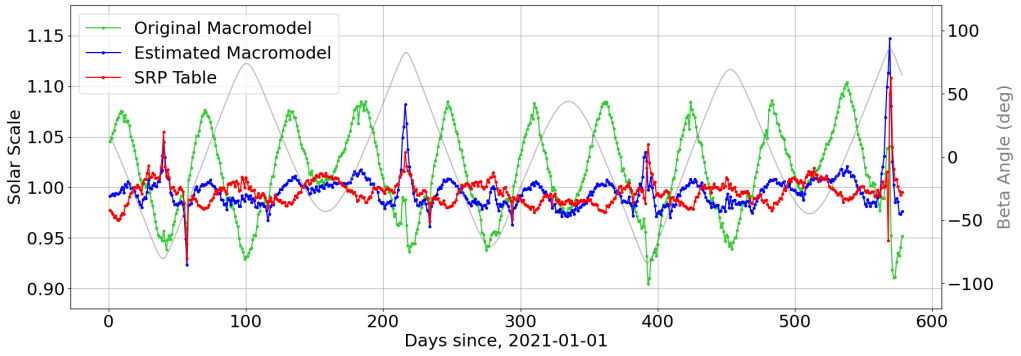


Figure 6.4: Daily solar scale estimate for original macromodel (green), estimated macromodel (blue), and SRP table (red). The beta angle is plotted in grey against the right axis

Table 6.4: Drag coefficient and solar scale in terms of the mean ± the standard deviation of daily estimates after $5\sigma$ outlier removal

| | Drag Coefficient | Solar Scale |
|---|---|---|
| Original Macromodel | 22.9 ± 9.4 | 1.013 ± 0.043 |
| Estimated Macromodel | 7.23 ± 4.7 | 0.995 ± 0.012 |
| SRP Table | 3.43 ± 1.4 | 0.995 ± 0.011 |

effect produced by the new SRP models. Table 6.4 shows the mean daily solution ± the overall standard deviation of the drag and solar scale estimates. The mean drag coefficient for the SRP table is very close to the fixed value of 3 applied during estimation. Using the SRP table produces the most realistic and consistent estimates for the drag coefficient with a mean value of 3.43 and an overall standard deviation of 1.4 after $5\sigma$ outlier removal. Looking at Table 6.4 as well as Figures 6.3 and 6.4, we see the original macromodel has significant structure in the solar scale time history with a strong correlation to the beta angle. In the time history, the estimated macromodel and SRP table both perform well except at the highest beta angles (> 85-deg). This is to be expected given the limited amount of data available to tune the Sentinel-6 MF SRP models at higher beta angles.

### 6.3.3 Dynamic Orbit Solution Internal Metrics

To assess impact of the new SRP models on the precision of the orbit, we first examine 30-hour dynamic orbits, estimating drag and once-per-orbit accelerations in the cross-track and in-track directions. We also apply ambiguity resolution to these solutions by applying a soft constraint

Table 6.5: Residual rms and ambiguity resolution percentage in terms of the mean ± the standard deviation of daily statistics after $5\sigma$ outlier removal

| | Phase (mm) | Pseudorange (mm) | Ambiguity Resolution (%) |
|---|---|---|---|
| Original Macromodel | 7.0 ± 1.3 | 690 ± 120 | 55.9 ± 9.7 |
| Estimated Macromodel | 6.6 ± 0.6 | 670 ± 60 | 60.0 ± 6.9 |
| SRP Table | 6.5 ± 0.6 | 670 ± 60 | 60.3 ± 6.4 |

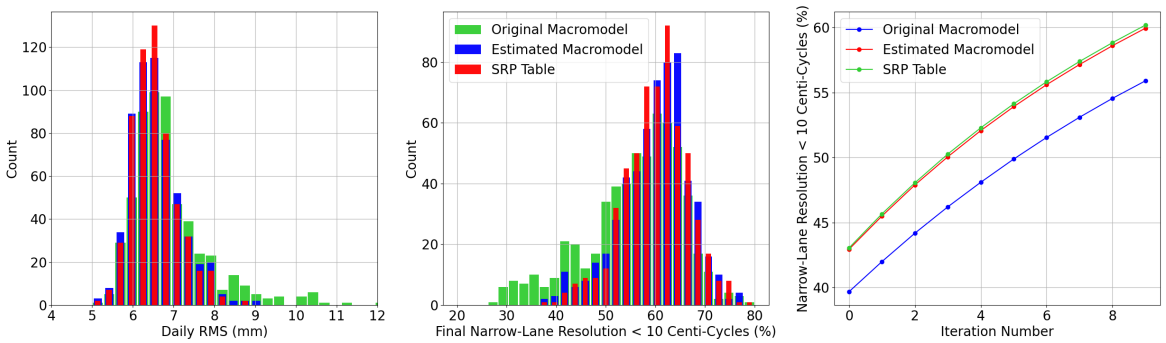


Figure 6.5: Histogram of the daily phase residual rms (left), daily constrained narrow-lane ambiguity resolution to less than 10 centi-cycles (middle), and mean narrow-lane ambiguity resolution after each iteration (right) for original macromodel (green), estimated macromodel (blue), and SRP table (red)

to the double-differences and iterating 10 times. Figure 6.5 shows the distribution of the daily solution phase residual rms values (left), the narrow-lane ambiguity resolution as a percentage of passes constrained to within one tenth of a cycle after the final iteration (middle), and the percentage of passes constrained after each iteration (right). Table 6.5 shows the overall statistics for each solution after $5\sigma$ removal. Both the estimated macromodel and SRP table perform better than the original macromodel with a decrease in the mean daily phase residual rms from 7.0 mm to 6.5 mm along with a reduction in the daily solution standard deviation from 1.3 mm to 0.6 mm. This is accompanied by a more than 4% increase in the successful ambiguity resolution.

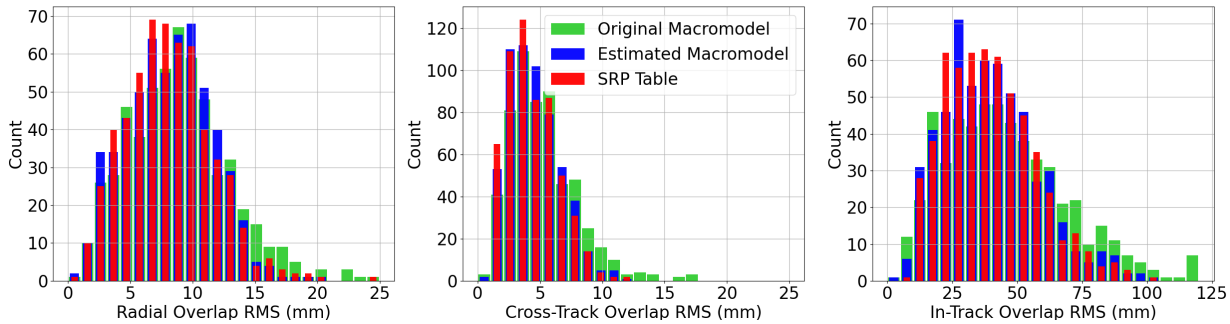


Figure 6.6: Histogram of the daily radial, cross-track, and in-track overlap differences for original macromodel (green), estimated macromodel (blue), and SRP table (red)

The dynamic orbit solution precision can be evaluated from the 30-hour arcs by computing the rms of the component differences during the 6-hour overlap period. To avoid edge effects, only the central four hours of the overlap period are evaluated. Figure 6.6 shows the statistics of the radial, cross-track, and in-track overlap difference rms for all three SRP models. Table 6.6 shows the mean rms across all days ± the overall standard deviation after $5\sigma$ outlier removal. Both the estimated macromodel and SRP table are more consistent than the original macromodel, with both smaller mean overlap values, and lower variability from day-to-day. The better overall cross-track performance compared to radial is likely due to the estimation strategy only including empirical accelerations in the cross-track and in-track components.

Table 6.6: Rms of the radial, cross-track, and in-track component overlap differences in terms of the mean ± the standard deviation daily differences after $5\sigma$ outlier removal

| | Radial Overlap (mm) | Cross-track (mm) | In-track (mm) |
|---|---|---|---|
| Original Macromodel | 9.6 ± 5.9 | 5.2 ± 2.7 | 51 ± 37 |
| Estimated Macromodel | 8.2 ± 3.5 | 4.5 ± 2.0 | 40 ± 18 |
| SRP Table | 8.3 ± 4.0 | 4.4 ± 2.0 | 40 ± 17 |

#### 6.3.3.1 Antenna offsets

Antenna offsets are estimated within 24-hour dynamic orbit solutions together with drag and once-per-orbit empirical accelerations in the cross-track and in-track components applying the

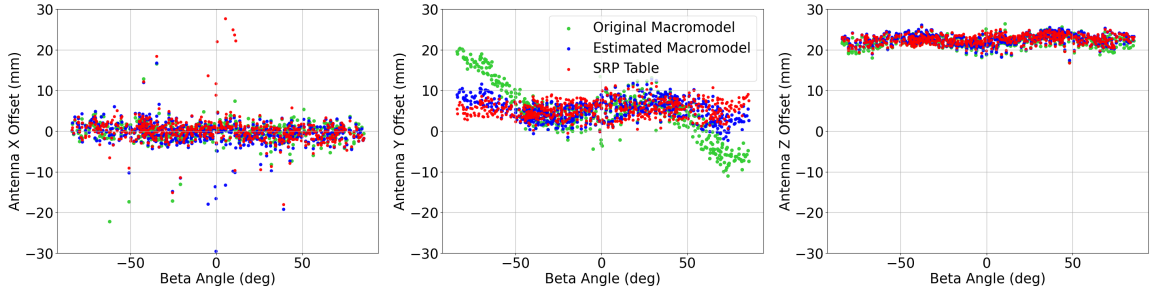


Figure 6.7: Estimated antenna offsets relative to nominal pre-launch calibrations for original macromodel (green), estimated macromodel (blue), and SRP table (red)

Table 6.7: Antenna offsets in terms of the mean ± the standard deviation of the daily estimates after $5\sigma$ outlier removal. Note: the x-offset is aligned with the in-track, y-offset with cross-track, and z-offset with radial

| | x-offset (mm) | y-offset (mm) | z-offset (mm) |
|---|---|---|---|
| Original Macromodel | -0.470 ± 7.3 | 4.93 ± 5.8 | 22.15 ± 1.3 |
| Estimated Macromodel | -0.448 ± 2.8 | 5.25 ± 2.6 | 22.53 ± 1.2 |
| SRP Table | 0.047 ± 2.9 | 5.35 ± 2.0 | 22.51 ± 1.1 |

pre-launch antenna calibrations. This is done to be consistent with the method used to estimate the full antenna calibration and allow for an understanding of how the SRP model can influence the estimated antenna PCOs. Figure 6.7 shows the daily antenna offsets relative to the nominal values estimated as constant parameters across the solution arc. Because Sentinel-6 MF is roughly yaw fixed, the body-x offset is highly correlated with the in-track direction and is difficult to resolve. Because of this, the *a priori* x-offset uncertainty was set to 2 mm to reduce the daily scatter but opened up to 20 mm for the y and z-offsets which are more observable.

The resulting estimated antenna y-offsets have a strong beta angle dependency for the original macromodel that is greatly reduced when using both the estimated macromodel and the SRP table. Table 6.7 shows the overall mean and standard deviation of the offsets where the SRP table shows a reduction in the standard deviation from 5.8 mm to 2.0 mm when compared to the original macromodel. While the z-offset has some beta angle dependence, it only varies by a few millimeters and is relatively consistent across all three solutions. The large bias in the z-offset is likely due to interactions with the applied transmitter calibrations. For the y-offsets, the original macromodel has a strong beta angle dependence with a nearly 3 cm spread. This type of behavior for the y-offset means that a resulting antenna calibration would be dependent on the distribution of the beta angle during estimation. Over long estimation periods this would likely average out, but early in in the mission when data is lacking, it could be heavily influenced by the relative beta angle distribution.

The applied SRP table highlights the potential benefits and issues of using an empirical

model. It is possible to completely remove the estimated antenna y-offset beta angle dependence through an empirical elevation correction of 1 $nm/s^2$ per 1 mm of offset. We can be confident in the solution due to enforcing symmetry about the body-xz plane and the resulting lack of beta angle dependence in the final results, but it does highlight the potential issue of fitting the SRP table to incorrect or unknown antenna offsets.

### 6.3.4 Reduced Dynamic Solutions

The internal metrics for the reduced dynamic ambiguity-resolved orbits are shown in Table 6.8. The most significant improvement with both the estimated macromodel and SRP table is in the ambiguity resolution. Here there is nearly a 1-percent increase in passes fixed to a tenth of a cycle, along with a decrease in the ambiguity resolution standard deviation. There is also a reduction in the phase residual rms as seen in both the mean and standard deviation. Because the reduced dynamic process allows the solution to fit the measurements better, it is not surprising to see similar values for all three SRP modeling for the overlap statistics. There is a small improvement in the standard deviation of the cross-track overlap difference rms for the SRP table indicating a more consistent cross-track solution.

Table 6.8: Phase residual rms, ambiguity resolution percentage, radial (R), cross-track (C), and in-track (I) component overlap differences for reduced dynamic orbit solutions in terms of the mean $\pm$ the standard deviation of the daily values after $5\sigma$ outlier removal

| | LC rms (mm) | Amb Res (%) | R (mm) | C (mm) | I (mm) |
|---|---|---|---|---|---|
| Original Macromodel | 5.0 $\pm$ 0.32 | 83.1 $\pm$ 3.2 | 0.75 $\pm$ 0.26 | 1.7 $\pm$ 0.60 | 1.7 $\pm$ 0.55 |
| Estimated Macromodel | 4.8 $\pm$ 0.27 | 84.1 $\pm$ 2.5 | 0.74 $\pm$ 0.26 | 1.7 $\pm$ 0.57 | 1.7 $\pm$ 0.56 |
| SRP Table | 4.8 $\pm$ 0.27 | 84.2 $\pm$ 2.5 | 0.74 $\pm$ 0.26 | 1.6 $\pm$ 0.55 | 1.7 $\pm$ 0.55 |

#### 6.3.4.1 SLR Residuals

As a final evaluation of the original macromodel, estimated macromodel, and SRP table, we examine the independent SLR residuals measured against ambiguity-resolved reduced dynamic orbits. Only SLR stations with a mean bias below 5 mm and overall standard deviation below 10 mm are examined. These include a total of six stations: Greenbelt, Maryland; Graz, Austria; Herstmonceux, United Kingdom; Mt Stromlo, Australia; Yarragadee, Australia; and Wettzell, Germany with a combined measurement total of 88,722 after $5\sigma$ outlier removal. Figure 6.8 shows the one-way SLR residual rms and mean as a function of off-nadir angle relative to the laser retroreflector array. The estimated macromodel and SRP table both perform better than the original macromodel with overall SLR residual rms values decreasing from 8.6 mm to 8.1 mm as shown in in Table 6.9. There is also a small reduction in the overall SLR residual mean value from about 2.0 mm to 1.6 mm. Limiting the SLR residuals to below 40 degrees off-nadir angle, further

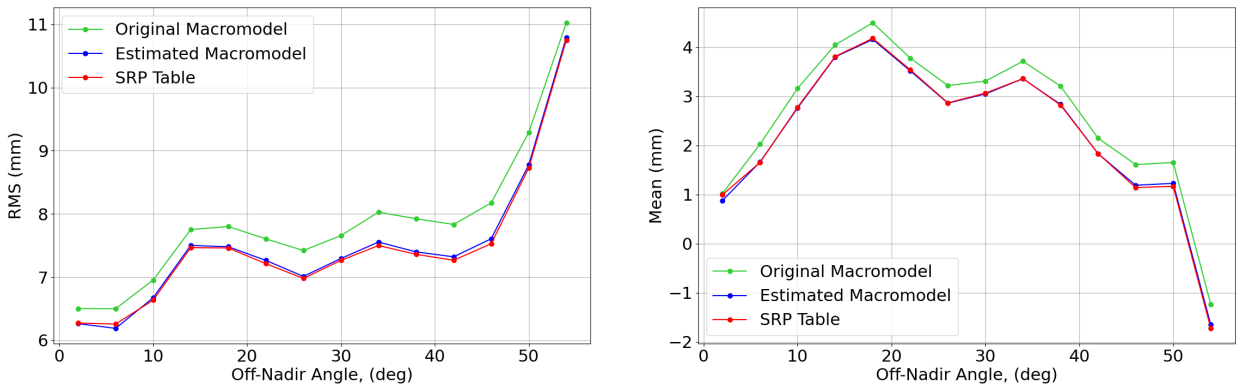


Figure 6.8: SLR residual rms (left) and mean (right) as a function of off-nadir angle in the SLR reference frame for original macromodel (green), estimated macromodel (blue), and SRP table (red)

Table 6.9: SLR residual rms and mean

| | rms (mm) | std (mm) | rms < 40-deg (mm) | mean (mm) |
|---|---|---|---|---|
| Original Macromodel | 8.6 | 8.3 | 7.8 | 2.03 |
| Estimated Macromodel | 8.1 | 7.9 | 7.3 | 1.65 |
| SRP Table | 8.1 | 7.9 | 7.3 | 1.62 |

reduces the residual rms to 7.3 mm for the estimated macromodel and SRP table. Lower off-nadir angles are dominated by the radial errors and here indicate better than 1 cm (rms) radial orbit accuracy.

## 6.4 Summary

Solar radiation pressure modeling is an important component of precise orbit determination. The presence of mismodeled dynamics can degrade the estimated antenna calibrations which are estimated within dynamic solutions. We show an improvement to the SRP modeling for Sentinel-6 MF with both an estimated macromodel and SRP table. Both estimated SRP models produce more consistent estimates for drag and solar scale, dynamic solution internal metrics, and antenna offsets relative to the pre-launch calibrations when compared to the manufacture provided macromodel. Independent SLR residuals measured against reduced dynamic ambiguity-resolved orbits are improved from 8.6 mm to 8.1 for both the estimated macromodel and the SRP table.

# Chapter 7

# Extending the GPS IIIA antenna calibration for precise orbit determination of low Earth orbit satellites

## 7.1 Introduction

Accurate antenna calibration for the GNSS transmitters and the LEO based receiver (Schmid et al., 2005, 2007) is essential to achieve POD accuracy at the desired level of below 1 cm radial rms. For transmitters, the IGS provides a unique PCO for each satellite. The IGS PVs, however, are modeled to be identical for every satellite within a GPS sub-block and only describe variations as a function of boresight angle (Montenbruck et al., 2015a). These were initially restricted to nadir angles less than 14 degrees, the limit of what is observed by ground stations. For LEO satellites such as Sentinel-6 MF, however, boresight angles greater than 14 degrees are regularly observed. Jäggi et al. (2010) proposed an extension of the IGS05 PVs beyond 14 degrees which was generated from simultaneous estimation of GPS and LEO antenna calibrations using only GPS measurements collected onboard multiple LEO satellites. Later, a similar approach was also used by Schmid et al. (2016) to estimate the GPS PVs beyond 14 degrees. These extensions were done only for the Block II IGS antenna calibrations which are separated into six sub-block groups: II, IIA, IIR-A, IIR-B, IIR-M, and IIF. For the remainder of this chapter, we collectively refer to all these sub-blocks as Block II while applying the specific IGS14 sub-block PVs and individual PCOs. Additionally, for the purposes of comparison the sub-block types IIR-B and IIR-M are combined due to having identical IGS14 PVs.

For several subsequent reference frame realizations, only the PCOs have been changed while

the PVs have remained fixed to those provided by Jäggi et al. (2010) for IGS05. Each IGS realization of the International Terrestrial Reference Frame (ITRF) must update the transmitter PCOs due in part to the reference frame scale changes. For example, Schmid et al. (2016) estimated updated PCOs for the IGS08 definition of transmitter phase calibrations and Rebischung and Schmid (2016) updated the IGS14 values of the PCOs while continuing to adopt the PVs from IGS05.

The GPS constellation is currently in the process of incorporating new GPS IIIA transmitters, with the first satellite launched in December 2018 (Thoelert et al., 2019). As of December 2021, the GPS constellation includes 5 GPS IIIA satellites in operation with space vehicle numbers (SVN) 74 - 78. Unlike the Block II IGS14 antenna calibration that inherited the full IGS05 extension calibration values, the IGS14 GPS IIIA PVs are adopted as varying with boresight angle up to 14 degrees, then held constant for larger angles. The GPS IIIA PCO values were provided by the manufacturer (Lockheed Martin, 2019) for the first GPS IIIA satellite, SVN-74. Steigenberger et al. (2020) found that these values had good agreement with on orbit estimates of the PCO. For subsequent GPS IIIA transmitters, the IGS14 adopted the SVN-74 PCO values.

In this study, we aim to generate an extension of the IGS14 GPS IIIA PVs for boresight angles higher than 14 degrees that is consistent with the Block II antenna calibrations. This approach facilitates the continuity of POD solutions based on IGS standards during and after the transition of the GPS constellation from Block II to GPS IIIA transmitters. To extend the GPS IIIA antenna calibrations above 14 degrees, we use the Sentinel-6 MF GPS L1/L2 carrier and pseudorange observations from the TriG receiver (Donlon et al., 2021b). At the nominal altitude of 1336 km, Sentinel-6 MF routinely observes GPS measurements with boresight angles greater than 14 degrees. Sentinel-6 MF is an ideal platform for extending the GPS IIIA antenna calibration because of its altitude, geodetic quality receivers and antennas with favorable multipath, and already demonstrated radial orbit accuracy better than 1 cm rms (Montenbruck et al., 2021). Additionally, during the majority of 2021, Sentinel-6 MF was flying in tandem with Jason-3 where it is following the same ground track, but approximately 30 seconds behind (Donlon et al., 2021a).

Thus, we can use Jason-3 to validate the Sentinel-6 MF derived GPS IIIA antenna calibration extension.

To produce a GPS IIIA antenna calibration extension consistent with the IGS14 Block IIs, we implement the following approach. We first generate a Sentinel-6 MF receiving antenna calibration based only on GPS Block II tracking data and using the IGS14 definition of the transmitter antenna calibrations. With this receiver antenna calibration, Block II based dynamic orbit and clock solutions for Sentinel-6 MF are estimated. We then use residuals from the withheld GPS IIIA tracking data and predicted observables based on the dynamic orbit and clock solutions to determine the GPS IIIA dependency on boresight angle, namely the PV. The IGS14 definition of the PCO is held fixed. Finally, to test the fidelity of the proposed extension, we compare orbit solutions with and without GPS IIIA satellites for Jason-3 - a LEO satellite not used in the calibration procedure.

Section 7.2 describes the POD models and solution strategy, the Sentinel-6 MF receiver antenna calibration method, and the GPS IIIA antenna calibration extension process. In Section 7.3 we assess the validity of the calibration by comparing orbit metrics for three different scenarios. The first POD solution uses only Block II measurements; the second includes Block II and IIIA measurements with the original IGS14 antenna calibrations; and finally the third includes Block II and IIIA measurements with the newly generated GPS IIIA antenna calibration extension. Section 7.4 describes validation of the GPS IIIA calibration extension using Jason-3 as an independent platform. In Section 7.5 we provide the overall conclusions and recommendations.

## 7.2 Methods

### 7.2.1 Sentinel-6 MF Instrumentation

The Sentinel-6 MF POD in this chapter exclusively uses the undifferenced GPS L1/L2 pseudorange and carrier measurements received by TriG POD antenna. For this analysis, the TriG measurements are preferable for a few reasons. First, observations are tracked down to 0 degrees elevation whereas the primary PODRIX receiver enforces a cut off at 10 degrees. These low el-

evation measurements in the receiver frame result in more observations for transmitter boresight angles above 14 degrees. Second, because the Trig only tracks GPS signals (PODRIX tracks both GPS and Galileo), this allows for a more robust Block II only solution due to significantly more GPS measurements. In a manner similar to Bertiger et al. (2010a), the raw 1 Hz measurements are decimated to a 5-minute dual-frequency (ionosphere-free) combination for the GPS carrier and pseudorange (LC and PC) observations.

### 7.2.2 Orbit Models/Solution Strategy

We apply the background models described in Section 5.2 and listed in Table 5.1 including the IGS14 GPS antenna calibrations for both PCOs and PVs from igs14_2194.atx (Rebischung and Schmid, 2016) except for where we specifically note that we have applied our new estimates of the GPS IIIA PV extension for boresight angles larger than 14 degrees. The orbit solution strategy for the reduced-dynamic, ambiguity resolved orbits were described in Section 5.2 and summarized in Table 5.2.

### 7.2.3 Sentinel-6 MF Antenna Calibration

The Sentinel-6 MF TriG receiver antenna calibration is generated using only the GPS Block II measurements. Because the receiver and transmitter antenna calibrations are inherently coupled, this approach anchors the Sentinel-6 MF antenna calibration to the established IGS14 Block II transmitter calibrations. The receiver antenna calibration is estimated from daily solutions generated from 24-hour dynamic orbit estimates (including daily estimates of drag coefficient and once per revolution accelerations in cross-track and in-track). We first perform a daily orbit solution using the pre-launch measurements of the receiver calibration and with all Block II tracking data. From this solution we identify outliers, which are then excluded from a subsequent dynamic orbit solution that also simultaneously estimates a two-dimensional correction to the pre-launch receiver calibration. The estimated antenna calibration correction is defined over discrete bins of 3 degrees in elevation and 4 degrees in azimuth for elevations below 51 degrees. Above this, the azimuth

bin spacing is variable to account for lower measurement density at higher elevations. Outliers are removed as they can significantly influence the receiver calibration, especially for bins with low measurement density. The sum of the pre-launch calibration and the estimated correction then forms the total receiver antenna calibration which corrects for line-of-sight variations due to antenna gain patterns and spacecraft multipath.

We use the tuned custom macromodel presented in Chapter 6 which produced much more consistent antenna offsets estimates as a function of the beta angle when compared to the manufacturer provided macromodel (the SRP table described in Chapter 6 was not used as it was developed after this study on the GPS IIIA extension). The final Sentinel-6 MF antenna calibration is generated by accumulating the final Square Root Information Filter (SRIF) state outputs from each Block II-only daily solution into a single estimate over the accumulated time frame. It is during this process that the average of all bins above 30 degrees elevation and body-x offset are constrained to zero.

### 7.2.4 GPS IIIA Antenna Calibration Extension

Unlike the Block II variants, the current IGS14 GPS IIIA antenna calibrations above 14 degrees, as seen in Figure 7.1, are fixed to the value from the 14 degree boresight angle. Here we

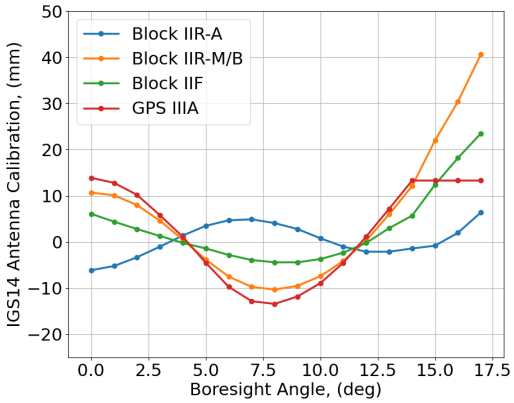


Figure 7.1: IGS14 PVs as a function of boresight angle separated by block type from igs14_2194.atx. Note: Block IIR-B antenna PVs are the same as IIR-M

describe the approach taken to extend them to 17 degrees. We note that JPL's final orbit and clock solutions for the GPS constellation used in our solution are determined from a global ground network. Because of this, the GPS orbit and clock products only depend on the IGS14 calibration values for boresight angles less than 14 degrees. For this reason, we choose to limit our modification of the IGS14 GPS IIIA calibration values to boresight angles greater than 14 degrees to improve the LEO POD without affecting terrestrial GNSS processing with IGS14 values.

To ensure the GPS IIIA antenna calibration extension is derived relative to the Block II, a two-iteration process is implemented. First, Sentinel-6 MF dynamic orbit solutions are estimated using only Block II measurements and the corresponding receiver antenna calibration we computed earlier. The orbit and receiver clock solutions are then fixed, and the GPS IIIA dual-frequency phase measurements are fit to those Block II-based dynamic orbit solutions, estimating only phase biases for each arc. The resulting GPS IIIA residuals are zero mean across all boresight angles. This results in an undesired mean residual offset below 14 degrees that is due primarily to poorly modeled calibration values above 14 degrees. To facilitate a consistent calibration for the higher boresight angles, the stacked GPS IIIA residuals are offset such that their mean value below 14 degrees over the entire data set is zero. From this starting point, we iterate a solution based on the fixed Block II orbits and clock solution with updates to the GPS IIIA antenna calibration above 14 degrees based on stacked post-fit residuals. Our approach ensures that the new GPS IIIA antenna calibration extensions are consistent with the IGS14 Block II antenna calibrations.

## 7.3 Results

We use the TriG receiver GPS L1/L2 5-minute decimated phase and pseudorange measurements from the entirety of 2021 for all subsequent results; except for the antenna calibration which uses 30-second data over a slightly longer time span. The following sections first describe the resulting receiver antenna calibration and GPS IIIA satellite antenna calibration extension estimated from 24-hour solutions. We evaluate the consistency of the GPS IIIA antenna calibration extension by comparing reduced-dynamic ambiguity resolved 30-hour precise orbit solutions from three cases:

using only Block II tracking data with IGS14 antenna calibration, using Block II and IIIA tracking data with default IGS14 antenna calibration, and using Block II and IIIA tracking data with IGS14 calibration modified to include our extensions above 14 degree boresight angles. Orbit quality is evaluated using comparisons of internal metrics. The statistics for the daily solutions are reported in terms of the mean value ± the standard deviation of the full year of daily solutions. Finally, withheld SLR measurements are independently applied to evaluate the orbit solution accuracy for all three scenarios.

### 7.3.1 Antenna Calibrations

#### 7.3.1.1 Sentinel-6 MF Antenna Calibration

The Sentinel-6 MF antenna calibration is generated from more than one year of data spanning from 2021-01-01 to 2022-02-13. High-rate 30-second L1/L2 ionosphere-free dual-frequency combination observations from Block II only measurements for the phase and P(Y)-code measurements are applied. Daily solutions with fewer than 18,000 phase measurements and daily rms of post-fit phase residuals above 5.5 mm, along with days that have orbit maintenance maneuvers, are excluded from the final estimate of the receiver calibration resulting in a total of 388 daily so-

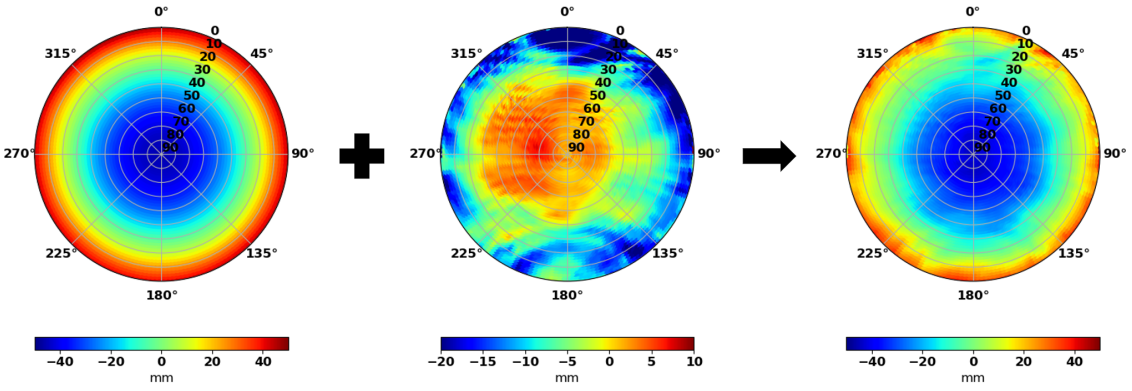


Figure 7.2: Sentinel-6 MF pre-launch phase antenna calibration (left) combined with the estimated antenna calibration correction (middle) and resulting in-flight Block II derived phase antenna calibration (right)

lutions. The final estimated antenna calibrations are generated for both phase and code solutions. Figure 7.2 shows a comparison of the L1/L2 dual-frequency phase pre-launch anechoic chamber antenna calibration, the estimated correction, and the resulting in-flight Block II derived antenna calibration. As expected, the overall structure is similar between the original and the final, but there is significant irregular structure with variations on the order of -20 to 10 mm in portions of the antenna calibration captured in the in-flight environment, presumably due to multipath and a significant z-PCO contribution. When compared to the pre-launch antenna calibration, the resulting PCO offsets in the antenna y and z directions are -3.8 mm and -20.0 mm respectively. For our implementation, we do not separate out the PCO from the estimated calibration, but rather retain the antenna reference point in Table 5.1 and allow the antenna calibration to absorb the estimated offsets.

A consideration for the use of high-rate data is due to the yaw-fixed attitude of Sentinel-6 MF. Delays in acquiring signals from rising satellites results in relatively few measurements for elevations below 6 degrees in the in-flight direction, making this portion of the antenna calibration more difficult to resolve. For the time-span contributing to the antenna calibration, there are three instances where the nominal yaw attitude is flipped 180 degrees for a few days. The high-rate data combined with the yaw-flip maneuvers allow for better resolution of the low elevation portion of the antenna calibration in the nominal flight direction (azimuth = 0°).

#### 7.3.1.2 GPS IIIA Antenna Calibration Extension

With the Sentinel-6 MF receiver antenna calibration established based on the Block II calibrations, we are able to compute a GPS IIIA transmitter extension consistent with the Block II IGS14 antenna calibrations. From each daily Block II derived dynamic orbit solution during 2021, GPS IIIA residuals from five transmitters (SVNs 74-78) are fit and then stacked by boresight angle. Days with orbit maintenance maneuvers are excluded. Figure 7.3 shows the stacked residuals with a bin size of 0.25 degrees from post-fit measurement residuals and the right panel shows the number of residuals in each bin. The GPS IIIA observations contribute 13.2% of the total number of ob-

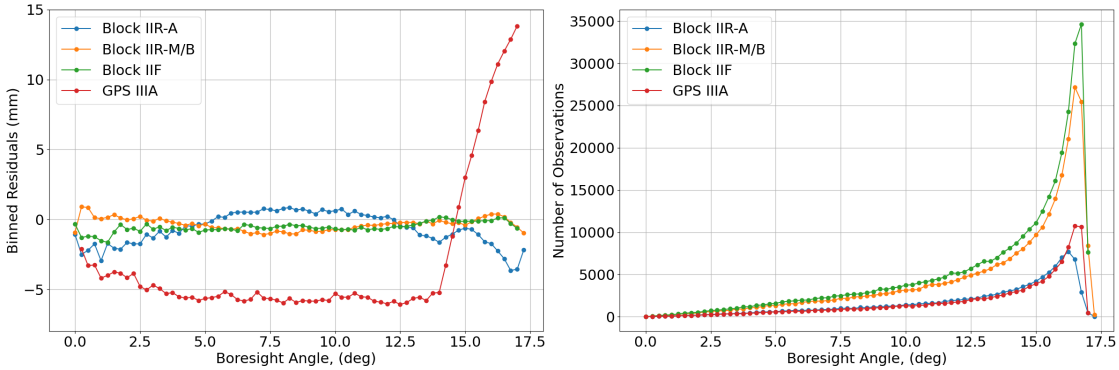


Figure 7.3: Mean binned residuals relative to Block II-only orbit solutions (left) and the total number of observations in each bin (right) for Block IIR-A (blue), IIR-M/B (orange), IIF (green), and IIIA (red)

servations over all boresight angles, with more than half of these GPS IIIA observations occurring above 14 degree boresight angles. An improved antenna calibration above 14 degrees is therefore important to the GPS IIIA measurement model. In contrast, the Block II stacked residuals do not indicate significant deficiencies. We use the mean stacked residuals from the 0.25 degree bins to derive GPS IIIA extension at boresight angles of 15, 16, and 17 degrees as shown in Table 7.1. The resulting GPS IIIA extension after convergence is shown in Figure 7.4.

We note also that our estimated extension of the GPS IIIA PVs is very similar to that of the

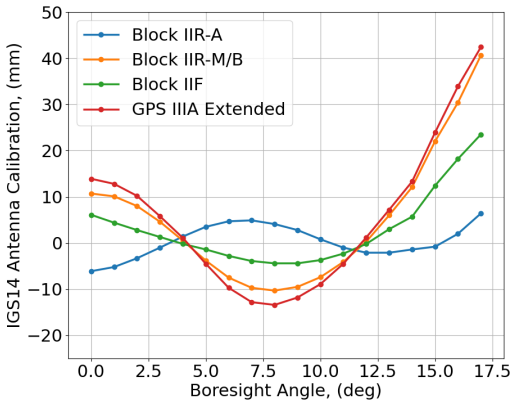


Figure 7.4: GPS IIIA extended PV (red) as a function of boresight angle compared to existing IGS14 Block IIR-A (blue), IIR-M/B (orange), and IIF (green) PVs

Table 7.1: Estimated GPS IIIA antenna calibration extension values

| boresight angle | 14 degrees | 15 degrees | 16 degrees | 17 degrees |
|---|---|---|---|---|
| calibration value | 13.3 mm | 23.9 mm | 33.9 mm | 42.4 mm |

Block IIR-M constellation from IGS14. Using that extension is a potential alternative to the values we propose in Table 7.1. The two platforms are both manufactured by Lockheed Martin which may explain some of the similarity. Additionally, Steigenberger et al. (2020) found agreement in other aspects of the two platforms such as the attitude profile and dimensions.

### 7.3.2 Orbit Quality Comparison

#### 7.3.2.1 Sentinel-6 MF Internal Metrics

The daily post-fit phase residual rms is an indicator of the goodness-of-fit of the orbit solution and will be impacted by how well the receiving and transmitting antennas are modeled. Figure 7.5 shows the histogram of daily rms of post-fit phase residuals from daily 30-hour reduced-dynamic

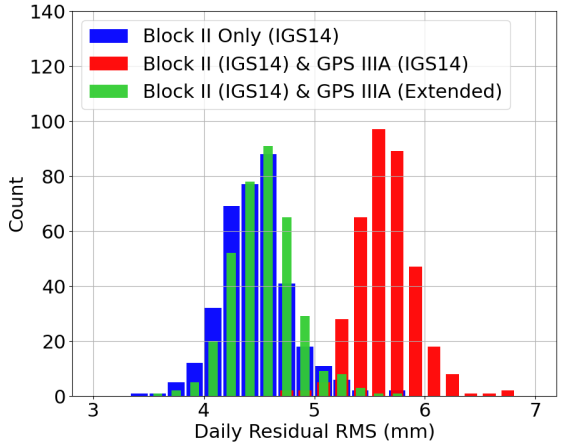


Figure 7.5: Post-fit phase residual rms from Sentinel-6 MF ambiguity-resolved reduced dynamic orbit solutions for three cases: 1) Block II tracking data alone (blue), 2) Block II and IIIA tracking data with IGS14 antenna calibrations (red), 3) Same as case (2) but using GPS IIIA PV extension (green)

Table 7.2: Sentinel-6 MF post-fit residual rms in terms of the mean ± the standard deviation of the daily statistics

| | LC (mm) | LC GPS IIIA Only (mm) | PC (mm) |
|---|---|---|---|
| Block II Only | 4.5 ± 0.32 | - | 620 ± 60 |
| Block II and IIIA IGS14 | 5.6 ± 0.27 | 9.7 ± 0.45 | 610 ± 110 |
| Block II and IIIA Extended | 4.5 ± 0.30 | 4.5 ± 0.52 | 610 ± 100 |

POD solutions from the entirety of 2021. As expected, our GPS IIIA antenna calibration extensions clearly provide a better fit to the data. Most notably, the post-fit rms of residuals from POD solutions using both Block II and IIIA tracking data fall in-line with solutions using only Block II tracking data. Meanwhile post-fit residuals from POD solutions using Block II and IIIA tracking data with the IGS14 antenna calibrations are larger by 20% as shown in Table 7.2. Looking only at the GPS IIIA data shows a more than 50% reduction in the post-fit residual rms when using our GPS IIIA extension.

From daily 30-hour ambiguity resolved orbit solutions, there are six hours of overlap. Here we difference the central four hours to compute a daily radial, cross-track, and in-track component rms

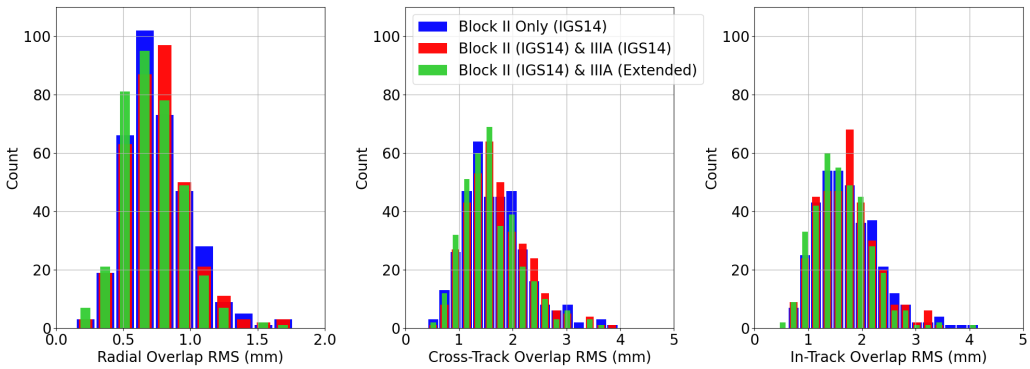


Figure 7.6: Daily overlap difference rms for radial (left), cross-track (middle), and in-track (right) from Sentinel-6 MF ambiguity-resolved reduced dynamic orbit solutions for three cases: 1) Block II tracking data alone (blue), 2) Block II and IIIA tracking data with IGS14 antenna calibrations (red), 3) Same as case 2 but using GPS IIIA PV extension (green)

Table 7.3: Sentinel-6 MF overlap difference rms in terms of the mean ± the standard deviation of the daily statistics

| | Radial Overlap (mm) | Cross-track (mm) | In-track (mm) |
|---|---|---|---|
| Block II Only | 0.78 ± 0.33 | 1.7 ± 0.57 | 1.8 ± 1.0 |
| Block II and IIIA IGS14 | 0.77 ± 0.31 | 1.7 ± 0.56 | 1.8 ± 0.90 |
| Block II and IIIA Extended | 0.73 ± 0.28 | 1.6 ± 0.54 | 1.7 ± 0.83 |

statistics. The resulting rms values are a measure of the orbit solution precision and consistency. Daily rms values that are more than 5 standard deviations away from the overall mean value are removed. Figure 7.6 shows a histogram of the daily overlap statistics for each orbital component. Computing the mean and standard deviation of all daily overlap difference rms statistics produces a summary of the the overall precision and consistency of the solutions. Table 7.3 lists the mean values and standard deviation for all three components. The orbit solutions that incorporate the GPS IIIA measurements with the extrapolated antenna calibration have superior precision with slightly improved overlap statistics for all three components, in both the mean and standard deviation of daily values. Of course, the GPS constellation currently only includes 5 GPS IIIA satellites, and we would expect higher impact as that number continues to increase. Given that the orbit overlaps are a measure on solution precision, we would expect the reduced dynamic approach to produce similar results. The improvement when including GPS IIIA measurements is due in part to the increased number of measurements, as compared to when they are excluded.

#### 7.3.2.2 Ambiguity Resolution

Each of the daily reduced dynamic POD solutions includes an ambiguity resolution summary. Fixed phase ambiguity biases are applied within the filter smoother using a soft constraint with a confidence level of 10 cm and the solution is iterated 10 times. Figure 7.7 shows the distribution of passes with narrow-lanes constrained to less than 10 centi-cycles of an integer (left). The Block II only orbit solutions have a median of 84.5 percent of narrow-lane passes constrained to less than 10 centi-cycles while the inclusion of the GPS IIIA with the IGS14 antenna calibrations reduces the

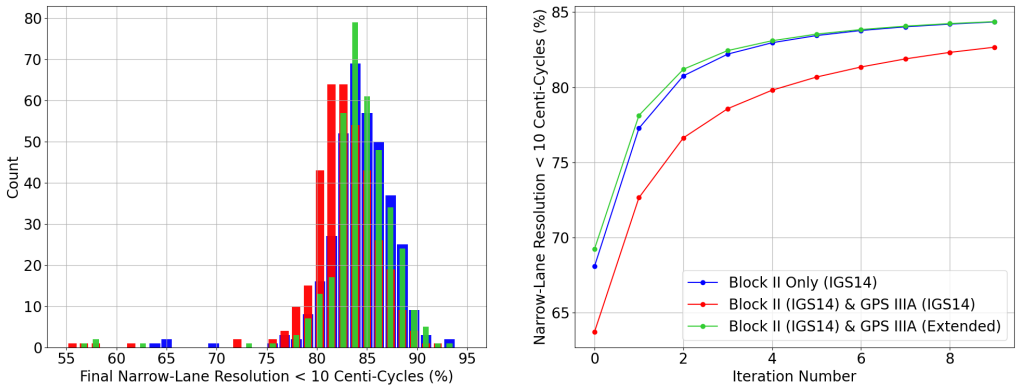


Figure 7.7: Final iteration of daily narrow-lane ambiguity resolution histogram (left) and overall mean narrow-lane resolution after each iteration (right) as a percent of passes constrained to less than 10 centi-cycles from Sentinel-6 MF ambiguity-resolved reduced-dynamic orbit solutions for three cases: 1) Block II tracking data alone (blue), 2) Block II and IIIA tracking data with IGS14 antenna calibrations (red), 3) Same as case (2) but using GPS IIIA PV extension (green)

median to 82.7 percent. Using the extended GPS IIIA antenna calibration brings the median back to 84.5 percent of passes constrained to less than 10 centi-cycles. Here we see that by extending the GPS IIIA IGS14 antenna calibration the ambiguity resolution improves and is consistent with the Block II only results. This is also consistent with the results in Figure 7.7 (right) where the extended GPS IIIA antenna calibration shows similar performance to the Block II only results after each iteration.

#### 7.3.2.3 External Metrics

To evaluate the orbit accuracy, we consider independent SLR measurements (Pearlman et al., 2019). Only SLR stations with biases below 5 mm for the entire data set are used to evaluate orbit accuracy. These include a total of eight stations: Greenbelt, Maryland; Graz, Austria; Herstmonceux, United Kingdom; Hartebeesthoek, South Africa; Mt Stromlo, Australia; Yarragadee, Australia; Wettzell, Germany; and Zimmerwald, Switzerland. Figure 7.8 shows the SLR residual rms, left panel, and overall bias, right panel, from all SLR measurements across 2021 as a function of boresight angle relative to the SLR frame. Here we can see that all three orbit solutions are

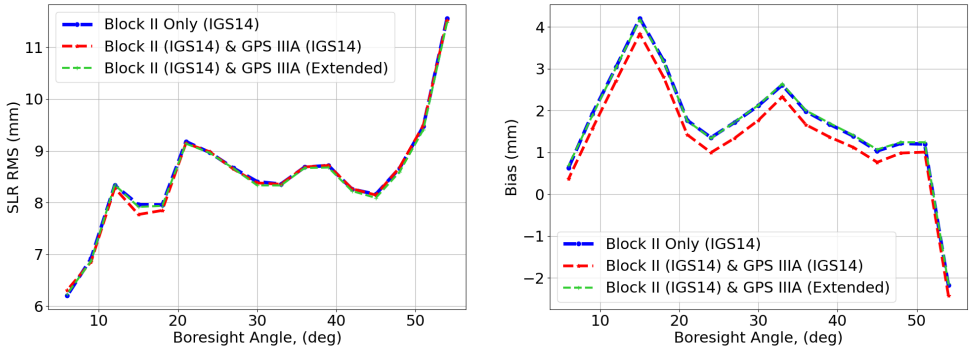


Figure 7.8: SLR residual rms (left) and bias (right) as a function of boresight angle

relatively similar. Overall rms values are 8.9 mm for Block II only, 8.9 mm including GPS IIIA with IGS14 antenna calibrations, and 8.8 mm including GPS IIIA with extended antenna calibration. The consistency in the SLR residual rms values between all three solutions is likely due to the strength of the ambiguity resolution of the Block II measurements which contribute more than 85 percent of the total measurements. It is reasonable to conclude that as the number of GPS IIIA satellites increase, the orbit accuracy will be degraded without extension of the GPS IIIA calibration.

Looking at the SLR residual bias as a function of boresight angle shows a shift of about 0.3 mm when using the GPS IIIA measurements with IGS14 antenna calibrations. Incorporating the GPS IIIA measurements with the extended antenna calibration produces SLR biases that are essentially consistent with the Block II only solutions. Table 7.4 shows a comparison of the overall statistics from each set of orbit solutions.

Table 7.4: Comparison of the overall rms, mean, and standard deviation of the SLR residuals

| | rms (mm) | mean (mm) | std (mm) |
|---|---|---|---|
| Block II Only | 8.9 | 1.26 | 8.8 |
| Block II and IIIA IGS14 | 8.9 | 0.99 | 8.8 |
| Block II and IIIA Extended | 8.8 | 1.28 | 8.7 |

## 7.4 Independent Validation with Jason-3

The GPS IIIA extensions are further validated using Jason-3 by applying the same three scenarios as those above with Sentinel-6: a Block II only solution, a Block II and IIIA solution using IGS14 antenna calibrations for both, and finally, a Block II and IIIA solution with extended GPS IIIA calibration. Worth noting is that the Jason-3 GPS antenna is tilted 15 degrees away from zenith while the Sentinel-6 GPS antenna points towards zenith. This geometry, combined with a yaw-steering attitude profile, changes the correlation between the receiver and transmitters, particularly in the spacecraft z-direction. As such, Jason-3 provides a useful validation of the consistency of the GPS IIIA PV extension given that it has different lines of sight to the GPS constellation. These solutions are processed over the same time frame as the previous Sentinel-6 MF results, 2021-01-01 to 2021-12-31. Like Sentinel-6 MF, the Jason-3 receiver antenna calibration is generated from Block II only measurements although from a longer time frame covering from 2016-02-13 to 2020-09-12.

### 7.4.1 Jason-3 Internal Metrics

The Jason-3 daily L1/L2 dual-frequency phase post-fit residual rms is shown in Figure 7.9 and the mean ± the standard deviation is listed in Table 7.5. Here the results show a pattern that matches what was observed in Sentinel-6 MF, where the POD solutions using both Block II and IIIA tracking data are more in line with Block II-only solutions when the extended calibrations for the GPS IIIA transmitters are applied.

Table 7.5: Jason-3 post-fit residual rms in terms of the mean ± the standard deviation of the daily statistics

| | LC (mm) | LC GPS IIIA Only (mm) | PC (mm) |
|---|---|---|---|
| Block II Only | 4.4 ± 0.25 | - | 380 ± 30 |
| Block II and IIIA IGS14 | 5.6 ± 0.38 | 9.3 ± 1.0 | 390 ± 30 |
| Block II and IIIA Extended | 4.5 ± 0.24 | 4.6 ± 0.40 | 390 ± 30 |

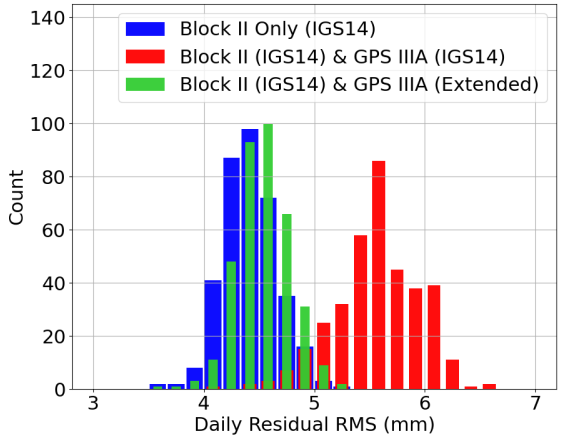


Figure 7.9: Post-fit phase residual rms from Jason-3 ambiguity-resolved reduced dynamic orbit solutions for three cases: 1) Block II tracking data alone (blue), 2) Block II and IIIA tracking data with IGS14 antenna calibrations (red), 3) Same as case (2) but using GPS IIIA PV extension (green)

Comparing the daily central four hours of overlap differences for radial, cross-track, and in-track components, we observe a similar pattern to the Sentinel-6 MF overlap statistics. As with Sentinel-6 MF, outliers 5 standard deviations from the mean are removed. Figure 7.10 shows the

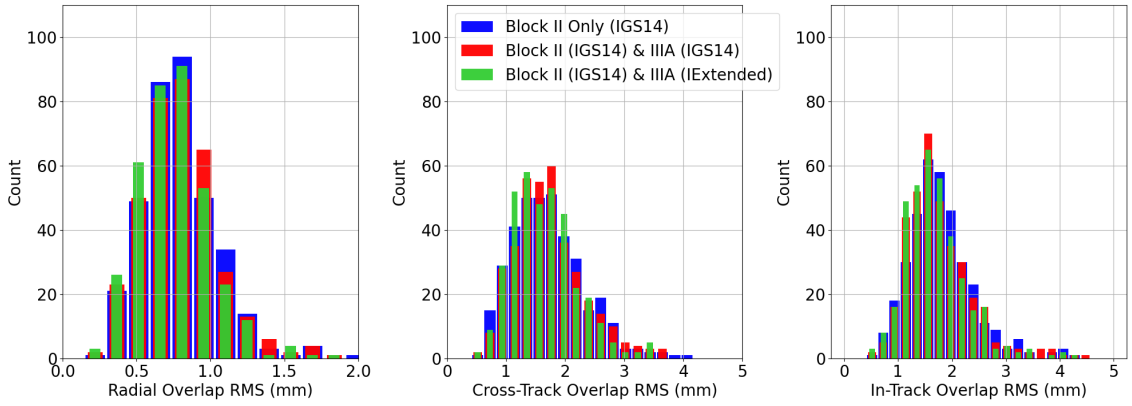


Figure 7.10: Jason-3 Daily overlap rms for radial (left), cross-track (middle), and in-track (right) from Jason-3 ambiguity-resolved reduced dynamic orbit solutions for three cases: 1) Block II tracking data alone (blue), 2) Block II and IIIA tracking data with IGS14 antenna calibrations (red), 3) Same as case (2) but using GPS IIIA PV extension (green)

Table 7.6: Jason-3 overlap difference rms in terms of the mean ± the standard deviation of the daily statistics

| | Radial Overlap (mm) | Cross-track (mm) | In-track (mm) |
|---|---|---|---|
| Block II Only | 0.80 ± 0.29 | 1.7 ± 0.61 | 1.8 ± 0.72 |
| Block II and IIIA IGS14 | 0.79 ± 0.26 | 1.7 ± 0.58 | 1.8 ± 0.62 |
| Block II and IIIA Extended | 0.76 ± 0.26 | 1.7 ± 0.55 | 1.7 ± 0.62 |

daily overlap statistics for all three solutions. Table 7.6 lists the mean values ± the standard deviation for all daily overlap values. While the overall improvements to the mean values are relatively small when using the extended GPS IIIA calibration, it does represent an improvement to the POD solution. The improvement to the standard deviations suggests a better day-to-day consistency, particularly for the in-track component.

### 7.4.2 Jason-3 Ambiguity Resolution

Once again, the daily narrow-lane ambiguity resolution statistics for Jason-3 show a similar pattern when compared to the Sentinel-6 MF ambiguity resolution. Figure 7.11 shows the statistics of the daily ambiguity resolution after iteration (left) across all of 2021 and the mean ambiguity

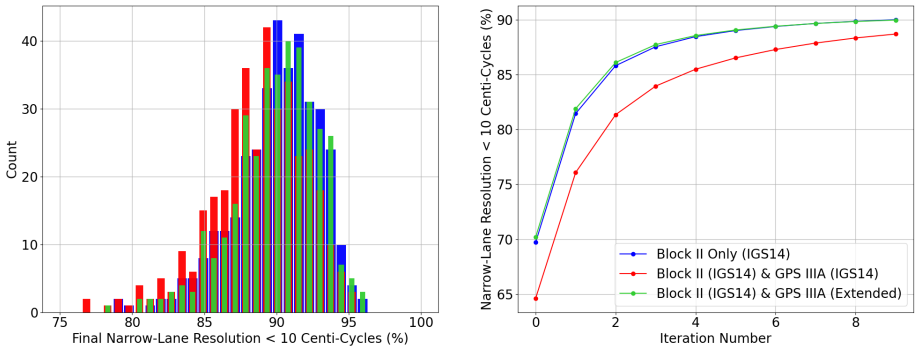


Figure 7.11: Final iteration of daily narrow-lane ambiguity resolution histogram (left) and overall mean narrow-lane resolution after each iteration (right) as a percent of passes constrained to less than 10 centi-cycles from Jason-3 ambiguity-resolved reduced dynamic orbit solutions for three cases: 1) Block II tracking data alone (blue), 2) Block II and IIIA tracking data with IGS14 antenna calibrations (red), 3) Same as case (2) but using GPS IIIA PV extension (green)

resolution after each iteration (right). The median value of narrow-lane passes that are fixed to less than 10 centi-cycles is 90.3 percent for the Block II only orbit solutions, 89.0 when including GPS IIIA with IGS14 calibration, and 90.4 percent when including GPS IIIA with our extended calibration. Here the ambiguity resolution with the extended GPS IIIA antenna calibrations is consistent with the Block II only results. The extended GPS IIIA antenna calibration is also consistent with the Block II only results after each iteration as seen in Figure 7.11 (right).

### 7.4.3 GPS Transmitter Calibrations

To evaluate the overall consistency of the transmitter antenna calibrations, residuals are stacked by boresight angle and separated into sub-block types for all of 2021. Figure 7.12 shows the mean residual value for both Sentinel-6 MF (left) and Jason-3 (right) as a function of transmitter boresight angle from the reduced dynamic and ambiguity resolved solutions with the GPS IIIA antenna calibration extension. The GPS IIIA satellite stacked residuals are generally quite

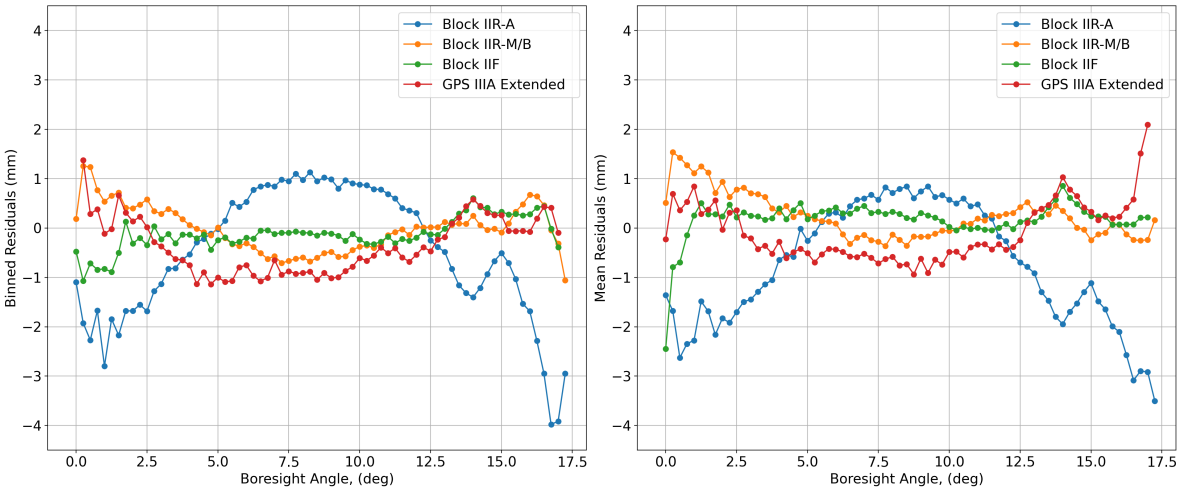


Figure 7.12: Comparison of stacked block residuals by transmitter boresight angle for Sentinel-6 MF (left) and Jason-3 (right)

consistent between the Jason-3 and Sentinel-6 MF solutions across all boresight angles less than 17 degrees, despite being processed completely independently of each other, and each with their own receiver antenna calibrations. There are differences on the order of 1-2 mm at boresight angles

higher than 17 degrees. These results suggest that improvements on the order of 1-2 mm to the IGS14 PVs at all boresight angles for all blocks could be possible. The poorer performance of the IIR-A residuals may be due to the IGS14 antenna calibration estimate being relative to a group of satellites that have now been partially phased out of operation, showing a potential weakness in applying combined PVs to an entire transmitter sub-block.

### 7.4.4 Manufacturer Published PVs for GPS IIIA

A recent public release of measured antenna patterns for the first five GPS IIIA satellites (Fischer, 2022), provides an opportunity for comparison with the extended GPS IIIA IGS14 PVs derived in this work. The data set, which includes phase measurements across azimuth and boresight angles for each operational frequency (L1, L2, and L5), was collected prior to antenna installation on the spacecraft. To compare against the GPS IIIA IGS14 PVs, phase values are converted to length and averaged across azimuth. The individual L1 and L2 patterns are then combined in the same way as the ionosphere-free observables.

Different standards for representing the PCO can confound the comparisons, so we adjust the manufacturer PVs to be consistent with the IGS14 PCOs:

$$PV = PV_{PCO-Manufacturer} - PV_{PCO-IGS14} + PV_{Manufacturer} \tag{7.1}$$

where the phase variations due to the PCO ($PV_{PCO}$) are computed by projecting the offset onto the line-of-sight direction, $\mathbf{e}$, using

$$PV_{PCO} = \mathbf{r} \cdot \mathbf{e} = x_{PCO}cos(el)cos(az) + y_{PCO}cos(el)sin(az) + z_{PCO}sin(el) \tag{7.2}$$

For azimuth averaged PVs, only the z-offset is retained, simplifying to

$$PV_{PCO} = z_{PCO}sin(el) \tag{7.3}$$

Figure 7.13 (left) shows the comparison of the GPS IIIA IGS14 PVs including our extension

to the average PVs based on the published values. To aid in the comparison of the overall shape, the published PVs are shifted to align the 0 degree boresight value with the IGS14 value.

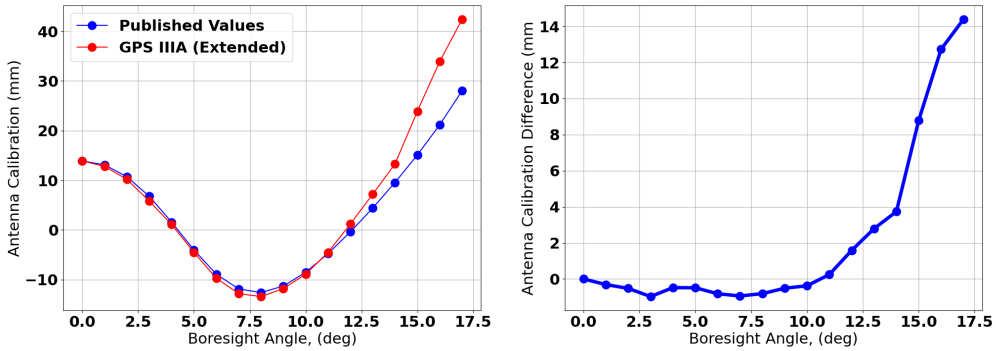


Figure 7.13: Comparison of the average GPS IIIA manufacturer published phase variations to the extended IGS14 values (left) and the difference between them (right)

Figure 7.13 (right) shows the difference between the ground-measured and extended IGS14 phase calibrations. In light of the different techniques used to establish these estimates, the general agreement of the patterns to within 4 mm below 14 deg boresight, and 15 mm overall, is quite encouraging. Two candidate explanations for the remaining differences are spacecraft multipath effects, which are unaccounted for in the manufacturer's antenna measurements, and the consistency constraints imposed on the IGS14 antenna calibrations. The ability to detect and correct for spacecraft multipath is clearly an important benefit of using in-flight calibrations. Transmitter calibration differences due to the reference frame constraint are less critical, because they will have very little effect on POD when combined with in-flight receiving antenna calibrations that compensate for these systematic effects (Jäggi et al., 2010).

It is quite interesting to note, however, that the measured PVs are smooth across the 14 degree transition, whereas the extended GPS IIIA calibration has a noticeable shift in the slope before and after 14 degrees. This feature is not unique to our solution but is also evident in the IGS14 Block IIR-M/B and IIF PVs. Given that our extension has been developed to be consistent with the Block II extensions, this discrepancy may highlight a potential deficiency in the IGS14 PVs which is potentially a result of the the Block IIAs being used as the baseline for later Block II

satellite extensions (Schmid et al., 2016). Thus, future work to develop calibrations referenced to the manufacturer-provided GPS IIIA antenna patterns seems like a promising approach for further improvements in GPS performance.

## 7.5 Summary

The work presented demonstrates an effective extension of the IGS14 GPS IIIA PVs above 14 degree boresight angles and the resulting improvements to the orbit determination solutions for both Sentinel-6 MF and Jason-3. We provide a model for the GPS IIIA PVs for boresight angles greater than 14 degrees, using an approach that makes them consistent with the IGS14 Block II PVs. Use of this GPS IIIA PV extension, determined from only Sentinel-6 tracking data, results in better consistency between orbit solutions determined from Block II-only tracking data and those including both Block II and III. Most metrics improve when using the combination of Block II and IIIA tracking data together with our GPS IIIA PV extension. POD solutions for low-Earth orbiters will likely be degraded without a more reliable antenna calibration for GPS IIIA satellites, with the impact continuing to grow as the number of GPS IIIA satellites increases. Our estimates for the GPS IIIA PVs for boresight angles greater than 14 degrees remove this potential degradation. Additionally, the correlated residuals between Sentinel-6 MF and Jason-3 suggest that the IGS14 antenna calibrations could be improved across all sub-block types. Given the performance and low multipath properties of the Sentinel-6 MF TriG receiver, it presents the possibility for use as a reference calibration for estimation of the entire GPS transmitter antenna calibration separate from a predetermined reference frame. An approach similar to that performed by Haines et al. (2015) could provide additional insight for improvement of the transmitter calibrations.

The current form of the IGS2020 transmitter calibrations have adjusted the PCOs of all GPS transmitters to the IGS realization of the ITRF2020 while continuing to use the PVs from the IGS14 transmitter calibrations. Similarly, the GPS IIIA PV extensions from this work, relative to the IGS14 Block II transmitters, could also be applied to the IGS2020 transmitter calibrations. Additionally, with the release of the manufacturer published PVs for GPS IIIA, it is possible to

recalibrate the Block II PVs against the the GPS IIIA. This has the potential to remove the large z-offsets observed in the TriG in-flight receiver calibration.

# Chapter 8

# An evaluation of a combined TriG and PODRIX POD solution

## 8.1 Introduction

Sentinel-6 MF is the first LEO satellite to fly two fully independent geodetic GNSS receivers with the PODRIX (redundant pair) tracking GPS and Galileo signals and the TriG tracking GPS. This unique configuration presents an opportunity to study and compare a multi-receiver, multi-GNSS constellation POD solution. The performance of the combined solution can be compared and contrasted with the performance of each receiver alone and between the GPS and Galileo constellations. The configuration of Sentinel-6 MF acts an orbiting geodetic observatory, linking three separate tracking systems in GPS, Galileo, and SLR. As described by Haines et al. (2015), having a single space platform with multiple geodetic tracking systems could enable better realizations of the terrestrial reference frame along with improved gravity recovery. While the primary goal of this study is to understand and compare the POD associated with the TriG and PODRIX, it is important to highlight the additional benefits that Sentinel-6 MF could provide for geodetic science.

Montenbruck et al. (2021) first demonstrated highly accurate POD solutions for Sentinel-6 MF with a consistency of 1 cm based on the PODRIX observations alone. Additional PODRIX derived solutions were described by Peter et al. (2022) and Zandbergen et al. (2022) where it was found that the Galileo solutions performed better than the GPS solutions, but when combined, the two performed better than either alone. The better Galileo performance is due to lower residual rms and higher ambiguity fixing statistics. Jin et al. (2023) demonstrated the ability to estimate the Sentinel-6 MF attitude using observations from both receivers. Applying the estimated attitude

improved the orbit solutions when compared to solutions based on the nominal attitude. However, they did not present results using the as-measured quaternions.

TriG based POD solutions were presented as part of the studies described in Chapters 6 and 7, where solutions with radial orbit accuracies better than 1 cm were inferred from SLR residuals. Even though highly accurate POD solutions for both the TriG and PODRIX have already been demonstrated, the goal of this study is to estimate orbit solutions using all observations from both the PODRIX and TriG receivers. As part of this work, initial comparisons between separate TriG and PODRIX solutions revealed a discrepancy in the in-track position of approximately 10 mm. A similar bias was also observed in baseline estimates between the TriG and PODRIX antennas by Montenbruck et al. (2022) and Desai et al. (2022). Based on SLR residuals, this bias has been isolated to an inconsistency between the estimated receiver clock bias and time-tag in the TriG observations. To correct for this, the TriG observations are calibrated through the application of a 405 m range bias, which is equivalent to a 1.35 $\mu$s time-tag error.

Section 8.2 compares the two receivers and tracking modes and provides an overview of the available data. This is followed by a brief description of the methods for antenna calibration estimation and POD processing strategy. Next, section 8.3 provides a description of the observed in-track bias between the TriG and PODRIX, and the calibration of the TriG observations to resolve it. Section 8.4 provides an overview of the results for six solutions; TriG only, TriG only with 10 degree elevation mask, PODRIX GPS only, PODRIX Galileo only, PODRIX GPS plus Galileo (referred to as PODRIX from here on), and TriG plus PODRIX (referred to as combined from here on). First, the mean offsets absorbed by the estimated antenna PV corrections are compared across the different solutions. As in the prior chapters, the results include a presentation of the internal metrics consisting of post-fit residual rms, orbit overlaps, and ambiguity resolution performance. Finally, the orbit accuracy of each solution is evaluated through the use of independent SLR measurements which are withheld from the POD solutions.

## 8.2 Methods

### 8.2.1 Sentinel-6 MF Instrumentation

The primary Sentinel-6 MF GNSS POD instrument is a redundant pair of multi-GNSS (GPS and Galileo) PODRIX receivers from RUAG, capable of tracking up to a combined total of 18 GPS and Galileo satellites (Montenbruck et al., 2021; Peter et al., 2022). A secondary NASA JPL TriG receiver with support for radio occultation measurements also provides POD quality GPS observations, tracking up to 12 satellites (Tien et al., 2010, 2012). The TriG does not enforce any limitations on tracking based on elevation, but the PODRIX employs a 10 degree receiver elevation mask. Table 8.1 shows the various signals available on Sentinel-6 MF and their corresponding RINEX 3.0 (receiver independent exchange format-version 3.0) observation codes (Gurtner and Estey, 2007). The current PODRIX tracking configuration includes a mix of legacy and modern GPS observations on L1 and L2 along with those from Galileo on L1 and L5. With this extensive measurement set, Sentinel-6 MF facilitates the comparison of solutions using newer signals against the legacy observations which have an extensive well-established record for POD.

In this study, we use the RINEX 3.0 three digit nomenclature to define the observations. The

Table 8.1: GNSS observation types available on Sentinel-6 MF. TriG observations are derived from P(Y) (along with C/A on L1) tracking while the PODRIX tracks P(Y) on Block IIR satellites and C/A and L2C for Blocks IIR-M, IIF, and GPS IIIA

| Receiver | GNSS | Frequency Band | PRN Code Type | Pseudorange Observation Code | Carrier Phase Observation Code |
|---|---|---|---|---|---|
| TriG | GPS | L1/1575.42 MHz | C/A | C1C | L1C |
| | | L1/1575.42 MHz | P(Y) | C1W | L1W |
| | | L2/1227.60 MHz | P(Y) | C2W | L2W |
| PODRIX | GPS | L1/1575.42 MHz | C/A | C1C | L1C |
| | | L1/1575.42 MHz | P(Y) | C1W | L1W |
| | | L2/1227.60 MHz | L2C (L) | C2L | L2L |
| | | L2/1227.60 MHz | P(Y) | C2W | L2W |
| PODRIX | Galileo | E1/1575.42 MHz | C | C1C | L1C |
| | | E5a/1176.45 MHz | Q | C5Q | L5Q |

first letter defines the observations type (C for pseudorange, L for phase), the second is the frequency band (L1, L2, L5), and third the observation type (e.g. C for C/A, W for P(Y), and L for L2C). The TriG tracks GPS C1C/C1W/C2W pseudorange along with L1C/L1W/L2W carrier signals. The PODRIX tracks both GPS and Galileo signals. For GPS, the C1C/C1W/C2W pseudorange and L1C/L1W/L2W carrier phase are tracked for the Block IIR satellites, but switches to C1C/C2L pseudorange, and L1C/L2L carrier phase for Blocks IIR-M, IIF, and GPS IIIA satellites which transmit the modernized L2L signal. For Galileo signals, the C1C/C5Q pseudorange and L1C/L5Q phase signals are tracked.

The JPL orbit, clock, and wide-lane products (Dietrich et al., 2018) are estimated using the 1W/2W observations for GPS and 1C/5Q for Galileo. The TriG tracks the C1W/C2W pseudorange signals which are consistent with the clock product, so no corrections based on observation type are necessary. The same is true for the PODRIX-Galileo observations which track the C1C/C5Q pseudorange signals. On the other hand, the PODRIX 1C/2L measurements must be corrected for differential code biases (DCB) that exist between the different pseudorange signals. DCBs are the result of hardware delays between different codes and can occur on both transmitters and receivers. Uncorrected DCBs degrade the wide-lane ambiguity resolution, which is the first step for single receiver ambiguity resolution (Bertiger et al., 2010b). Before processing, several corrections have been applied to the PODRIX RINEX files. The first is a calibration by the manufacturer of temperature dependent pseudorange corrections which account for receiver based biases between C1C-C1W and C2L-C2W pseudorange observations. As estimated by Montenbruck et al. (2021), an additional empirical correction to the L2L phase measurement of 0.075 cycles, plus the expected 0.25 cycle offset between L2L and L1W, is also applied.

### 8.2.2 Differential Code Bias Correction

Because a subset of the PODRIX GPS signals observe the C1W/C2W pseudoranges, which are consistent with the wide-lane bias product, they can serve as a reference against which the remaining C1C-C1W and C2L-C2W biases can be estimated. This was done by first fixing TriG

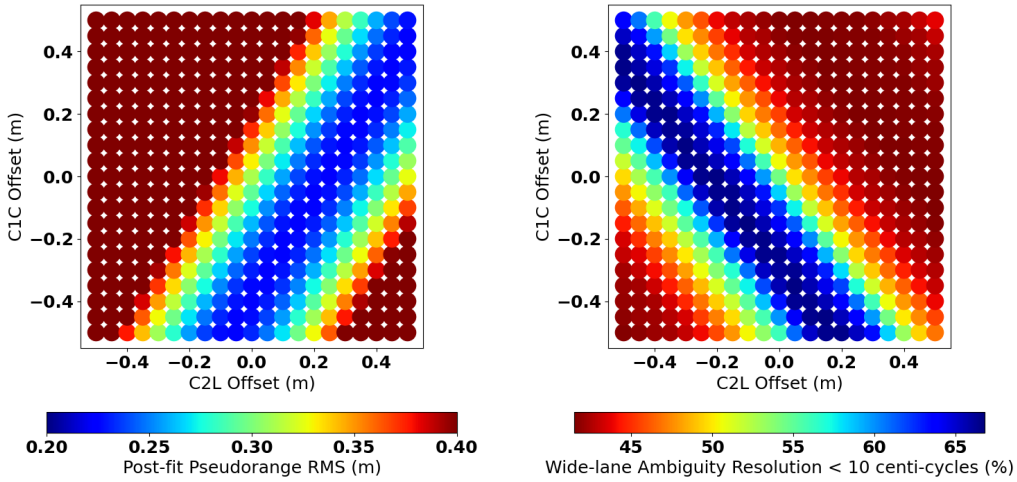


Figure 8.1: Post-fit pseudorange rms (left) and wide-lane ambiguity resolution (right) as a function of percentage of samples fixed to within 10 centi-cycles of an integer for a given C1C and C2L offset

based orbit solutions. Then, a bias was applied to the C1C and C2L observations across a range of ±0.5 m in 0.05 m steps. For each combination of C1C and C2L biases, the C1W/C2W observations along with a single C2L transmitter were fit to the fixed orbit solutions estimating only the receiver clock, phase biases, and produced wide-lane resolution statistics. Finally, the C1C and C2L bias values were chosen based on the the combinations of highest percent wide-lane ambiguity resolution and the lowest post-fit pseudorange residual rms. This was done for all L2C transmitters for two separate days, 2021-06-30 and 2022-05-29, and the average bias from these two days was applied to all observations across the examined time span. Figure 8.1 shows the results for SVN-50 from 2021-06-30. Applying these biases greatly improves the overall wide-lane ambiguity resolution.

### 8.2.3 Data Overview

TriG pseudorange and phase observations are downlinked at 1 Hz. The PODRIX phase observations are also sent at 1 Hz, but the code observations are only sent once per 10 seconds. Prior to orbit estimation, raw measurements are processed in the GipsyX GNSS data editor where they are screened for outliers and phase breaks are flagged. Continuous phase arcs shorter than

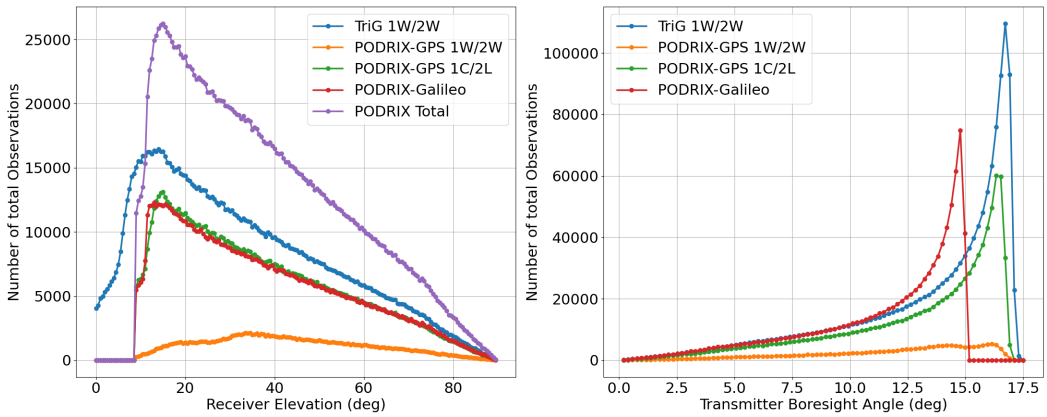


Figure 8.2: Number of observations from 2021-06-30 to 2022-12-31 as a function of receiver elevation (left) and transmitter boresight (right) for TriG 1W/2W (blue), PODRIX-GPS 1W/2W (orange), PODRIX-GPS 1C/2L (green), and PODRIX-Galileo 1C/5Q (red). The left panel also shows the total PODRIX observations (purple)

10-minutes are discarded. The remaining observations are decimated to a 5-minute data rate along with carrier smoothing of the pseudorange. Figure 8.2 shows the number of observations available as a function of receiver line-of-sight elevation for all observations across an 18 month time span from 2021-06-30 to 2022-12-31. Of the total combined TriG and PODRIX observations, the TriG contributes 40.5% and the PODRIX 59.5%. For the PODRIX observations, 8.7% are GPS C1W/C2W, 46.1% GPS C1C/C2L, and 45.2% Galileo. In the receiver frame, approximately 35% of TriG observations are below 20 degrees elevation, while fewer than 24% of PODRIX observations are below this threshold due to the 10 degree elevation mask. In the transmitter frame, more than half of all TriG observations occur at boresight angles between 14 and 17 degrees. The PODRIX-Galileo on the other hand has only about 30% of observations above 14 degrees with a maximum of 15 degrees. This is due not only to the 10 degree mask, but also the higher altitude of the Galileo constellation.

Figure 8.3 shows the percentage of epochs with a given number of tracked satellites. The median tracked is 9 for the TriG, 1 for the PODRIX-GPS C1W/C2W, 6 for PODRIX-GPS C1C/C2L, and 6 for PODRIX-Galileo resulting in a combined total of 13. The TriG tracks eight satellites or

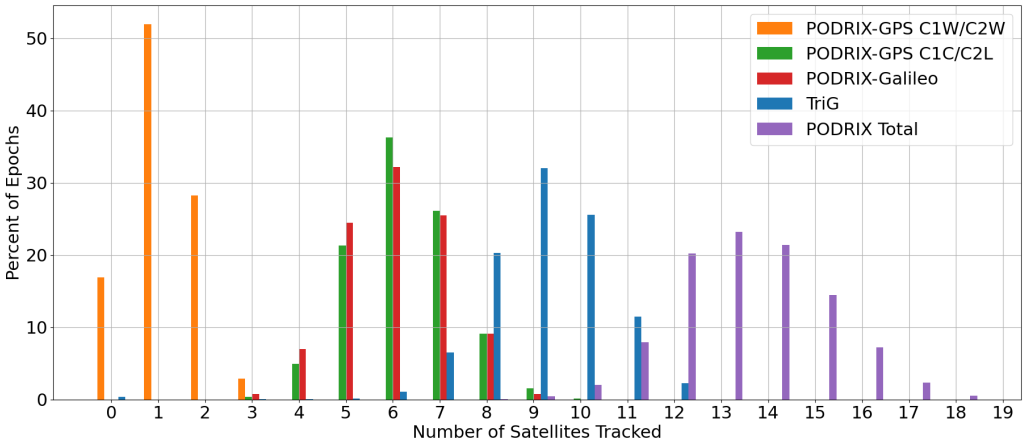


Figure 8.3: Number of satellites tracked at each epoch from 2021-06-30 to 2022-12-31 for PODRIX-GPS 1W/2W (orange), PODRIX-GPS 1C/2L (green), PODRIX-Galileo 1C/5Q (red), TriG 1W/2W (blue), ant total PODRIX (purple)

more 91.7% of the time, while the PODRIX tracks eight or more observations 99.0% of the time. By combining the GPS and Galileo constellations, the PODRIX increases the median tracking by 4 transmitters more than the TriG despite its 10 degree elevation mask. In terms of the number of measurements possible, the multi-constellation tracking provides a clear advantage.

### 8.2.4 Receiver Antenna Calibrations

Like the previous studies, the receiver antenna calibration is estimated from daily solutions generated from 24-hour dynamic orbit estimates. This process is described in more detail in Chapter 3 with the estimation strategy shown in Table 3.1. The main difference from the previous studies is that instead of a single system (TriG), there are now two independent receivers, TriG and PODRIX. Also, even though the PODRIX-GPS and PODRIX-Galileo observations share an antenna, they require separate calibrations due to the different observation frequencies as well as the dependence on the IGS14 transmitter calibrations. This results in a total of three antenna calibrations.

For each orbit solution, antenna calibrations for both the code and the phase are estimated in a manner that is consistent with the receiver observations under study. For example, the TriG POD

solutions use an antenna calibration that is estimated using only TriG observations, whereas for the combined antenna calibration, the TriG, PODRIX-GPS, and PODRIX-Galileo corrections to the pre-launch calibrations are simultaneously estimated together in a single solution. Constraints are constructed from the antenna calibration vertices for the x-offset using the methods described in Section 5.5. When multiple calibrations are being estimated together, the x-offset constraint is applied to only one antenna calibration. This allows for any observable baseline between the calibrations to be retained. For the PODRIX, the Galileo calibration x-offset is chosen to be constrained to zero whereas for the combined, the TriG calibration is constrained.

### 8.2.5 POD Processing Strategy

The POD processing strategy follows closely the procedure previously described in Section 5.2. The primary difference is the use of the Rapid JPL multi-GNSS clock product instead of the final products, which at the time of writing do not include the orbit and clock products for Galileo. The IGS14 PCO and PV calibrations from igs14_2196.atx (Rebischung and Schmid, 2016) are applied with the exception of the GPS IIIA which uses the estimated extension described

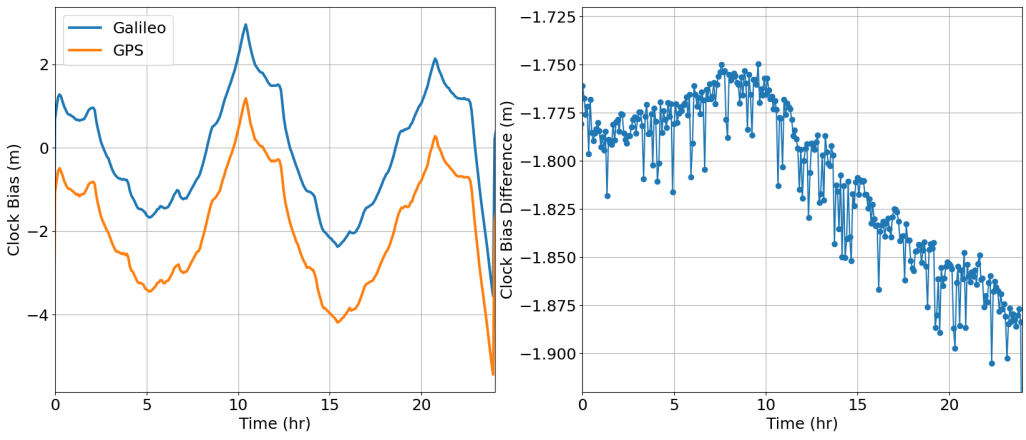


Figure 8.4: Receiver clock bias for PODRIX-Galileo (blue) and PODRIX-GPS (orange) and solution differences from 2022-01-22

in Chapter 7. Finally, while the PODRIX GPS and Galileo observations share a common clock bias contribution from the receiver, there exists an inter-signal bias between the observable clock solutions. Also, as noted by Peter et al. (2022), there are small glitches (2-3 cm) in the GPS phase observations which show up in clock solution as seen in Figure 8.4. This prevents the ability to estimate a constant inter-signal bias as it would degrade the ambiguity resolution. For this reason, a separate clock bias is estimated for the TriG, PODRIX-GPS, and PODRIX-Galileo observation sets.

## 8.3 TriG/PODRIX In-Track Bias Correction

Before processing a combined solution, we conducted a comparative evaluation of TriG based solutions to separately processed PODRIX-GPS and PODRIX-Galileo orbit solutions. The applied background models and estimation strategies are the same for all three solutions. The following comparisons show the differences between 30-hour reduced-dynamic solutions applying the pre-flight antenna calibrations and ambiguity resolution. Figure 8.5 shows the statistics from 550 days of the mean component differences of the central 24-hours for each day in the radial, cross-track, and in-track directions. Small radial differences exist between GPS and Galileo solutions of a few

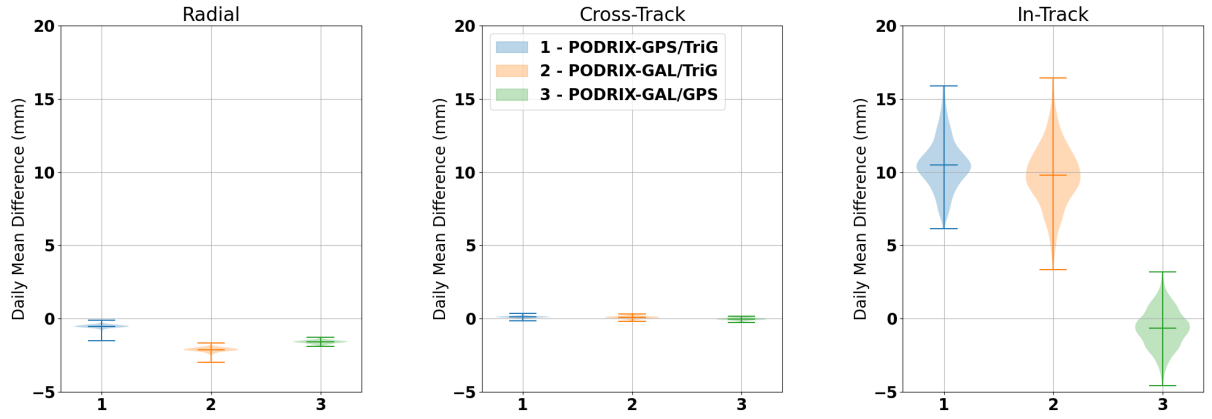


Figure 8.5: Daily mean component differences between PODRIX-GPS and TriG solutions (blue), PODRIX-Galileo and TriG (orange), and PODRIX-Galileo and PODRIX-GPS for radial (left), cross-track (middle), and in-track (right) components from 2021-06-30 to 2022-12-31

millimeters. This is likely due to inconsistencies between the pre-flight calibrations and the applied transmitter calibrations. The offsets in the cross-track differences are also small, below 0.5 mm. The in-track differences, however, show a consistent offset of about 10 mm between the two receiver solutions regardless of the constellation used with the PODRIX. While not significantly impactful for altimetry science, it is important for better understanding the behavior of each receiver.

The approximately 10 mm shift between the TriG and PODRIX is consistent with the observed baseline shift as reported by Desai et al. (2022) and Montenbruck et al. (2022). The observed differences between solutions is relative, and it could potentially be due to one, or both receivers. In order to determine the cause, the first step is to determine which receiver is the source of the relative bias. To do this, we examined the SLR residuals from each orbit solution used in the above comparisons for systematic body-frame errors. These offsets will map into the SLR measurements based on observation line-of-sight azimuth and elevation using

$$SLR_{res} = X_{off}cos(el)cos(az) + Y_{off}cos(el)sin(az) + Z_{off}sin(el) \tag{8.1}$$

We can estimate the offsets using a least squares approach with the resulting offsets being in the same frame as the SLR to ground station line-of-sight azimuth and elevation, which in this case is the spacecraft body frame. Because of the yaw-fixed attitude, these offsets will be highly correlated with the orbit frame. The least squares fit produces a body x-offset, which corresponds roughly to an in-track offset of 8.6 mm for TriG orbit solutions that is not present in either of the PODRIX solutions as shown in Table 8.2. Timing errors in the SLR observations can map into an

Table 8.2: Spacecraft body-x/y/z offsets estimated from the SLR residuals. These are correlated with the orbit in-track (body-x), cross-track (body-y), and radial (body-z) directions

| | rms ($mm$) | x ($mm$) | y ($mm$) | z ($mm$) |
|---|---|---|---|---|
| TriG | 8.2 | 8.55 | -2.69 | 4.02 |
| PODRIX-GPS | 7.7 | -0.97 | -2.57 | 3.56 |
| PODRIX-Galileo | 7.5 | -0.89 | -2.60 | 1.68 |

in-track error at the few mm level (Arnold et al., 2019), but the TriG in-track offset is larger than would be expected. This indicates the TriG as the dominant source of the relative in-track bias.

### 8.3.1 Timing Effects on Pseudorange

An in-track/body-x error such as the one seen here can be caused by something physical, such as an error in the antenna reference point, or timing errors. The yaw-fixed attitude of Sentinel-6 MF can make distinguishing these two effects difficult. However, the 180 degree yaw-flips allow for separating physical offsets from in-track offsets caused by timing errors. As shown in more detail later, this bias appears to be caused by a timing error.

Receiver timing errors change the observed pseudorange in two ways: a bias across all observations from the receiver clock, and a range-rate effect related to time-tag errors. For a given transmitter and receiver pair and ignoring ionosphere, multipath, and noise, the observed pseudorange is

$$\rho = c(t^r_{rx} - t^t_{tx}) \tag{8.2}$$

where $\rho$ is the pseudorange, $t^r_{rx}$ is the receiver clock time at time of reception, and $t^t_{tx}$ transmitter clock time at time of transmission. This can be rewritten in terms of the geometric range and the receiver and transmitter clock biases relative to GNSS time ($t_{GNSS}$) as

$$\rho = r + \delta t^r_{rx}(c - \dot{\rho}) - c\delta t^t_{tx} \tag{8.3}$$

where

$$\delta t^r_{rx} = t^r_{GNSS} - t^r_{rx} \tag{8.4}$$

$$\delta t^t_{tx} = t^t_{GNSS} - t^t_{tx} \tag{8.5}$$

Equation 8.3 models the expected pseudorange by incorporating both the bias and time-tag effects under the assumption that the time-tag bias is only due to the receiver clock offset relative to $t_{GNSS}$. It should be noted that modeling the time-tag in this way will have very little effect on the estimated clock bias. This is due to the fact that $c$ is much larger than $\dot{\rho}$. However, given the

high range rates for a LEO spacecraft of more than 6000 $m/s$, it will have a significant impact on the expected pseudorange. The TriG receiver clock bias is often larger than 100 $\mu$s which could potentially result in over half a meter difference in the modeled pseudorange.

The pseudorange as modeled in Equation 8.3 works well, but as mentioned before, assumes that the time-tag offset is consistent with the receiver clock offset. If this assumption does not hold true, either because of an added range bias (clock-like bias but no effect on time-tag) or a time-tag offset (from some source other than the receiver clock), then it will produce an error in the modeled pseudorange that is absorbed by an in-track offset when the position of the spacecraft is estimated. This in-track offset is proportional to the receiver velocity and the timing error.

When the pseudorange is modeled using Equation 8.3, it is not possible to separate a pure range bias from a pure time-tag bias. This can be shown by first adding a time-tag bias term, $\tau$, to Equation 8.3 (dropping the transmitter contribution) which results in

$$\rho = r + \delta t^r_{rx}(c - \dot{\rho}) + \tau\dot{\rho} + \ldots \tag{8.6}$$

Separating the receiver clock in terms of a new clock bias, $\delta\hat{t}^r_{rx}$, and the time-tag bias produces

$$\delta t^r_{rx} = \delta\hat{t}^r_{rx} + \tau \tag{8.7}$$

Plugging Equation 8.7 back into Equation 8.6 results in

$$\rho = r + \delta\hat{t}^r_{rx}(c - \dot{\rho}) + \tau c + \ldots \tag{8.8}$$

Which is equivalent to Equation 8.6 but expressed in terms of a range bias instead of a time-tag bias, and having a new clock bias offset by the range bias ($\delta\hat{t}^r_{rx} = \delta t^r_{rx} - \tau$). Estimation of either a constant range bias or time-tag bias allows for the separation of the clock bias and the time-tag. In practice, it is easier to estimate a constant range bias over the entire solution arc and an independent white noise receiver clock bias at each epoch.

To test this hypothesis, a constant range bias was estimated for a combined TriG and PODRIX 30-hour reduced-dynamic orbit solution with applied pre-launch antenna calibrations and ambiguity resolution. Daily range biases were estimated for both the TriG and PODRIX-GPS observations but not for PODRIX-Galileo. Figure 8.6 (left) shows the daily estimated range bias values across 1.5 years. Both solutions have a similar pattern in the time history with the TriG showing a large offset relative to the PODRIX-GPS. The differences between the two solutions show a relatively consistent offset between the two. The mean offset weighted by the formal error over the entire time-span results in a range bias estimate for the TriG of 405 m and for the PODRIX-GPS of -38 m.

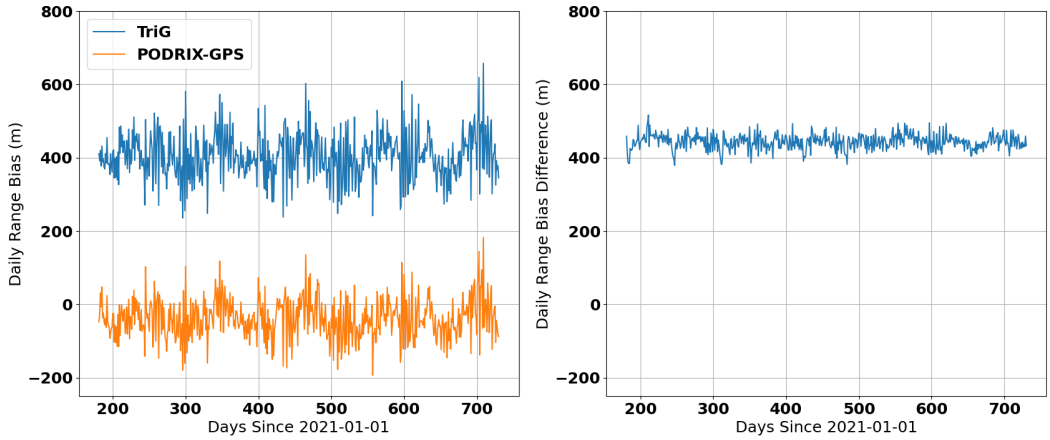


Figure 8.6: Daily range bias estimates across 550 days (left) for the TriG (Blue) and PODRIX-GPS (orange) and the daily estimated differences (right)

The estimated range bias will incorporate the relative in-track offsets due to both timing effects and any baseline offsets aligned with the in-track direction. This can be clearly demonstrated by adjusting the TriG body-fixed antenna reference point by 10 mm in the body-x direction. Figure 8.7 shows the time history for three months with this offset applied. The range bias estimates are consistent between the TriG and PODRIX-GPS, but only during the fly forward attitude where the applied body-x baseline offset is able to compensate for the in-track offset. However, during the

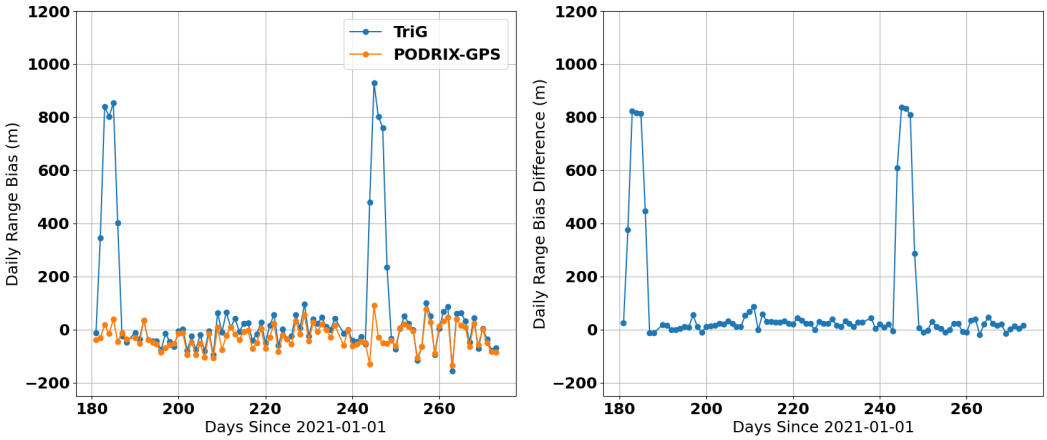


Figure 8.7: Daily range bias estimates (left) for the TriG (blue) and PODRIX-GPS (orange) and the daily estimated differences (right) after adjusting the TriG antenna reference point in the body-x direction by 10 mm

periods with 180 degree yaw bias, the range bias for the TriG approximately doubles, indicating that a baseline error cannot be the cause of the in-track bias. In contrast, Figure 8.8 shows the daily estimated range bias after offsetting the TriG observations by 405 m. Here the results are in

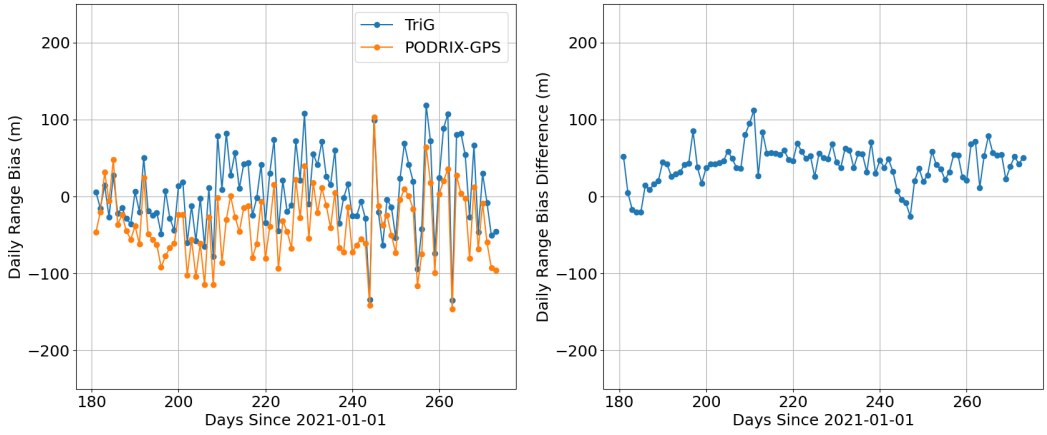


Figure 8.8: Daily range bias estimates (left) for the TriG (blue) and PODRIX-GPS (orange) and the daily estimated differences (right) after removing a 405 m range bias from the TriG observations

good agreement across the entire time span including during the days with 180 degree yaw bias. There is potentially a small observable baseline offset between the two but appears to be less than 1 mm. The Sentinel-6 MF yaw-flip maneuvers help to decouple the effects of a pure baseline offset from a pure timing error. Both baseline offsets and timing errors should be consistent regardless of the spacecraft attitude. However, offsets in the baseline are linked to the spacecraft body frame and timing errors to the orbit frame. Because of this, we can conclude that the in-track bias between the TriG and PODRIX solutions is dominated by a timing error and not a physical baseline error between the antennas.

The SLR residual indication of a relative bias of about 9.5 mm between the TriG and PODRIX is consistent with the absolute range bias of 405 m or equivalent to a time-tag inconsistency of 1.35 $\mu$s. Given the orbital velocity of Sentinel-6 MF ($\sim$7000 m/s), a time-tag error of 1.35 $\mu$s produces approximately 9.5 mm of displacement consistent with the observed bias between the TriG and PODRIX. The source of this error is unclear, but determination of the exact cause is beyond the scope of this study. Thus, for the remainder of this analysis, all TriG solutions simply apply a fixed range bias of 405 m to the pseudorange and phase observations.

## 8.4 Results

The results presented here cover 550 days from June 30, 2021 to December 31, 2022. An evaluation of six different 30-hour, reduced-dynamic orbit solutions with ambiguity resolution are examined and compared: a TriG only solution, a TriG only solution with 10 degree elevation mask, a PODRIX-GPS only solution, a PODRIX-Galileo only solution, a PODRIX-GPS plus Galileo solution, and a TriG plus PODRIX combined solution. Each solution uses an in-flight antenna calibration estimated from consistent methodology. The solutions are evaluated for consistency and precision using post-fit residual rms, orbit overlaps, and ambiguity resolution statistics. Finally, the orbit accuracy for each solution is assessed with independent SLR observations.

### 8.4.1 Antenna Calibration

Figure 8.9 shows the estimated in-flight PV corrections for each antenna calibration in the combined solution. Because spacecraft body-x/y/z offsets can be absorbed in the PVs, it is useful to examine how these offsets have changed relative to the nominal pre-launch antenna calibration. Table 8.3 lists the body-x/y/z offsets contained within each calibration correction. The bold offset represents the antenna for which the x-offset was constrained. At the scale in Figure 8.9, each separate antenna calibration appears very similar, and so only the results from the combined solution are shown. The antenna offsets within each calibration are consistent across the different solutions. GPS phase calibration corrections have very similar z-offsets of about 20 mm whereas

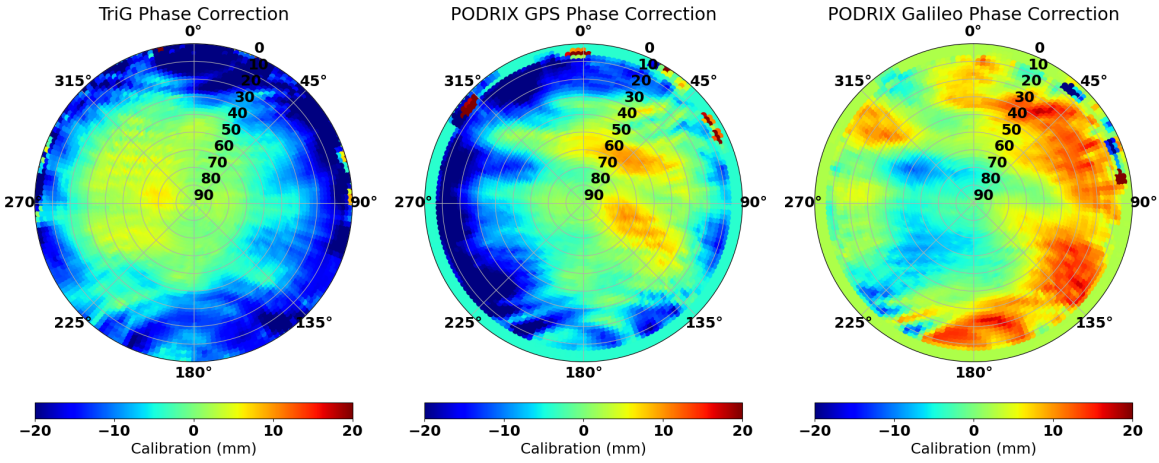


Figure 8.9: Correction to the pre-launch antenna calibration for the TriG (left), PODRIX-GPS (middle), and PODRIX-Galileo (right)

Table 8.3: Antenna offsets [body-x, body-y, body-z] computed from the pre-launch corrections. Constraints are applied to the bold x-offset

| | TriG (mm) | PODRIX-GPS (mm) | PODRIX-Galileo (mm) |
|---|---|---|---|
| TriG only | [**0.05**, −5.48, 20.82] | – | – |
| PODRIX-GPS only | – | [−**0.05**, 9.33, 20.06] | – |
| PODRIX-Galileo only | – | – | [−**0.12**, 7.14, −12.18] |
| PODRIX-GPS/Galileo | – | [−0.26, 9.35, 19.96] | [−**0.12**, 7.06, −11.93] |
| TriG plus PODRIX | [**0.05**, −5.51, 20.67] | [1.06, 9.36, 20.09] | [1.16, 7.02, −11.78] |

PODRIX-Galileo has a -11 mm z-offset. It seems likely that the relatively large z-offsets are linked to the IGS14 transmitter calibrations. For the combined solution, constraining the TriG x-offset to zero results in a small offset of about 1 mm in both the PODRIX calibrations. This may be the result of a small baseline difference or possibly related to the estimated range bias for the TriG. Nevertheless, it is quite small. Fairly sizable y-offsets of 5-9 mm exist in all three calibrations but with opposite signs between the TriG and PODRIX. Similar offsets were observed by Desai et al. (2022) and Montenbruck et al. (2022) with a potential explanation being caused by an attitude yaw-bias.

### 8.4.2 Internal Metrics

Each orbit solution is first evaluated using a set of internal metrics comprising the daily post-fit residual rms to test for goodness of fit. Next, a comparison of the orbit overlap difference rms is used to assess the orbit solution precision and consistency. This is followed by a discussion of the ambiguity resolution statistics for each solution.

Figures 8.10 and 8.11 show the distribution of the combined solution phase and code daily residual rms from 30-hour reduced-dynamic orbit solutions with ambiguity resolution. The mean of the daily rms ± the overall standard deviation is shown in Table 8.4. The TriG residuals are larger overall due to tracking down to zero degrees. When applying a 10 degree mask to the TriG, as is done for the PODRIX, the observations with the highest measurement noise are removed. This results in phase residuals that are slightly smaller than the PODRIX-GPS. The PODRIX-Galileo

Table 8.4: Post-fit residual rms in terms of the mean ± the standard deviation of the daily statistics

| | Ionosphere-free Phase (mm) | Ionosphere-free Code (mm) |
|---|---|---|
| TriG 1W/2W | 5.9 ± 0.45 | 660 ± 41 |
| TriG 1W/2W >10-deg | 3.7 ± 0.32 | 530 ± 35 |
| PODRIX 1W/2W | 4.2 ± 0.35 | 320 ± 48 |
| PODRIX 1C/2L | 4.1 ± 0.22 | 350 ± 50 |
| PODRIX E1/E5a | 3.4 ± 0.18 | 280 ± 30 |

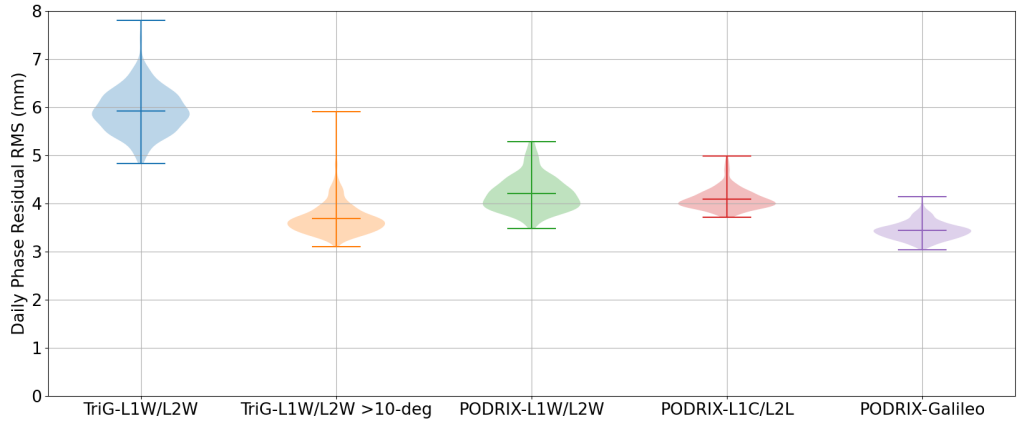


Figure 8.10: Distribution of the daily ionosphere-free phase residual rms statistics from the combined solution computed separately for TriG L1W/L2W, TriG >10-deg L1W/L2W, PODRIX-GPS L1W/L2W, PODRIX-GPS L1C/L2L, and PODRIX-Galileo L1C/L5Q

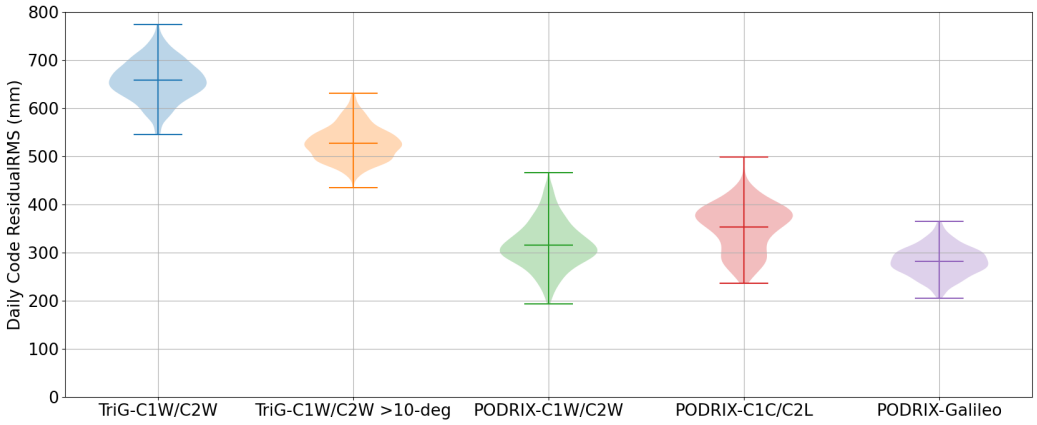


Figure 8.11: Distribution of the daily ionosphere-free code residual rms statistics from the combined solution computed separately for TriG C1W/C2W, TriG >10-deg C1W/C2W, PODRIX-GPS C1W/C2W, PODRIX-GPS C1C/C2L, and PODRIX-Galileo C1C/C5Q

phase and code residuals are smaller than any of the GPS with less variability overall. This can be attributed to the lower noise and multipath effects of wideband code tracking on L5 (Circiu et al., 2017). The PODRIX-GPS code observations are nearly 20 cm smaller than the TriG even

accounting for the 10 degree mask. Also, the PODRIX C1W/C2W observations have a similar rms to the C1C/C2L observations. The C1C/C2L residuals do exhibit a different distribution in Figure 8.11 which could possibly be related the residual receiver DCBs between C1W/C2W and C1C/C2L.

The orbit solution precision can be evaluated using orbit overlaps. From the 30-hour solution arcs, this results in 6 hours of overlap between each daily solution as shown in Figure 2.2. Using only the central four hours to avoid edge effects, a single rms value for the radial, cross-track, and in-track directions is computed from the daily component differences. Figure 8.12 shows the distribution of the daily rms statistics after $5\sigma$ outlier removal. All solutions exhibit very good precision with the TriG and PODRIX solutions showing very similar performance. The PODRIX-Galileo solution has slightly higher mean overlap rms and the most variability from day-to-day. Combining all observations into a single solution produces the most consistent overlap statistics with decreases in the mean overlap rms as well as in the daily variability across the solution time

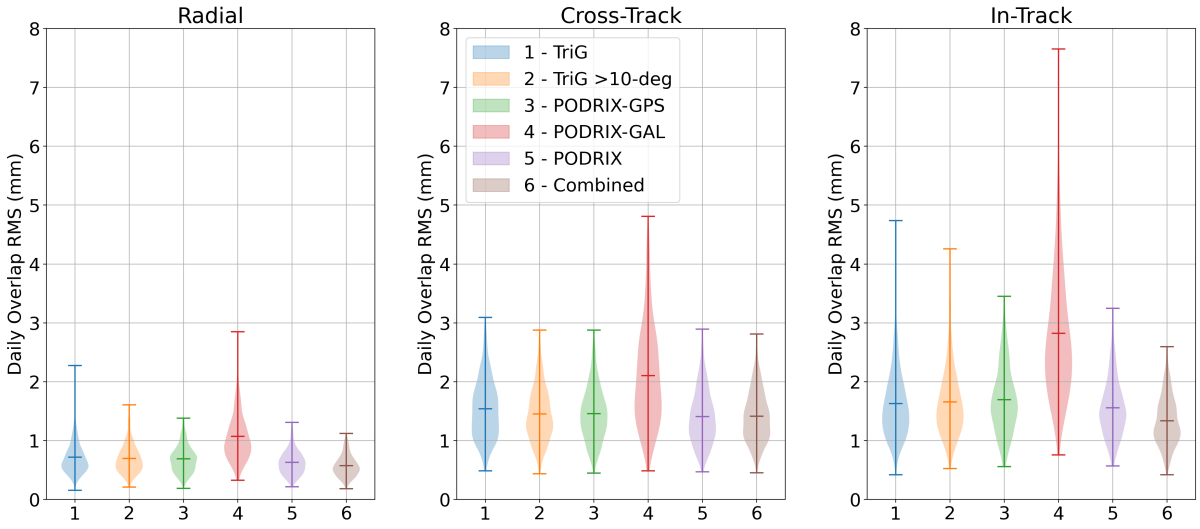


Figure 8.12: Daily overlap difference rms for radial (left), cross-track (middle), and in-track (right) from Sentinel-6 MF ambiguity-resolved reduced dynamic orbit solutions for six cases: 1) TriG, 2) TriG >10-deg, 3) PODRIX-GPS, 4) PODRIX Galileo, 5) PODRIX, 6) Combined

Table 8.5: Overlap difference rms in terms of the mean ± the standard deviation of the daily statistics after $5\sigma$ outlier removal

| | Radial Overlap (mm) | Cross-track (mm) | In-track (mm) |
|---|---|---|---|
| TriG | 0.72 ± 0.28 | 1.5 ± 0.5 | 1.6 ± 0.6 |
| TriG >10-deg | 0.70 ± 0.24 | 1.5 ± 0.5 | 1.7 ± 0.6 |
| PODRIX-GPS | 0.69 ± 0.23 | 1.5 ± 0.9 | 1.7 ± 0.6 |
| PODRIX-Galileo | 1.1 ± 0.4 | 2.1 ± 0.9 | 2.8 ± 1.1 |
| PODRIX | 0.63 ± 0.20 | 1.4 ± 0.5 | 1.6 ± 0.5 |
| Combined | 0.57 ± 0.18 | 1.4 ± 0.4 | 1.3 ± 0.4 |

span as shown in Table 8.5. The most notable improvement is for the in-track overlap which seems to benefit the most from the increase in observations. This is evident in both the PODRIX and the combined solutions. It is interesting to note, however, that applying a 10 degree elevation mask to the TriG did not degrade the solution precision. This is likely due to removal of the noisy low-elevation observations.

The slightly poorer performance of the PODRIX-Galileo compared to the other solutions may be due to a few factors. It is possible that performance may be degraded by the ISG14 calibrations and potential lower accuracy orbit and clock products. This could be tested by applying the newer IGS20 calibrations to evaluate this effect. It is also possible that the Galileo ambiguity resolution may play a factor and is discussed in more detail in the next section.

### 8.4.3 Ambiguity Resolution

Each of the daily reduced-dynamic POD solutions implement single-receiver ambiguity resolution (Bertiger et al., 2010b). The phase ambiguity biases are fixed using a wide-lane bias product estimated from a ground station network. This allows for the formation of double differences with the LEO receiver. The narrow-lane ambiguities are fixed based only on resolved wide-lane double differences that pass a confidence threshold and distance to the nearest integer test. The resulting constraints are not a linearly independent set of double-differences, but rather applied from all possible double-difference combinations. Because of this, constrained ambiguities are then applied

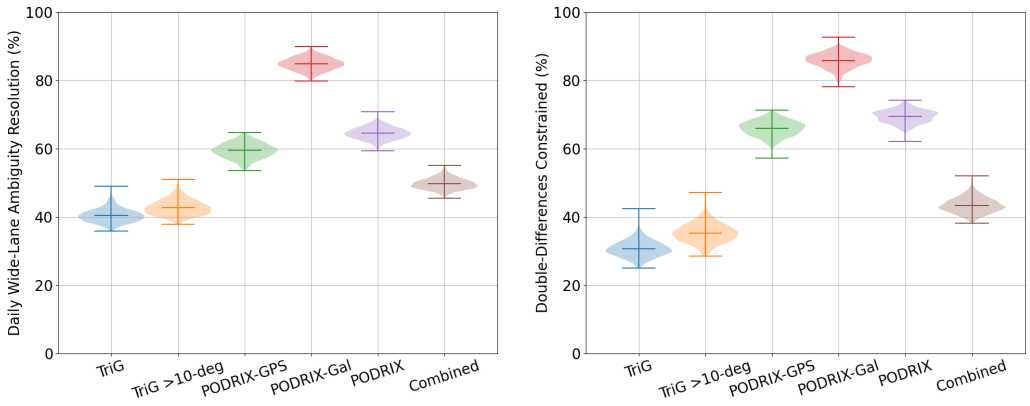


Figure 8.13: Daily solution percent of wide-lane samples fixed to within 10 centi-cycles (left), and the constrained double-differences as a percentage of the total possible for six solutions: 1) TriG tracking data (blue), 2) TriG tracking data > 10 degrees (orange), 3) PODRIX-GPS tracking data (green), 4) PODRIX-Galileo tracking data (red), 5) PODRIX tracking data (purple), 6) TriG plus PODRIX tracking data (brown)

within the filter smoother using a confidence weight of 10 cm. The ambiguity resolved solution is then iterated 10 times as described by Bertiger et al. (2010b).

Figure 8.13 shows the percentage of wide-lane samples (left) that have been resolved to less than 10 centi-cycles of the integer ambiguity and the constrained double-differences as a percentage of the total possible (right). The wide-lane resolution for the TriG has a relatively low percentage of samples fixed to within 10 centi-cycles with an overall mean of 40.3%. The PODRIX-GPS and Galileo, on the other hand, perform much better at 59.4% and 84.8% respectively. Because only passes with acceptable wide-lane criteria are constrained, a similar pattern is observed in the constrained double-differences as a percentage of the total possible. For the TriG, the cause of the poor wide-lane resolution is uncertain, but may be related to the large code residual rms observed earlier. It is interesting to note that the TriG does show a small benefit to the fixing statistics when the 10 degree elevation mask is applied.

Figure 8.14 (left) shows the daily total number of double-difference passes which are constrained in the 30-hour solution arc. Despite the lower fixing statistics for the TriG, it has a similar number of constraints applied as the PODRIX-GPS which is likely due to the higher number of

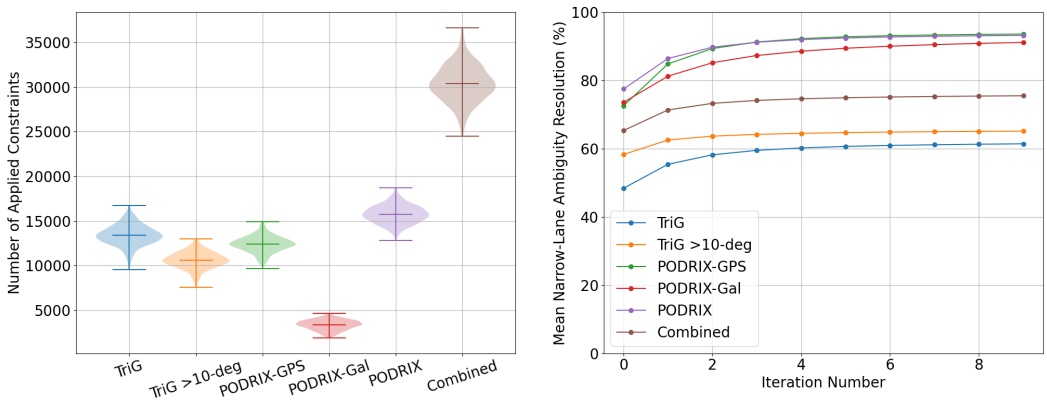


Figure 8.14: Total number of daily applied constraints (left) and the overall mean narrow-lane (right) samples resolved to within 10 centi-cycles of an integer after each iteration from 2021-06-30 to 2022-12-31 for six solutions: 1) TriG tracking data (blue), 2) TriG tracking data > 10 degrees (orange), 3) PODRIX-GPS tracking data (green), 4) PODRIX-Galileo tracking data (red), 5) PODRIX tracking data (purple), 6) TriG plus PODRIX tracking data (brown)

tracked GPS transmitters for the TriG. Galileo on the other hand, despite having the highest fixing percentage, has significantly fewer applied constraints. The reason for this is likely related to the wide-lane bias product containing far fewer stations for Galileo than for GPS and so fewer double differences are possible. In the combined solution, the applied constraints are dominated by the GPS double differences.

The overall average narrow-lane resolution as a function of iteration is shown in Figure 8.14 (right). Like the wide-lane, the TriG percentage of narrow-lane samples resolved to less than 10 centi-cycles is the lowest across all iterations. The lower narrow-lane fixing rate for the TriG is also evident in the combined solution. This poorer fixing rate is due to a number of fixed ambiguities which appear to be in error by a half-integer. This half-integer error has also been observed by Bertiger et al. (2010a). Given that the ambiguity resolution is applied with a soft constraint, it does not appear to have a significant effect on the orbit solution.

### 8.4.4 Independent SLR Residuals

To evaluate the orbit accuracy, we consider independent SLR observations (Pearlman et al., 2019). Only a set of high performing SLR stations with biases below 5 mm for the entire data set are considered to evaluate the Sentinel-6 MF orbit solutions. These include the following six stations: Greenbelt, Maryland; Graz, Austria; Herstmonceux, United Kingdom; Mt Stromlo, Australia; Yarragadee, Australia; and Wettzell, Germany. The SLR corrections discussed in Section 5.4 are applied to the observations. After $5\sigma$ filtering, Figure 8.15 shows the SLR one-way residual rms in the left panel, and the overall bias in the right panel as a function of boresight angle relative

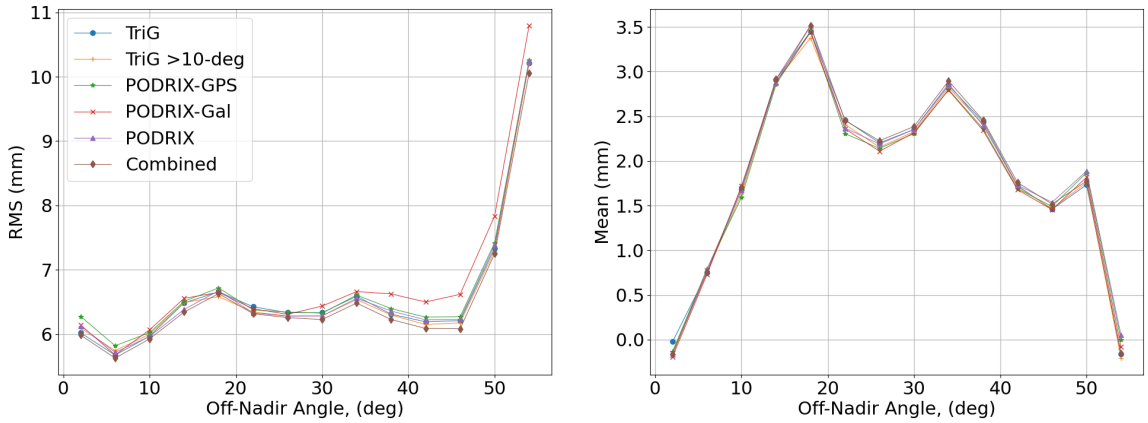


Figure 8.15: SLR residual rms (left) and bias (right) as a function of boresight angle

LRA. Here we can see that all orbit solutions are relatively similar with rms values of 6.9 mm for TriG, 7.0 mm for PODRIX-GPS, 7.3 mm for PODRIX-Galileo, 6.9 mm for PODRIX, and 6.8 mm for the combined solution. Table 8.6 shows a comparison of the overall statistics from each set of orbit solutions. The SLR residual rms below 45 degrees off-nadir angle (high station elevation) in the LRA frame of 6.5 mm or lower for all solutions indicates radial accuracies better than 1 cm.

From the SLR residuals, mean body-x/y/z offset, correlated with the radial, cross-track, and in-track directions, can be computed using a least squares approach with Equation 8.1. Table 8.7 lists the computed spacecraft body-x/y/z offsets. We see that all offsets are below 3 mm, and the application of the range bias on the TriG solution has effectively removed the body-x bias

Table 8.6: Comparison of the overall rms, bias, and rms below 45 degrees off-nadir angle

| | rms (mm) | mean (mm) | std (mm) | rms < 45-deg (mm) |
|---|---|---|---|---|
| TriG | 6.9 | 1.79 | 6.7 | 6.3 |
| TriG >10-deg | 6.9 | 1.78 | 6.7 | 6.3 |
| PODRIX-GPS | 7.0 | 1.80 | 6.7 | 6.4 |
| PODRIX-Galileo | 7.3 | 1.78 | 7.0 | 6.5 |
| PODRIX | 6.9 | 1.85 | 6.7 | 6.3 |
| TriG plus PODRIX | 6.8 | 1.82 | 6.6 | 6.2 |

Table 8.7: Spacecraft body-x/y/z offsets estimated from the SLR residuals. These are correlated with the orbit in-track (body-x), cross-track (body-y), and radial (body-z) directions

| | X ($mm$) | Y ($mm$) | Z ($mm$) |
|---|---|---|---|
| TriG | 0.50 | -2.59 | 2.40 |
| TriG >10-deg | 0.54 | -2.65 | 2.38 |
| PODRIX-GPS | -0.50 | -2.58 | 2.35 |
| PODRIX-Galileo | -0.89 | -2.71 | 2.29 |
| PODRIX | -0.78 | -2.59 | 2.39 |
| TriG plus PODRIX | 0.47 | -2.58 | 2.45 |

as previously observed. The Body-y/z offsets are consistent between each solution with relative differences being smaller 0.2 mm. The body-z offsets will be correlated with the overall biases in the right panel of Figure 8.15 which are related to both the station biases and potentially errors in the range bias correction shown in Figure 5.7. The body-y offsets are more difficult to explain. One potential explanation would be an body-y error in the spacecraft center of mass or the LRA spacecraft reference location. However, given that each of the antenna calibrations have absorbed fairly large body-y offsets, there appears to be some systematic error in the Sentinel-6 MF metrology that may explain both of these effects and could be related to the proposed yaw-bias given by Desai et al. (2022) and Montenbruck et al. (2022).

## 8.5 Summary

Sentinel-6 MF is the first operational science platform in LEO that flies multiple receivers and also tracks GPS plus Galileo observations. After estimation of antenna calibrations, orbit solutions derived from TriG and PODRIX observations were assessed for precision and accuracy. Both the TriG and PODRIX observations are capable of producing highly accurate orbit solutions.

The ability to compare the TriG and PODRIX solutions revealed a range bias of 405 m in the TriG observations. Correcting for this removed a systematic bias in the in-track direction as revealed by the SLR residual analysis. After application of the range bias for the TriG results in an SLR residual rms reduction from 8.2 mm to 6.9 mm. This improvement is due to both the in-track bias correction as well as the applied antenna calibration. When including the TriG and PODRIX observations in a single solution, this results in the most precise orbit solutions as evidenced by lower orbit overlap rms values and lowest SLR residual rms.

Overall, of the two receivers, the TriG and PODRIX had similar performance in terms of orbit overlaps and SLR residual rms. For the PODRIX, some improvement is possible. The use of multi-code GPS signals complicates the ambiguity resolution due to the presence of DCBs that are not accounted for in the current wide-lane products. This is evident in the lower wide-lane resolution and percentage of fixed double differences relative the PODRIX-Galileo. However, the Galileo solutions performed slightly worse in terms of orbit overlaps and SLR residuals compared to GPS potentially due to the transmitter calibrations, orbit and clock product, and significantly fewer available double-difference combinations in the wide-lane bias product. Despite this, Galileo had lower phase and code residuals rms which are benefits of wideband code tracking on L5. As the Galileo orbit, clock, and wide-lane products mature, it will likely be a key contributor to LEO based science missions.

# Chapter 9

# Conclusions and Future Work

## 9.1 Conclusions

GNSS-based precise orbit determination is a technique that can provide insights beyond the orbit solutions themselves. In essence, the abundance of GNSS measurements allows for an assessment and improvement of the dynamic force models, measurement models, and POD solution strategy, which can then be applied back into the POD process and improve the subsequent orbit solutions.

The CYGNSS mission, a constellation of eight small satellites designed to use reflected GNSS signals for retrieval of ocean surface winds, provides an opportunity to study the limiting factors of GNSS-R altimetry. For this application, orbit knowledge is a significant error source, and the navigation solutions, computed with the onboard single-frequency GPS receiver, do not provide sufficient accuracy. Using more than five months of data from the CYGNSS FM05 satellite, the accuracy of the CYGNSS orbit solutions is improved by evaluating the solution strategies and associated errors when applied to the GRACE mission, for which highly accurate orbit solutions are available. Of the two competing solution strategies, the GRAPHIC method is shown to be more accurate and precise than the code-only method. The bound on CYGNSS GRAPHIC orbit errors, as inferred by GRACE, places a $1\sigma$ range of 1.4 – 5.3 cm for radial, 1.2 – 31 cm for cross-track, and 3.0 – 15 cm for in-track with a 3-D position error of 3.5 – 40 cm. The lower bound is determined from the overlap precision and the upper bound from the GRAPHIC/Code-only differences. The upper bound is dominated by code-only solution errors, and therefore the GRAPHIC solutions will

be closer to the lower bound, particularly for the cross-track component. Based on the analysis of GRACE POD solutions using the same methodology, the $1\sigma$ CYGNSS GRAPHIC orbit accuracy is expected to be 3 cm radial, 3 cm cross-track, and 6 cm in-track, resulting in a 3-D accuracy better than 10 cm. The improved orbit accuracy provided by this method allows researchers to better determine the potential utility of the CYGNSS constellation for GNSS-R based altimetry and potential single-frequency POD solutions for other small satellites.

Unlike CYGNSS, Sentinel-6 has high quality dual-frequency GNSS observations from two independent receivers along with independent SLR observations which can be used to validate the orbit solutions. This configuration provides the ability to study and improve the models which are inputs to the POD solution process. Using only the TriG observations, the SRP modeling is improved for Sentinel-6 MF. From dynamic orbit solutions the improved SRP modeling produce much more consistent estimates for drag and solar scale, internal metrics, and estimated antenna offsets when compared to the manufacturer provided macromodel. The improved consistency of the dynamic solutions is important for antenna calibrations which are estimated within these solutions. Independent SLR residuals measured against reduced-dynamic orbit solutions with ambiguity resolution are improved from 8.6 mm to 8.1 mm. This study shows the benefit to POD by improving the dynamic models.

The current IGS14 GPS IIIA PVs above 14 degree boresight angles are fixed to the 14 degree value. This results in poor phase modeling of the GPS IIIA measurements. This study was undertaken with the goal of improving the existing measurement models for the GPS IIIA satellites. An extension for the GPS IIIA PVs for boresight angles greater than 14 degrees is estimated using an approach such that the extension is consistent with the IGS14 Block II PVs. Use of this GPS IIIA PV extension, determined from only Sentinel-6 MF TriG tracking data, results in better consistency between orbit solutions determined from Block II-only tracking data and those including both Block II and GPS IIIA. Most metrics improve when using the combination of Block II and IIIA tracking data along with the estimated GPS IIIA PV extension, and degrade when applying the original IGS14 GPS IIIA PVs. This result is validated on Jason-3 which was not

used in the estimation of the GPS IIIA extension. POD solutions for LEO will likely be degraded without a more reliable antenna calibration for GPS IIIA satellites, with the impact continuing to grow as the number of GPS IIIA satellites increases. The estimates for the GPS IIIA PVs for boresight angles greater than 14 degrees removes this potential degradation.

Because Sentinel-6 MF is equipped with two independent receivers, a TriG and multi-GNSS PODRIX (GPS + Galileo), it provides an opportunity to compare various solutions based on different receivers and GNSS constellations. Applying the previous methods, orbit solutions derived from the TriG and PODRIX observations were assessed for precision and accuracy. The ability to compare the TriG and PODRIX solutions revealed a range bias of 405 m in the TriG observations. Correcting for this removed a systematic bias in the in-track direction. This improved the TriG only SLR residuals significantly. The SLR residual rms decreases from 8.2 mm to 6.9 mm for TriG based orbit solutions factoring the effects of both the in-flight estimated antenna calibration and applied range bias. Overall, both receivers exhibited similar performance in terms of orbit overlaps and SLR residual rms. The use of Galileo observations showed significantly lower phase and code residuals rms and better wide-lane fixing statistics, but overall performance was limited by the available double-differences in the wide-lane bias product.

The work presented in this thesis advances the measurement models, force models, and solution strategies. All studies estimate an in-flight receiver antenna calibration which improves the measurement models. CYGNSS examined both the measurement models and POD estimation strategy for single-frequency GRAPHIC POD solutions. Sentinel-6 MF was used to study methods for improving the solar radiation pressure dynamic models and GPS transmitter measurement models, both of which were applied to a multi-receiver and multi-constellation POD solution.

## 9.2 Future Work

Looking forward from this work, there are several interesting observations that warrant further investigation. For CYGNSS, the cross-track difference between the code-only and GRAPHIC solutions has yet to be explained. The presence of the same cross-track signal for Sentinel-6 MF

eliminates an ionosphere signal as the likely cause. Two potential sources that could be examined are either a latitude dependent clock signal in the GPS constellation, or the lack of code antenna calibrations for the GPS transmitters. To investigate this would require estimation of the GPS orbit and clock products, including observations from other LEO satellites, not just ground stations.

Sentinel-6 MF provides a variety of avenues for future study. In the context of the work presented here, there are a few anomalies that would require further investigation. The most puzzling is the poor wide-lane ambiguity resolution performance of the TriG receiver and high code residual rms. This could be related to flex power (Esenbuğa and Hauschild, 2020; Steigenberger et al., 2019) that may impact the wide-lane bias product, the TriG observations, or both. It is also possible that there is some link between the observed range bias which impacts the ability to consistently resolve the wide-lane ambiguities. Further analysis would need to be done to fully understand the cause and correct it.

The estimated antenna calibration y-offsets for the TriG and PODRIX seem larger than expected. Given that they are on opposite sides of the center of mass, this could be related to a small yaw-bias as presented by both Desai et al. (2022) and Montenbruck et al. (2022). While the evidence presented is based strictly on the observations, if such a yaw-bias exists, it may be possible to observe the effects on estimated empirical accelerations and would provide a second line of evidence to support this conclusion.

Finally, given the performance and low multipath properties of the Sentinel-6 MF TriG receiver, it also presents the possibility for use as a reference against which to estimate the antenna calibrations of the entire GPS constellation in an approach similar to that performed by Haines et al. (2015). The role of Sentinel-6 MF as an orbiting geodetic observatory linking GPS and Galileo plus SLR could enable better realizations of the terrestrial reference frame along with improved gravity recovery. Alternatively, with the manufacturer-provided GPS IIIA antenna patterns available, a promising approach is to estimate the Block II antenna PVs relative to the GPS IIIA and evaluated for improvements in GPS performance. In particular, it may explain the large antenna z-offsets observed in the TriG and PODRIX-GPS in-flight antenna calibrations.

## Bibliography


Altamimi, Z., Rebischung, P., Métivier, L., and Collilieux, X. (2016). ITRF2014: A new release of the International Terrestrial Reference Frame modeling nonlinear station motions. Journal of Geophysical Research: Solid Earth, 121(8):6109–6131. doi: https://doi.org/10.1002/2016JB013098.

Aparicio, M., Brodie, P., Doyle, L., Rajan, J., and Torrione, P. (1996). GPS satellite and payload. Global Positioning System: Theory and applications., 1:209–244.

Arnold, D., Montenbruck, O., Hackel, S., and Sośnica, K. (2019). Satellite laser ranging to low earth orbiters: orbit and network validation. Journal of Geodesy, 93(11):2315–2334. doi: https://doi.org/10.1007/s00190-018-1140-4.

Auriol, A. and Tourain, C. (2010). DORIS system: the new age. Advances in Space Research, 46(12):1484–1496. doi: https://doi.org/10.1016/j.asr.2010.05.015.

Bar-Sever, Y. (2021). Orbit determination with GNSS. In Morton, Y. J., van Diggelen, F., Spilker Jr, J. J., Parkinson, B. W., Lo, S., and Gao, G., editors, Position, navigation, and timing technologies in the 21st century: Integrated satellite navigation, sensor systems, and civil applications, volume 2. John Wiley & Sons.

Bar-Sever, Y. and Kuang, D. (2003). New empirically-derived solar radiation pressure model for GPS satellites. IPN Progress Report, page 15:42–159.

Bertiger, W., Bar-Sever, Y., Christensen, E., Davis, E., Guinn, J., Haines, B., Ibanez-Meier, R., Jee, J., Lichten, S., Melbourne, W., et al. (1994). GPS precise tracking of TOPEX/POSEIDON: Results and implications. Journal of Geophysical Research: Oceans, 99(C12):24449–24464. doi: https://10.1029/94JC01171.

Bertiger, W., Bar-Sever, Y., Dorsey, A., Haines, B., Harvey, N., Hemberger, D., Heflin, M., Lu, W., Miller, M., Moore, A. W., Murphy, D., Ries, P., Romans, L., Sibois, A., Sibthorpe, A., Szilagyi, B., Vallisneri, M., and Willis, P. (2020). GipsyX/RTGx, a new tool set for space geodetic operations and research. Advances in Space Research, 66(3):469–489. doi: https://doi.org/10.1016/j.asr.2020.04.015.

Bertiger, W., Desai, S., Dorsey, A., Haines, B., Harvey, N., Kuang, D., Sibthorpe, A., and Weiss, J. (2010a). Sub-centimeter precision orbit determination with GPS for ocean altimetry. Marine Geodesy, 33(S1):363–378. doi: https://doi.org/10.1080/01490419.2010.487800.

Bertiger, W., Desai, S., Haines, B., Harvey, N., Moore, A. W., Owen, S., and Weiss, J. P. (2010b). Single receiver phase ambiguity resolution with GPS data. Journal of Geodesy, 84(5):327–337. doi: https://doi.org/10.1007/s00190-010-0371-9.

Bierman, G. J. (2006). Factorization methods for discrete sequential estimation. Courier Corporation.

Bilitza, D., Altadill, D., Truhlik, V., Shubin, V., Galkin, I., Reinisch, B., and Huang, X. (2017). International Reference Ionosphere 2016: From ionospheric climate to real-time weather predictions. Space Weather, 15(2):418–429. doi: https://doi.org/10.1002/2016SW001593.

Birmingham, W., Miller, B., and Stein, W. (1983). Experimental results of using the GPS for Landsat 4 onboard navigation. Navigation, 30(3):244–251. doi: https://doi.org/10.1002/j.2161-4296.1983.tb00843.x.

Bock, H., Jäggi, A., Dach, R., Schaer, S., and Beutler, G. (2009). GPS single-frequency orbit determination for low Earth orbiting satellites. Advances in Space Research, 43(5):783–791. doi: https://doi.org/10.1016/j.asr.2008.12.003.

Bruinsma, S., Thuillier, G., and Barlier, F. (2003). The DTM-2000 empirical thermosphere model with new data assimilation and constraints at lower boundary: accuracy and properties. Journal of Atmospheric and Solar-Terrestrial Physics, 65(9):1053–1070. doi: https://doi.org/10.1016/S1364-6826(03)00137-8.

Carreno-Luengo, H., Lowe, S. T., Zuffada, C., Esterhuizen, S., and Oveisgharan, S. (2017). GNSS-R from the SMAP and CyGNSS missions: Application to polarimetric scatterometry and ocean altimetry. In 2017 IEEE International Geoscience and Remote Sensing Symposium (IGARSS), pages 5019–5021. IEEE.

Circiu, M.-S., Meurer, M., Felux, M., Gerbeth, D., Thölert, S., Vergara, M., Enneking, C., Sgammini, M., Pullen, S., and Antreich, F. (2017). Evaluation of GPS L5 and Galileo E1 and E5a performance for future multifrequency and multiconstellation GBAS. Navigation: Journal of The Institute of Navigation, 64(1):149–163. doi: https://doi.org/10.1002/navi.181.

Colombo, O. L. (1989). The dynamics of Global Positioning System orbits and the determination of precise ephemerides. Journal of Geophysical Research: Solid Earth, 94(B7):9167–9182. doi: https://doi.org/10.1029/JB094iB07p09167.

Conrad, A., Axelrad, P., Desai, S. D., and Haines, B. J. (2022). Improved modeling of the solar radiation pressure for the Sentinel-6 MF spacecraft. In Proceedings of the 35rd International Technical Meeting of the Satellite Division of The Institute of Navigation (ION GNSS+ 2022), September 2022. doi: https://doi.org/10.33012/2022.18478.

Conrad, A., Desai, S., Haines, B., and Axelrad, P. (2023a). Extending the GPS IIIA antenna calibration for precise orbit determination of low Earth orbit satellites. Journal of Geodesy, 97(4):35. doi: https://doi.org/10.1007/s00190-023-01718-0.

Conrad, A. V., Axelrad, P., Haines, B., Zuffada, C., and O'Brien, A. (2023b). Improved GPS-based single-frequency orbit determination for the CYGNSS spacecraft using GipsyX. NAVIGATION: Journal of the Institute of Navigation, 70(1). doi: https://doi.org/10.33012/navi.565.

Copernicus.eu (2023a). Instrument payload. https://sentinels.copernicus.eu/web/sentinel/missions/sentinel-6/instrument-payload. Accessed April 25th, 2023.

Copernicus.eu (2023b). Satellite description. https://sentinels.copernicus.eu/web/sentinel/missions/sentinel-6/satellite-description. Accessed April 25th, 2023.

Couderc, V. (2015). Jason-3 characteristics for POD processing,. https://ids-doris.org/documents/BC/satellites/Jason-3_CharacteristicsForPODprocessing.pdf.

Desai, S., Conrad, A., and Haines, B. (2022). GPS-based precise orbit determination of the Sentinel-6 MF mission. In Ocean Surface Topography Science Team meeting. https://ostst.aviso.altimetry.fr/fileadmin/user_upload/OSTST2022/Presentations/POD2022-GPS-based_Precise_Orbit_Determination_of_the_Sentinel-6_MF_and_Jason-3_Missions.pdf.

Desai, S. and Yuan, D.-N. (2006). Application of the convolution formalism to the ocean tide potential: Results from the Gravity Recovery and Climate Experiment (GRACE). Journal of Geophysical Research: Oceans, 111(C6). doi: https://doi.org/10.1029/2005JC003361.

Desai, S. D. and Ray, R. D. (2014). Consideration of tidal variations in the geocenter on satellite altimeter observations of ocean tides. Geophysical Research Letters, 41(7):2454–2459. doi: https://doi.org/10.1002/2014GL059614.

Dietrich, A., Ries, P., Sibois, A. E., Sibthorpe, A., Hemberger, D., Heflin, M. B., and David, M. W. (2018). Reprocessing of GPS products in the IGS14 frame. In AGU Fall Meeting Abstracts, volume 2018, pages G33C–0690.

Donlon, C., Berruti, B., Buongiorno, A., Ferreira, M.-H., Féménias, P., Frerick, J., Goryl, P., Klein, U., Laur, H., Mavrocordatos, C., et al. (2012). The global monitoring for environment and security (gmes) sentinel-3 mission. Remote sensing of Environment, 120:37–57. doi: https://doi.org/10.1016/j.rse.2011.07.024.

Donlon, C., Cullen, R., Giulicchi, L., Fornari, M., and Vuilleumier, P. (2021a). Copernicus Sentinel-6 Michael Freilich satellite mission: Overview and preliminary in orbit results. In 2021 IEEE International Geoscience and Remote Sensing Symposium IGARSS, pages 7732–7735. IEEE. doi: https://doi.org/10.1109/IGARSS47720.2021.9553731.

Donlon, C. J., Cullen, R., Giulicchi, L., Vuilleumier, P., Francis, C. R., Kuschnerus, M., Simpson, W., Bouridah, A., Caleno, M., Bertoni, R., Rancaño, J., Pourier, E., Hyslop, A., Mulcahy, J., Knockaert, R., Hunter, C., Webb, A., Fornari, M., Vaze, P., Brown, S., Willis, J., Desai, S., Desjonqueres, J.-D., Scharroo, R., Martin-Puig, C., Leuliette, E., Egido, A., Smith, W. H., Bonnefond, P., Le Gac, S., Picot, N., and Tavernier, G. (2021b). The Copernicus Sentinel-6 mission: Enhanced continuity of satellite sea level measurements from space. Remote Sensing of Environment, 258:112395. doi: https://doi.org/10.1016/j.rse.2021.112395.

Duan, B. and Hugentobler, U. (2021). Enhanced solar radiation pressure model for GPS satellites considering various physical effects. GPS Solutions, 25(2):1–14. doi: https://doi.org/10.1007/s10291-020-01073-z.

Dunn, C., Bertiger, W., Franklin, G., Harris, I., Kruizinga, G., Meehan, T., Nandi, S., Nguyen, D., Rogstad, T., Thomas, J. B., and Tien, J. (2002). The instrument on NASA's GRACE mission: augmentation of GPS to achieve unprecedented gravity field measurements. In Proceedings of

the 15th International Technical Meeting of the Satellite Division of The Institute of Navigation (ION GPS 2002), pages 724–730.

ESA (2023). Sentinel-6 Michael Freilich POD Context. https://ids-doris.org/documents/BC/satellites/Sentinel6A_PODcontext.pdf.

Esenbuğa, Ö. G. and Hauschild, A. (2020). Impact of flex power on GPS Block IIF differential code biases. GPS Solutions, 24(4):91. doi: https://doi.org/10.1007/s10291-020-00996-x.

Fischer, A. (2022). GPS III Earth Coverage (EC) Antenna Patterns. https://www.navcen.uscg.gov/sites/default/files/pdf/gps/GPS_ZIP/GPS_III_EC_Antenna_Patterns_SVN_74_75_76_77_78.pdf.

Folkner, W. M., Williams, J. G., and Boggs, D. H. (2009). The planetary and lunar ephemeris DE 421. IPN Progress Report, 42(178):1–34.

Gurtner, W. and Estey, L. (2007). RINEX-the receiver independent exchange format-version 3.00. Astronomical Institute, University of Bern and UNAVCO, Bolulder, Colorado.

Hackel, S., Montenbruck, O., Steigenberger, P., Balss, U., Gisinger, C., and Eineder, M. (2017). Model improvements and validation of terraSAR-X precise orbit determination. Journal of Geodesy, 91(5):547–562. doi: https://doi.org/10.1007/s00190-016-0982-x.

Haines, B., Bar-Sever, Y., Bertiger, W., Desai, S., and Willis, P. (2004). One-centimeter orbit determination for Jason-1: new GPS-based strategies. Marine Geodesy, 27(1-2):299–318. doi: https://doi.org/10.1080/01490410490465300.

Haines, B., Lichten, S., Lough, M., Muellerschoen, R., and Vigue-Rodi, Y. (1999). Determining precise orbits for Topex/Poseidon within one day of real time: Results and implications. In Spaceflight Mechanics 1999, volume 102, page 605–613. Advances in the Astronautical Sciences.

Haines, B. J., Bar-Sever, Y. E., Bertiger, W. I., Desai, S. D., Harvey, N., Sibois, A. E., and Weiss, J. P. (2015). Realizing a terrestrial reference frame using the Global Positioning System. Journal of Geophysical Research: Solid Earth, 120(8):5911–5939. doi: https://doi.org/10.1002/2015JB012225.

Hernández-Pajares, M., Juan, J., Sanz, J., Orus, R., Garcia-Rigo, A., Feltens, J., Komjathy, A., Schaer, S., and Krankowski, A. (2009). The IGS VTEC maps: a reliable source of ionospheric information since 1998. Journal of Geodesy, 83(3):263–275. doi: https://doi.org/10.1007/s00190-008-0266-1.

Huang, W., Männel, B., Brack, A., Ge, M., and Schuh, H. (2022). Estimation of GPS transmitter antenna phase center offsets by integrating space-based GPS observations. Advances in Space Research, 69(7):2682–2696. doi: https://doi.org/10.1016/j.asr.2022.01.004.

Jäggi, A., Dach, R., Bock, H., Beutler, G., Montenbruck, O., and Schmid, R. (2010). Extending the GPS satellite antenna patterns of the IGS to nadir angles beyond 14 using LEO data. In AGU Fall Meeting, pages 13–17.

Jäggi, A., Dach, R., Montenbruck, O., Hugentobler, U., Bock, H., and Beutler, G. (2009). Phase center modeling for LEO GPS receiver antennas and its impact on precise orbit determination. Journal of Geodesy, 83(12):1145–1162. doi: https://doi.org/10.1007/s00190-009-0333-2.

Jin, B., Chen, S., Li, M., Yue, F., and Zhao, L. (2023). Sentinel-6A attitude modeling with dual GNSS antennas and its impact on precise orbit determination. GPS Solutions, 27(1):7. doi: https://doi.org/10.1007/s10291-022-01346-9.

Johnston, G., Riddell, A., and Hausler, G. (2017). The international GNSS service. In Springer handbook of global navigation satellite systems, pages 967–982. Springer, Cham. doi: https://doi.org/10.1007/978-3-319-42928-1_33.

Kang, Z., Bettadpur, S., Nagel, P., Save, H., Poole, S., and Pie, N. (2020). GRACE-FO precise orbit determination and gravity recovery. Journal of Geodesy, 94:1–17. doi: https://doi.org/10.1007/s00190-020-01414-3.

Knocke, P., Ries, J., and Tapley, B. (1988). Earth radiation pressure effects on satellites. In AIAA/AAS Astrodynamics Conference, page 4292. doi: https://doi.org/10.2514/6.1988-4292.

Kobel, C., Arnold, D., and Jäggi, A. (2021). Impact of different attitude modes on Jason-3 precise orbit determination and antenna phase center modeling. In EGU General Assembly Conference Abstracts, pages EGU21–4831.

Le Traon, P. Y., Reppucci, A., Alvarez Fanjul, E., Aouf, L., Behrens, A., Belmonte, M., Bentamy, A., Bertino, L., Brando, V. E., Kreiner, M. B., et al. (2019). From observation to information and users: The copernicus marine service perspective. Frontiers in Marine Science, 6:234. doi: https://doi.org/10.3389/fmars.2019.00234.

Lemoine, J.-M., Biancale, R., Reinquin, F., Bourgogne, S., and Gégout, P. (2019). CNES/GRGS RL04 Earth gravity field models, from GRACE and SLR data. GFZ Data Services.

Li, W., Cardellach, E., Fabra, F., Ribo, S., and Rius, A. (2018). Lake level and surface topography measured with spaceborne GNSS-reflectometry from CYGNSS mission: Example for the lake Qinghai. Geophysical Research Letters, 45(24):13–332. doi: https://doi.org/10.1029/2018GL080976.

Li, W., Cardellach, E., Fabra, F., Ribó, S., and Rius, A. (2019). Assessment of spaceborne GNSS-R ocean altimetry performance using CYGNSS mission raw data. IEEE Transactions on Geoscience and Remote Sensing, 58(1):238–250. doi: https://doi.org/10.1109/TGRS.2019.2936108.

Lockheed Martin (2019). SVN74 APC & ISC data release, January 2019.

Lyard, F., Lefevre, F., Letellier, T., and Francis, O. (2006). Modelling the global ocean tides: modern insights from FES2004. Ocean Dynamics, 56(5):394–415. doi: https://doi.org/10.1007/s10236-006-0086-x.

Mao, X., Arnold, D., Girardin, V., Villiger, A., and Jäggi, A. (2021). Dynamic GPS-based LEO orbit determination with 1 cm precision using the Bernese GNSS Software. Advances in Space Research, 67(2):788–805. doi: https://doi.org/10.1016/j.asr.2020.10.012.

Marshall, J. A. and Luthcke, S. B. (1994). Modeling radiation forces acting on TOPEX/Poseidon for precision orbit determination. Journal of Spacecraft and Rockets, 31(1):99–105.

Mashburn, J., Axelrad, P., Zuffada, C., Loria, E., O'Brien, A., and Haines, B. (2020). Improved GNSS-R ocean surface altimetry with CYGNSS in the seas of Indonesia. IEEE Transactions on Geoscience and Remote Sensing, 58(9):6071–6087. doi: https://doi.org/10.1109/TGRS.2020.2973079.

Mercier, F. and Couhert, A. (2016). Jason-3 SLR range correction estimation. https://ilrs.gsfc.nasa.gov/docs/2020/Jason3correctionSLR.pdf.

Milani, A., Nobili, A. M., and Farinella, P. (1987). Non-gravitational perturbations and satellite geodesy. Adam Hilger Ltd., Bristol, UK.

Montenbruck, O. (2003). Kinematic GPS positioning of LEO satellites using ionosphere-free single frequency measurements. Aerospace Science and Technology, 7(5):396–405. doi: https://doi.org/10.1016/S1270-9638(03)00034-8.

Montenbruck, O., Garcia-Fernandez, M., Yoon, Y., Schön, S., and Jäggi, A. (2009). Antenna phase center calibration for precise positioning of LEO satellites. GPS Solutions, 13:23–34. doi: https://doi.org/10.1007/s10291-008-0094-z.

Montenbruck, O. and Gill, E. (2002). Ionospheric correction for GPS tracking of LEO satellites. The Journal of Navigation, 55(2):293–304. doi: https://doi.org/10.1017/S0373463302001789.

Montenbruck, O., Hackel, S., and Jäggi, A. (2018). Precise orbit determination of the Sentinel-3A altimetry satellite using ambiguity-fixed GPS carrier phase observations. Journal of Geodesy, 92(7):711–726. doi: https://doi.org/10.1007/s00190-017-1090-2.

Montenbruck, O., Hackel, S., Wermuth, M., and Zangerl, F. (2021). Sentinel-6A precise orbit determination using a combined GPS/Galileo receiver. Journal of Geodesy, 95(9):1–17. doi: https://doi.org/10.1007/s00190-021-01563-z.

Montenbruck, O. and Kroes, R. (2003). In-flight performance analysis of the CHAMP BlackJack GPS Receiver. GPS Solutions, 7(2):74–86. doi: https://doi.org/10.1007/s10291-003-0055-5.

Montenbruck, O., Schmid, R., Mercier, F., Steigenberger, P., Noll, C., Fatkulin, R., Kogure, S., and Ganeshan, A. S. (2015a). GNSS satellite geometry and attitude models. Advances in Space Research, 56(6):1015–1029. doi: https://doi.org/10.1016/j.asr.2015.06.019.

Montenbruck, O., Steigenberger, P., and Hugentobler, U. (2015b). Enhanced solar radiation pressure modeling for Galileo satellites. Journal of Geodesy, 89(3):283–297. doi: https://doi.org/10.1007/s00190-014-0774-0.

Montenbruck, O., Swatschina, P., Markgraf, M., Santandrea, S., Naudet, J., and Tilmans, E. (2012). Precision spacecraft navigation using a low-cost GPS receiver. GPS Solutions, 16(4):519–529. doi: https://doi.org/10.1007/s10291-011-0252-6.

Montenbruck, O., Van Helleputte, T., Kroes, R., and Gill, E. (2005). Reduced dynamic orbit determination using GPS code and carrier measurements. Aerospace Science and Technology, 9(3):261–271. doi: https://doi.org/10.1016/j.ast.2005.01.003.

Montenbruck, O., Wermuth, M., and Hackel, S. (2022). Cross-calibration of the TRIG and PODRIX GNSS receivers onboard Sentinel-6A. In Ocean Surface Topography Science Team Meeting 2022. https://elib.dlr.de/189926/.

Muellerschoen, R. J., Bertiger, W. I., Wu, S. C., Munson, T. N., Zumberge, J. F., and Haines, B. (1994). Accuracy of GPS determined TOPEX/Poseidon orbits during anti-spoof periods. In Proceedings of the 1994 National Technical Meeting of The Institute of Navigation, pages 607–614.

Nguyen, V. A., Nogués-Correig, O., Yuasa, T., Masters, D., and Irisov, V. (2020). Initial GNSS phase altimetry measurements from the spire satellite constellation. Geophysical Research Letters, 47(15):e2020GL088308. doi: https://doi.org/10.1029/2020GL088308.

O'Brien, A. (2019). Personal Communication.

Parke, M. E., Stewart, R. H., Farless, D. L., and Cartwright, D. E. (1987). On the choice of orbits for an altimetric satellite to study ocean circulation and tides. Journal of Geophysical Research: Oceans, 92(C11):11693–11707. doi: https://doi.org/10.1029/JC092iC11p11693.

Pearlman, M. R., Noll, C. E., Pavlis, E. C., Lemoine, F. G., Combrink, L., Degnan, J. J., Kirchner, G., and Schreiber, U. (2019). The ILRS: approaching 20 years and planning for the future. Journal of Geodesy, 93(11):2161–2180. doi: https://doi.org/10.1007/s00190-019-01241-1.

Peter, H., Springer, T., Zangerl, F., and Reichinger, H. (2022). Beyond gravity PODRIX GNSS receiver on Sentinel-6 Michael Freilich–receiver performance and POD analysis. In Proceedings of the 35th International Technical Meeting of the Satellite Division of The Institute of Navigation (ION GNSS+ 2022), pages 589–601. doi: https://doi.org/10.33012/2022.18368.

Petit, G. and Luzum, B. (2010). Iers conventions (2010). Technical report, Bureau International des Poids et mesures sevres (France).

Ray, R. D. (2013). Precise comparisons of bottom-pressure and altimetric ocean tides. Journal of Geophysical Research: Oceans, 118(9):4570–4584. doi: https://doi.org/10.1002/jgrc.20336.

Rebischung, P. and Schmid, R. (2016). IGS14/igs14.atx: A new framework for the IGS products. In AGU Fall Meeting 2016, San Francisco, CA. American Geophysical Union.

Rodriguez-Solano, C., Hugentobler, U., and Steigenberger, P. (2012). Adjustable box-wing model for solar radiation pressure impacting GPS satellites. Advances in Space Research, 49(7):1113–1128. doi: https://doi.org/10.1016/j.asr.2012.01.016.

Rothacher, M., Schaer, S., Mervart, L., and Beutler, G. (1995). Determination of antenna phase center variations using GPS data. In IGS Workshop Proceedings: Special Topics and New Directions, pages 205–220. IGS.

Rudenko, S., Neumayer, K.-H., Dettmering, D., Esselborn, S., and Schöne, T. (2015). Improvements in precise orbit determination of altimetry satellites. In Ocean Surface Topography Science Team meeting.

Ruf, C. S., Gleason, S., Jelenak, Z., Katzberg, S., Ridley, A., Rose, R., Scherrer, J., and Zavorotny, V. (2012). The CYGNSS nanosatellite constellation hurricane mission. In 2012 IEEE International Geoscience and Remote Sensing Symposium, pages 214–216. IEEE. doi: https://doi.org/10.1109/IGARSS.2012.63516008.

Schmid, R., Dach, R., Collilieux, X., Jäggi, A., Schmitz, M., and Dilssner, F. (2016). Absolute IGS antenna phase center model igs08.atx: status and potential improvements. Journal of Geodesy, 90(4):343–364. doi: https://doi.org/10.1007/s00190-015-0876-3.

Schmid, R., Rothacher, M., Thaller, D., and Steigenberger, P. (2005). Absolute phase center corrections of satellite and receiver antennas. GPS Solutions, 9(4):283–293. doi: https://doi.org/10.1007/s10291-005-0134-x.

Schmid, R., Steigenberger, P., Gendt, G., Ge, M., and Rothacher, M. (2007). Generation of a consistent absolute phase-center correction model for GPS receiver and satellite antennas. Journal of Geodesy, 81(12):781–798. doi: https://doi.org/10.1007/s00190-007-0148-y.

Shao, K., Gu, D., Chang, X., Yi, B., and Wang, Z. (2019). Impact of GPS receiver antenna GRAPHIC residual variations on single-frequency orbit determination of LEO satellites. Advances in Space Research, 64(5):1166–1176. doi: https://doi.org/10.1016/j.asr.2019.06.014.

Steigenberger, P., Thoelert, S., and Montenbruck, O. (2020). GPS III Vespucci: Results of half a year in orbit. Advances in Space Research, 66(12):2773–2785. doi: https://doi.org/10.1016/j.asr.2020.03.026.

Steigenberger, P., Thölert, S., and Montenbruck, O. (2019). Flex power on GPS block IIR-M and IIF. GPS Solutions, 23(1):8. doi: https://doi.org/10.1007/s10291-018-0797-8.

Thoelert, S., Steigenberger, P., Montenbruck, O., and Meurer, M. (2019). Signal analysis of the first GPS III satellite. GPS Solutions, 23(4):1–11. doi: https://doi.org/10.1007/s10291-019-0882-7.

Tien, J., Young, L., Meehan, T., Franklin, G., Hurst, K., Esterhuizen, S., and Team, T. G. R. (2010). Next generation of spaceborne GNSS receiver for radio occultation science and precision orbit determination. In AGU Fall Meeting Abstracts, volume 2010, pages G51A–0661.

Tien, J. Y., Okihiro, B. B., Esterhuizen, S. X., Franklin, G. W., Meehan, T. K., Munson, T. N., Robison, D. E., Turbiner, D., and Young, L. E. (2012). Next generation scalable spaceborne GNSS science receiver. In Proceedings of the 2012 International Technical Meeting of The Institute of Navigation, pages 882–914.

Unwin, M., Jales, P., Blunt, P., Duncan, S., Brummitt, M., and Ruf, C. (2013). The SGR-ReSI and its application for GNSS reflectometry on the NASA EV-2 CYGNSS mission. In 2013 IEEE Aerospace Conference, pages 1–6. IEEE. doi: https://doi.org/10.1109/AERO.2013.6497151.

Wang, T., Ruf, C. S., Gleason, S., O'Brien, A. J., McKague, D. S., Block, B. P., and Russel, A. (2021). Dynamic calibration of gps effective isotropic radiated power for gnss-reflectometry earth remote sensing. IEEE Transactions on Geoscience and Remote Sensing, 60:1–12. doi: https://doi.org/10.1109/TGRS.2021.3070238.

Wingham, D., Francis, C., Baker, S., Bouzinac, C., Brockley, D., Cullen, R., de Chateau-Thierry, P., Laxon, S., Mallow, U., Mavrocordatos, C., et al. (2006). CryoSat: A mission to determine the fluctuations in earth's land and marine ice fields. Advances in Space Research, 37(4):841–871. doi: https://doi.org/10.1016/j.asr.2005.07.027.

Wu, S. and Thornton, C. (1985). OASIS—a new GPS covariance and simulation analysis. In Positioning with GPS-1985: Proceedings, First International Symposium on Precise Positioning with the Global Positioning System, Rockville, Maryland, April 15-19, 1985, volume 1, page 337. US Department of Commerce, National Oceanic and Atmospheric Administration.

Wu, S.-C., Yunck, T. P., and Thornton, C. L. (1991). Reduced-dynamic technique for precise orbit determination of low earth satellites. Journal of Guidance, Control, and Dynamics, 14(1):24–30. doi: https://doi.org/10.2514/3.20600.

Young, L., Neilan, R., and Bletzacker, F. (1985). GPS satellite multipath: an experimental investigation. In First International Symposium on Precise Positioning with the Global Positioning System, Rockville, Maryland, volume 1, page 423.

Yunck, T., Bertiger, W., Wu, S., Bar-Sever, Y., Christensen, E., Haines, B., Lichten, S., Mueller-schoen, R., Vigue, Y., and Willis, P. (1994). First assessment of GPS-based reduced dynamic orbit determination on TOPEX/Poseidon. Geophysical Research Letters, 21(7):541–544. doi: https://doi.org/10.1029/94GL00010.

Yunck, T., Wu, S.-C., Wu, J.-T., and Thornton, C. (1990). Precise tracking of remote sensing satellites with the Global Positioning System. IEEE Transactions on Geoscience and Remote Sensing, 28(1):108–116. doi: https://doi.org/10.1109/36.45753.

Yunck, T. P. (1993). Coping with the atmosphere and ionosphere in precise satellite and ground positioning. Washington DC American Geophysical Union Geophysical Monograph Series, 73:1–16. doi: https://doi.org/10.1029/GM073p0001.

Zandbergen, R., Gini, F., Schönemann, E., Mayer, V., Otten, M., Springer, T., and Enderle, W. (2022). ESA/ESOC-precise orbit determination for Sentinel-6 Michael Freilich based on Galileo and GPS observations. In Proceedings of the 35th International Technical Meeting of the Satellite Division of The Institute of Navigation (ION GNSS+ 2022), pages 575–588. doi: https://doi.org/10.33012/2022.18413.